https://doi.org/10.5194/egusphere-2025-5823
Preprint. Discussion started: 27 January 2026

ARTEMIS version 1.0: A Reactive Transport Enhanced Rock Weathering Model with Coupled Soil Carbon and Nutrient Dynamics

Lyla Taylor[1], Rachael H. James[2], Ilsa Kantola[3], and David Beerling[1]

[1]Leverhulme Centre for Climate Change Mitigation, School of Biosciences, University of Sheffield, Sheffield, UK
[2]School of Ocean and Earth Science, National Oceanography Centre Southampton, European Way, Southampton, SO14 3ZH, UK
[3]Institute for Sustainability, Energy and Environment, Carl R. Woese Institute for Genomic Biology, University of Illinois at Urbana-Champaign, Illinois, USA

Correspondence: Lyla Taylor (L.L.Taylor@sheffield.ac.uk)

Abstract. Enhanced rock weathering (ERW) is increasingly considered to be a promising carbon dioxide reduction (CDR) strategy, but carbon removal can be is difficult to verify with field measurements. Reactive transport models (RTMs) have the potential to shed light on the soil dynamics affecting CDR, and to quantify the timescales involved. Here, we present a new 1-D RTM representing all major processes affecting the chemistry of soils. These processes include nitrogen cycling kinetics, sorption and the choice of open or closed systems with respect to gas diffusion. We demonstrate this model's utility with a detailed investigation examining the impact of those key ERW and soil processes on CDR and topsoil pH at a site in the United States Corn Belt. Given continued annual applications of a metabasalt for 55 years, results indicate a 20-year lag time to achieve 10 tCO_2 ha^{-1} for CDR based on solute export in drainage water, with long-term topsoil pH (7.5–8.0) maintained by sorption. Topsoil pH would stabilise below the maximum recommended limit of 7.4 with triennial metabasalt treatments, but the lag time would double. Five-year model runs with four annual metabasalt treatments suggest doubled bicarbonate export in the absence of nitrogen kinetics due to reduced strong acid weathering. Calcite deposition in the upper soil occurs if the metabasalt is replaced with a pure $CaSiO_3$ feedstock, reducing CDR efficiency. For a pure Mg_2SiO_4 feedstock, calcite deposition limits Mg export because Mg replaces exchangeable Ca on soil clay surfaces. Without sorption, calcite saturation maintains topsoil pH near 8 for all feedstocks under open system conditions. However, topsoil pH was unrealistically high (~ 10) for the $CaSiO_3$ feedstock with a closed system. With these model runs, we illustrate the process representation useful for predicting solute export through soils at individual field sites. Critically, we also discuss the limitations of this model and possibilities for development of the next generation of ERW models.

1 Introduction

It is now widely understood that carbon dioxide reduction (CDR) will be necessary to help avert climate change, but conventional methods such as afforestation are unlikely to remove sufficient carbon to limit warming to 1.5° (Lamb et al., 2024). Novel CDR methods such as enhanced rock weathering (ERW) could help fill this CDR gap while providing a range of co-

https://doi.org/10.5194/egusphere-2025-5823
Preprint. Discussion started: 27 January 2026

benefits for crops (Beerling et al., 2018) and mitigating greenhouse gas (GHG) emissions (Chiaravalloti et al., 2023). ERW is compatible with other land-based CDR methods, with the potential to improve plant nutrient cycling and GHG emissions as well as carbon capture (Anthony et al., 2025; Almaraz, 2025; de Oliveira Garcia et al., 2020).

Weathering, and therefore CDR via ERW, depends on soil solution chemistry along with geochemical interactions with solid soil phases. In the upper layers of soils, biological nutrient cycling along with root and microbial respiration partially control key drivers of weathering, such as pH. However, agricultural soils often have a long history of repeated human disturbance and intervention, including liming, fertiliser applications, harvests and tillage. The geochemistry of these soils is therefore likely to be perturbed relative to any putative natural, pre-agriculture state.

Biological effects on ERW and CDR are increasingly recognised (e.g., Vicca et al., 2022) and included in modelling studies to varying degrees and at different scales (e.g., Deng et al., 2023; Gaucher et al., 2025; Kantzas et al., 2022), but many of the agricultural management processes noted above are not routinely quantified or explicitly represented in geochemical models. The detailed process model presented here (ARTEMIS) was developed to help fill some of those gaps and to allow investigation of the effects of agriculturally-mediated carbon and nutrient cycling processes on CDR via ERW. Here, a technical description of the implemented weathering and nutrient-cycling processes is followed by an example of calibrating and validating ARTEMIS using field data from a long-term ERW experiment (Beerling et al., 2024). Finally, the capabilities of this model to isolate several key process effects (sorption, nitrogen kinetics and CO_2 availability) on CDR are presented. A subsidiary aim of this paper is to illustrate how these processes might be represented and improved in the next generation of ERW-CDR reactive transport models (RTMs).

2 Modelled biogeochemical processes

To understand short-term carbon cycling and carbon capture in agriculturally-managed soils, ARTEMIS aims to capture all the key processes impacting soil chemistry in agricultural settings (Table 1). This will include both the weathering arena, where feedstock dust has been added to soil, and the subsoil through which weathering products must be transported.

ARTEMIS does not currently include longer-term natural processes such as physical erosion, dust or sediment deposition, bedrock fragmentation, saprolite or aquifer development, pedogenesis, ecosystem succession or disturbances such as fire. Baseline geochemical and vegetation data describing the pre-ERW system state are prescribed.

2.1 Aqueous speciation and sorption

ARTEMIS (Figure 1) is essentially a preprocessor and wrapper for the well-known PHREEQC geochemical speciation and batch-reaction model (Parkhurst and Appelo, 2013), which will not be described in great detail here. PHREEQC computes all aqueous speciation and other equilibrium processes such as cation exchange and surface complexation. Cation exchange parameters for clay surfaces are defined in the PHREEQC "EXCHANGE" data block, while parameters for complexation with organic and ferric oxide surfaces are defined in the PHREEQC "SURFACE" data block (Parkhurst and Appelo, 2013). In general, surface complexation binds cations more strongly than cation exchange on clays, but depending on the extraction

https://doi.org/10.5194/egusphere-2025-5823
Preprint. Discussion started: 27 January 2026

Table 1. Modelled processes

Process	Section	Key references
Aqueous speciation and sorption	Sec. 2.1	Parkhurst and Appelo (2013)
Mineral weathering	Sec. 2.2.1	Palandri and Kharaka (2004, Eqn. 6)
Organic matter decomposition	Sec. 2.3.1	Neitsch et al. (2011); Lawrence et al. (23 March 2020)
Nitrogen cycling	Sec. 2.4	Neitsch et al. (2011)
Fertilisers	Sec. 2.5	
Plant nutrient uptake	Sec. 2.6.2	Neitsch et al. (2011)
Evapotranspiration	Sec. 2.7.2	Neitsch et al. (2011)
Respiration and soil pCO_2 profile	Sec. 2.9	Cerling (1991)
Hydrology	Sec. 2.7	

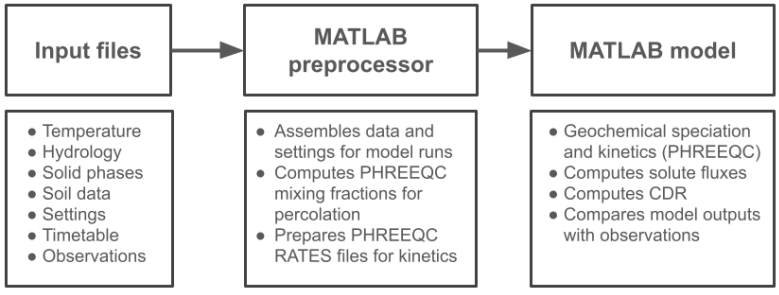

Figure 1. System diagram for ARTEMIS. Written in MATLAB, ARTEMIS comprises a preprocessor and a main model function. Geochemical and kinetic calculations are performed by PHREEQC (Parkhurst and Appelo, 2013). See the user guide for details about the input files.

method, some of the surface sites defined for organic matter may contribute to measured cation exchange capacity (CEC, e.g., Johnson, 2002). By default, ARTEMIS assigns all CEC to clays, but includes options to assign some the measured CEC to organic surface sites. It is also possible to exclude surfaces at runtime.

CEC data for the soil layers are required inputs for ARTEMIS. Users can choose to allow PHREEQC to initialise the EXCHANGE block via equilibration with the solution, in which case base saturation will be close to 100%. Alternatively, exchangeable cation data can be provided. If these data do not sum to the given CEC, exchangeable acidity will be added in the form of H^+ or other cation specified by the user, such as Al^{3+}.

https://doi.org/10.5194/egusphere-2025-5823
Preprint. Discussion started: 27 January 2026

The sites for surface complexation on organic matter are defined as described in (Example 19 of Parkhurst and Appelo, 2013). For each active gram of organic carbon, there are four monoprotic carboxylic sites with a charge of 2.84 meq g^{-1}, four monoprotic phenolic sites with a charge of 1.42 meq g^{-1}, and twelve diprotic sites with a charge of 2.84 meq g^{-1}. For these sites to be defined, the user must provide soil organic carbon data. The default specific surface area is 12 m^2 g^{-1} organic carbon, as PHREEQC tended to crash with the much larger surface areas in (Example 19 of Parkhurst and Appelo, 2013). That example specified the active fraction of organic carbon as 0.629 (Shi et al., 2007) and also specified 0.1 as the active fraction for analyzed Fe. Strong and weak sites for complexation with Fe oxides are defined by multiplying active moles of extractable Fe by 0.005 and 0.2 respectively (Dzombak and Morel, 1990; Parkhurst and Appelo, 2013). Extractable Fe can be provided or calculated from goethite, ferrihydrite, or phases with formula FeOOH if such phases have been defined by the user. Following Dzombak and Morel (1990) and Parkhurst and Appelo (2013), the default Fe specific surface area is 600 m^2 g^{-1}.

The full list of aqueous and solid geochemical species,equilibrium reactions and thermodynamic constants recognised by PHREEQC are defined in an input database. ARTEMIS is designed to use non-standard geochemical databases (THAmmOrg.dat or THAmmOrgAl.dat) which are included with the ARTEMIS software. The database THAmmOrg.dat was developed from Tipping_Hurley.dat, a version of the wateq4f.dat database which includes sorption to organic matter (Tipping and Hurley, 1992; Tipping, 1998; Lofts and Tipping, 2000). Both Tipping_Hurley.dat and wateq4f.dat ship with recent versions of PHREEQC. The key difference between Tipping_Hurley.dat and THAmmOrg.dat is that ammonium and nitrate are redox-decoupled in the latter, because nitrification and denitrification in soils are both microbially mediated and should be modelled as kinetic processes (Section 2.4). There are several additional differences between these two databases and Tipping_Hurley.dat, such as the inclusion of some additional master species (Table 2). The second database, THAmmOrgAl.dat, is like THAmmOrg.dat except it includes Al complexation with organic matter following Erlandsson et al. (2016, their Table S1).

Limitations of the treatment of sorption in ARTEMIS include the lack of sorption to inorganic surfaces other than hydrous ferric oxides, and lack of dynamic coupling of sorption to secondary phases that may be allowed to dissolve or precipitate, such as ferrihydrite or gibbsite. Silicic acid sorption to stable oxides is not currently modelled, nor are transitions between solid phases, such as the transformation of amorphous $Al(OH)_3$ to gibbsite (Yariv and Cross, 2012).

With respect to cation exchange, the default equilibrium constants for exchange represent sorption to clays such as kaolinite. Parameters for smectites (Benson, 1982) and montomorillonite (Fletcher and Sposito, 1989) are included in the same directory with the THAmmOrg.dat and THAmmOrgAl.dat databases, but as separate files which can be added as PHREEQC INCLUDE$ files using a keyword when running the model on the MATLAB command line. See the ARTEMIS user manual for details.

2.2 Solid phase dynamics

Solid phases include feedstock phases, native soil phases, and secondary phases; they can be crystalline or amorphous. All solid phases to be modelled must be defined in an input phases file along with sufficient parameters to represent them. These parameters should normally include the equilibrium constant ($\log_{10}K$).

There are four options for representing solid phases in ARTEMIS:

https://doi.org/10.5194/egusphere-2025-5823
Preprint. Discussion started: 27 January 2026

Table 2. Additional master species in the THAmmOrg.dat database for PHREEQC

Element name	Master species	Description
Amm	AmmH+	Ammonium (N(-3), redox-decoupled from nitrate)
Oxalate	Oxalate-2	Low molecular weight diprotic organic acid
Ti	Ti(OH)4	Titanium, for ilmenite weathering and anatase equilibria
Urea	Urea	Organic fertiliser (kinetic aqueous phase)
Tracer	Tracer	Unreactive tracer
Hubstrsoifd	Hubstrsoifd-3	Triprotic organic acid analogue using citrate molecular mass (Fakhraei and Driscoll, 2015)
Citrate	Citrate-3	Low molecular weight triprotic organic acid

kinetic The phase will dissolve and possibly precipitate following kinetic rate laws (Section 2.2.1) and thermodynamic parameters which must be provided for it. Precipitation will only be allowed if the phase is designated as reversible.

implicit The phase will dissolve in tandem with kinetic phases, ignoring any rate laws or thermodynamic parameters that may have been provided for it.

equilibrium The phase will dissolve and precipitate thermodynamically, ignoring any kinetic rate laws that may have been provided for it. At minimum, the equilibrium constant must be provided.

ignore The phase will not participate in any dissolution or precipitation reactions (no thermodynamic or kinetic data are required for such phases). The phase will, however, be included in preliminary surface area calculations.

These options (including the reversibility of kinetic phases) can be changed at runtime without updating the input phase file(s).

Interactions between inorganic and organic solid phases are not yet explicitly represented in ARTEMIS. These include stabilisation of particulate and mineral-associated organic matter (POM and MAOM) by aggregation, phyllosilicates and short-range-order amorphous phases (e.g., Barré et al., 2014; Lavallee et al., 2020; Stoner et al., 2023). Given the importance of MAOM carbon in global carbon cycling and its prevalence in key ERW arenas such as croplands and grasslands (Sokol et al., 2022), these interactions should be prioritised in the next generation of ERW models.

2.2.1 Mineral weathering

Weathering is modelled as a kinetic process, with rate laws of the form (Palandri and Kharaka, 2004) given in Eqn 1 (see Table 3 for detailed descriptions of the variables):

$$R_m = -A_m \times \sum_i \left(k_{i,m}^{289.15K} e^{\frac{-E_{app,i,m}}{R}\left(\frac{1}{T}-\frac{1}{298.15K}\right)} \prod_j [a_{i,j,m}^{n_{i,j,m}} (1-\Omega_m^{p_{i,m}})^{q_{i,m}}] \right) \quad (1)$$

https://doi.org/10.5194/egusphere-2025-5823
Preprint. Discussion started: 27 January 2026

In ARTEMIS, it is possible to define phases that dissolve or precipitate kinetically, specifying parameters for this type of rate law. Dissolution kinetics may also be considered to be fully reversible assuming microscopic reversibility (Tolman, 1925; Lasaga, 1984; Palandri and Kharaka, 2004). In this case, the equilibrium constant K_m (Table 3) represents the ratio between the forward (+) and backward (−) kinetic rate constants such that $k_{-,i,m} = k_{+,i,m}/K_m$. Alternatively, any phase with a specified equilibrium constant K_m can also be modelled as an equilibrium phase which dissolves or precipitates instantly depending its saturation state Ω_m.

Reversibility of dissolution kinetics, precipitation kinetics and choice of rate laws all require caution. Rate laws such as those of Palandri and Kharaka (2004) for silicate phases were determined by regression of apparent net rates of elemental release measured from solution chemistry in far-from-equilibrium experiments (Zhu et al., 2020). These rate laws can overestimate weathering rates of key basalt components near equilibrium by several orders of magnitude (Zhu et al., 2020, 2021; Chen et al., 2024). They are also effectively irreversible for primary silicate minerals, whose precipitation is unlikely at the pressures and temperatures in soils due to the saturation of secondary phases. Recent work by Zhu et al. (2020) suggests that near-equilibrium dissolution of feldspars at $< 100°C$ is coupled with precipitation of secondary phases and so should be modeled as a forward reaction without significant back-reaction. Their rates are 1.5 orders of magnitude slower than those of Palandri and Kharaka (2004). Zhu et al. (2021) looked at near-equilibrium albite weathering using stable Si isotopic tracers, avoiding the problem of secondary precipitation altering the apparent rates as determined with solution Al or Si. They found that precipitation does occur, but that rate laws from compilations such as that of Palandri and Kharaka (2004) which are based on solution chemistry represent net rates.

Natural waters in basaltic systems such as Iceland offer additional insight regarding primary mineral precipitation and dissolution when applying basaltic material to soils. Stefánsson and Arnórsson (2000) noted that albite and K-feldspar are common in hydrothermal systems and are likely to have been precipitated as secondary minerals (particularly for temperatures $> 200°C$). They suggest that primary disordered feldspars may dissolve while ordered end-member ones (albite and K-feldspar) precipitate. However, Stefánsson et al. (2001) observed more or less saturated (high) albite at basic pH in spring water whereas more calcic plagioclases, olivines and pyroxenes other than the pure Fe end-members are undersaturated. They considered that primary minerals remained more or less undersaturated due to the saturation of secondary phases such as amorphous $FeOH_3$, imogolite, allophane, and smectites, and due to uptake of K and possibly Mg by organisms. Their observations accord well with the Goldich mineral stability series (Goldich, 1938).

At present, ARTEMIS does not check whether kinetic rate laws or reversibility are sensible for any particular phases. It is up to the user to make reasonable decisions, but the inclusion of secondary phases is highly recommended as their dynamics will affect the saturation indices of the primary minerals. Judicious secondary phase choices should also allow modelling of cation trapping in the interlayers of clays.

2.2.2 Particle size distributions for feedstocks

Feedstock particle size distribution (PSD) data can be provided as inputs for ARTEMIS. In the absence of such data, a PSD can be derived from a cumulative distribution function (CDF, Equation 2) suitable for milled feedstocks (Rosin and Rammler,

https://doi.org/10.5194/egusphere-2025-5823
Preprint. Discussion started: 27 January 2026

Table 3. Variables in the weathering rate equation (Eqn 1)

Variable	Units	Description
m		Index of the phase (mineral or amorphous solid) being weathered
i		Index of the mechanism, e.g., acid, neutral, base, etc.
j		Index of the species participating in the weathering reaction, e.g., H^+, H_2O, OH^-, etc. NB: More than one species j can be associated with a mechanism i (e.g., acid) (e.g., see Eqn 3b for pyrite, Palandri and Kharaka, 2004)
R_m	$\text{mol}_{\text{phase}}\ \text{m}_{\text{phase}}^{-2}\ \text{s}^{-1}$	Rate at which phase m weathers
A_m	m^2	Reactive surface area of phase m
$k_{i,m}$	$\text{mol}_{\text{phase}}\ \text{m}_{\text{phase}}^{-2}\ \text{s}^{-1}$	Rate constant for weathering a phase via mechanism i
$E_{app,i,m}$	kJ mol^{-1}	Apparent activation energy for weathering a phase via mechanism i
R	$\text{J mol}^{-1}\ \text{K}^{-1}$	Gas constant
T	K	Temperature
$a_{i,j,m}$		Activity of species j weathering the phase via mechanism i
$n_{i,j,m}$		Reaction order of species j weathering the phase via mechanism i
Ω_m		Saturation index of the phase being weathered, where $\Omega = Q/K$
Q_m		Activity product of phase m
K_m		Solubility (equilibrium) constant of phase m
$p_{m,i}$		Empirical exponent for Ω (default: 1)
$q_{m,i}$		Empirical exponent for the affinity term $(1-\Omega^{p_i})$ (default: 1)

https://doi.org/10.5194/egusphere-2025-5823
Preprint. Discussion started: 27 January 2026

1933; Brown and Wohletz, 1995):

$$\mathrm{CDF} = 1 - \exp\left(\ln(0.2) \cdot \left(\frac{d}{p80}\right)^{s}\right) \tag{2}$$

where d is a vector of particle diameters (mm) for the upper bin edges, s is a spread parameter and $p80$ is the diameter (mm) below which 80% of particles are found. If diameters are not provided, they will be created following Equation 3:

$$d = \exp\left(-4.5 : 0.135 : \max\left(8, \ln\left(p80 \cdot 1000 \cdot 3\right)\right)\right) \cdot \frac{1}{1000} \tag{3}$$

where $-4.5 : 0.135 : x$ generates a vector of logged upper-bin particle diameters in the range $0.01 - x\,\mu$m with spacing $0.02\,\mu$m. x will have a minimum value of 3 mm.

2.2.3 Reactive surface area for feedstock phases

In ARTEMIS, weathering kinetics are calculated within PHREEQC (Sec. 2.2.1), but PHREEQC does not represent particles explicitly. Instead, it calculates the change in moles over time t from M_0 to M_t for each feedstock phase. Changes in RSA from A_0 to A_t for each phase must therefore be calculated from the change in moles, given simple relationships with changes in physical particle dimensions. Consider N smooth spherical particles with radius R and total moles M. These particles have a total surface area $A = N \cdot 4\pi R^2$, and total volume $V = N \cdot \frac{4}{3}\pi R^3$. The volume and mole ratios are both related to the cubed radius ratios: $\frac{V_t}{V_0} = \frac{M_t}{M_0} = \frac{R_t^3}{R_0^3}$, and the area ratio to the squared radius ratio: $\frac{A_t}{A_0} = \frac{R_t^2}{R_0^2}$. Because A_0, M_0 and M_t are all known during and after weathering, the expression given by Equation 4:

$$A_t = A_0 \left(\frac{M_t}{M_0}\right)^{\frac{2}{3}} \tag{4}$$

is easily derived from the area and mole ratios if N is constant and all N particles have the same radius. This is essentially the "shrinking sphere" approach to surface area changes during dissolution (e.g., Hangx and Spiers, 2009; Navarre-Sitchler et al., 2011).

We first calculate the initial surface area $A_{0,i}$ for each phase i by multiplying the initial surface area of the whole feedstock (see below) by either the mass fraction $f_{\mathrm{mass},i}$, the volume fraction $f_{V,i} = \frac{f_{\mathrm{mass},i}}{G_i}$, or the area fraction $f_{A,i} = 4\pi\left(f_{V,i} \cdot \frac{3}{4\pi}\right)^{\frac{2}{3}}$ for phase i, as specified by the user. Here, G_i is the specific gravity for phase i (g cm^{-3}). The default is to use the area fraction.

The initial geometric surface area for a feedstock A_{GEO} can be provided by the user. If not given, it can also be calculated using the mean particle radius of the PSD (Section 2.2.2), assuming spherical particles (Equation 5):

$$A_{\mathrm{geo}} = \frac{3}{10000} \cdot \left[\sum_{j}^{\mathrm{PSDbins}} (r_j \cdot m_j) \cdot \sum_{i}^{\mathrm{phases}} (G_i \cdot m_i)\right]^{-1} \tag{5}$$

where r_j is the radius for PSD bin j (cm), m_j is the mass fraction of feedstock in PSD bin j, m_i is the mass fraction of phase i in the feedstock, G_i is the specific gravity of phase i (cm^3 g^{-1}), and there are 10000 cm^2 m^{-2}. A surface area A_{BET} based on gas adsorption (Brunauer et al., 1938) can also be provided by the user, or it can be estimated from A_{GEO} if the user provides a roughness factor $\lambda = \frac{A_{\mathrm{BET}}}{A_{\mathrm{GEO}}}$. The user can choose either surface area.

https://doi.org/10.5194/egusphere-2025-5823
Preprint. Discussion started: 27 January 2026

There are several options for RSA dynamics during the model run, all of which use the shrinking sphere approach to update the RSA for individual feedstock phases assuming smooth, spherical monomineralogic particles:

inbuilt RSA is updated using the shrinking sphere method and the dynamic change in moles for each phase within PHREEQC (i.e., coded in the PHREEQC RATES block with the weathering calculations).

traditional RSA is updated using the shrinking sphere method by ARTEMIS at the end of each day (i.e., calculations done in MATLAB outside PHREEQC) using the change in moles for the phase. This means that RSA is constant during each day's call to PHREEQC.

static RSA does not change during the run; it remains constant until the phase disappears whereupon it is zero.

discrete PSD-tracking software (e.g., Kantzas et al., 2022, , not included with ARTEMIS) updates the RSA for each phase outside PHREEQC (in MATLAB) at the end of each day.

Scaling of initial RSA (i.e., multiplying by a constant) is possible and can be done separately for native soil phases (Section 2.2.4) and kinetic feedstock phases. It is also possible to scale the overall reaction rate of implicit feedstock phases with respect to kinetic feedstock phases. These scalings can help correct for errors in the initial RSA, but may not fully account for processes that affect the evolution of the RSA with time.

Surface coatings and associated nucleation dynamics can retard mineral dissolution rates (e.g., Nugent et al., 1998; Cubillas et al., 2005). These coatings may result from secondary phase precipitation (e.g., Nagy et al., 1999) and may have different effects on dissolution depending on the surface they have coated (Daval et al., 2010). ARTEMIS does not currently link secondary phase precipitation with the surface areas of other phases. It also does not consider apparent passivation by microbes (Oelkers et al., 2015) arising from microbial nutrient uptake and storage. These microbial processes could be represented by microbial growth, mortality and nutrient uptake in competition with plants (e.g., Lawrence et al., 23 March 2020).

Another limitation is the assumption of monomineralogical particles in ARTEMIS, unlikely to be realistic for cryptocrystalline feedstocks such as basalts. The surface area of each individual phase is required for calculating kinetic dissolution within the RATES block of PHREEQC, but at present ARTEMIS neglects the RSA dynamics of the overall feedstock. This limitation also affects the use of the discrete option, as separate PSDs are assigned to each feedstock phase. The ability to assign a single PSD to a feedstock and the use of polymineralogical particles will be developed in future by assuming that the constituent phases are evenly distributed by weight percent in each grain, ignoring mineralogical and crystallographic irregularities including veins, zoned phenocrysts, weathering rinds, exsolution lamellae (unmixing of end-member phases from a cooling solid solution), and edge dislocations. However, dislocations, phase boundaries and chemical impurities are sites of preferential dissolution (e.g., Holdren Jr and Speyer, 1987) leading to etch pitting and fragmentation.

The distributions of mass, number of fragments, and surface geometry resulting from differential dissolution and fragmentation have long been described by power laws suggesting fractal processes (e.g. Hartmann, 1969; Turcotte, 1986; Bittelli et al., 1999) in a wide variety of settings. Examples include the fragmentation of soil induced by tillage (Giménez et al., 1998), soil PSDs (Bayat et al., 2017), Parana River saprolite PSDs and pore-size distributions (Miranda et al., 2006), pore sizes and surface

https://doi.org/10.5194/egusphere-2025-5823
Preprint. Discussion started: 27 January 2026

areas in weathering basaltic andesite and quartz diorite (Navarre-Sitchler et al., 2013), and the surface roughness of weathering basalt at various spatial and temporal scales (Navarre-Sitchler and Brantley, 2007). Multi-fractal models for rocks and soils include separate fractal dimensions describing fragmentation, mass and surface changes (Perfect, 1997; Giménez et al., 1998), surface roughness, chemical reactivity, particle masses and pores (Bao et al., 2014) and soil particle size distributions (Rodríguez-Lado and Lado, 2017). These fractal models can be related to the Weibull and Rosin-Rammler distributions which describe particle sizes arising from comminution (Brown and Wohletz, 1995; Rosin and Rammler, 1933), but they are also relevant to dissolution of ERW feedstocks in soils because weathering and mechanical breakup produce similar mass distributions (Domokos et al., 2015). The fractal approach to surface roughness of Navarre-Sitchler and Brantley (2007) is represented in the PSD-tracking code developed by Mark Lomas (Beerling et al., 2020; Kantzas et al., 2022) and is also an option in the SCEPTER model (Kanzaki et al., 2022).

ARTEMIS includes beta-test options to apply surface area and surface roughness fractal dimensions to the RSA for each phase at the end of each model day. The surface fractal dimension $f_{D,s}$ (e.g., Farin and Avnir, 1987) relates the effective reactive surface area A to particle radius R: $A \propto R^{f_{D,s}-3}$, where $m = f_{D,s} - 3$ is the slope of the line given by $\log_{10} A_g = m \log_{10} R + \log_{10} A_{g,0}$. Here, A_g is a specific surface area (per unit mass). Navarre-Sitchler and Brantley (2007) related this surface fractal dimension to fragmentation of the reaction front, and suggested the range $2 < f_{Ds} < 3$ based on a review of the literature. Because f_{Ds} links the change in surface area to the change in radius ($\frac{R_t}{R_0} = \left(\frac{M_t}{M_0}\right)^{\frac{1}{3}}$, it can replace the exponent in Equation 4 when updating the reactive surface area in ARTEMIS:

$$A_t = A_0 \cdot \left(\frac{M_{i,t}}{M_{i,0}}\right)^{\frac{(f_{Ds}-3)}{3}} \tag{6}$$

$M_{i,t}$ represents the moles of phase i at the end of the model day, $M_{i,0}$ gives the moles of phase i at the start of the day, and f_{Ds} is the surface fractal dimension defined for the feedstock. Likewise, the roughness fractal dimension f_{Dr}, associated with the development of surface undulations on a weathering front (Navarre-Sitchler and Brantley, 2007), can be related to the ratio between characteristic length scales β and α for e.g. field and laboratory measurements and to mean grain sizes at those scales $\bar{r}^{\alpha}$ and $\bar{r}^{\beta}$ as $\lambda = \left(\frac{\beta}{\alpha}\right)^{f_{Dr}-2} = \left(\frac{\bar{r}^{\alpha}}{\bar{r}^{\beta}}\right)^{f_{Ds}-3}$. Navarre-Sitchler and Brantley (2007) suggested that $f_{Ds} \sim 2.7$ and $f_{Dr} \sim 2.3$, where the value 0.33 corresponds to $f_{Dr} - 2$.

In ARTEMIS, beta-test fractal dimensions can be specified for individual phases (e.g., Brantley and Mellott, 2000) or as single parameters applying to all feedstock phases (e.g., Navarre-Sitchler et al., 2013). They should be used with caution, as feedstock phases are represented by monomineralogical particles in ARTEMIS. It is also worth noting that these optional fractal dimensions are treated as constants within ARTEMIS, but this assumption may be incorrect: Navarre-Sitchler et al. (2013) observed a reduction in f_{Ds} from ~ 2.7 to 2.5 radially outward in the weathering rind of a basaltic andesitic clast. Finally, some studies suggest that milling imposes particle size limits outside which particle mass, diameter, surface area and number distributions are non-fractal (e.g., Stamboliadis et al., 2011).

https://doi.org/10.5194/egusphere-2025-5823
Preprint. Discussion started: 27 January 2026

2.2.4 Reactive surface area of native soil phases

Geometric reactive surface areas (RSAs) for native soil phases (minerals and amorphous inorganic solids) are based on soil texture data provided by the user: sand, silt and clay mass percentages and possibly also gravel and cobble mass percentages. We use the upper USDA diameter thresholds for clay (0.002 mm), silt (0.05 mm) and sand (2 mm); the upper limits for gravel and cobbles are 64 mm and 1000 mm respectively.

For N spherical particles of radius R, area $A = N \cdot 4\pi R^2$, volume $V = N \cdot \frac{4}{3}\pi R^3$, and mass $M = V \cdot G$, where G is the mass per unit volume or specific gravity of the phase. It follows that $A = \frac{3M}{GR}$,or in terms of diameter $D = 2R$, $A = \frac{6M}{GD}$. G is therefore a required parameter for all phases to be represented in ARTEMIS.

First, we calculate the mineral fraction of the soil as $f_C = 1 - C/0.58/100$, where C is organic carbon percentage and 0.58 is the carbon to dry matter mass ratio (Neitsch et al., 2011). Then, we compute reactive surface areas for the native phases using the upper diameter thresholds following Equation 7:

$$A = \sum_{i}^{\text{phases}} \left(\sum_{j}^{\text{diameters}} \left(M_s \cdot \frac{P_j}{100} \cdot f_C \cdot \frac{D_j}{1000 \cdot G_i} \cdot 6 \cdot p_i \right) \right) \cdot S \tag{7}$$

where $A_i j$ is the reactive surface area of phase i in size class j, M_s is the mass of soil in the layer (grams), P_j is the mass percentage of mineral soil in size class j, D_j is the upper diameter limit for size class j, G_i is the specific gravity of phase i (g cm^{-3}), and p_i is the mass proportion of phase i in the mineral soil, and S is an overall scaling factor set by the user (default: $S = 1$). Because upper size thresholds are used, this procedure underestimates the mean geometric surface area. Another limitation is that the overall soil mineral PSD is applied equally to all soil inorganic solid phases, ignoring the possibility of different phase assemblages in different size classes. Fractal approaches for native minerals are not currently available.

2.3 Nutrient cycling

Nutrient cycling plays a major role in soil chemistry and is a key driver of topsoil and subsoil acidification in agricultural systems. Bolan et al. (1991) describe the major pathways to acidifcation, all of which are considered in ARTEMIS:

1. Excess uptake of cations relative to uptake of anions by plants
2. Removal of biomass e.g. during harvest
3. Net nitrification due to fertiliser application
4. Nitrate leaching following nitrification
5. Nitrogen fixation

Excess cation uptake leads to rhizosphere acidification because cation and anion uptake by plants and their fungal symbionts is usually balanced by release of H^+ or OH^- respectively. Release of H^+ or OH^- helps plants maintain intracellular pH due to internal metabolic reactions, such as those associated with nitrate and ammonium assimilation (Neumann and Römheld,

https://doi.org/10.5194/egusphere-2025-5823
Preprint. Discussion started: 27 January 2026

2012). There are some exceptions. For example, *Lupinus angustifolius* releases organic anions when taking up nitrate (Tang et al., 1999), but at present ARTEMIS charge-balances nutrient uptake with H^+ or OH^-. Nitrogen is a plant macronutrient, so NH_4^+ (ammonium) and NO_3^- (nitrate) uptake play an important role in soil acidification.

Decomposition helps reverse acidification because it releases nutrients back to the soil, but removal of plant biomass (e.g., during harvest, De Vries and Breeuwsma, 1987) along with application of nitrogen fertilisers usually promotes acidification (De Vries and Breeuwsma, 1987). Exceptions have however been reported, such as acidification following straw application (Liang et al., 2023).

Cation exchange is another important process regulating soil chemistry, as cations may replace acidity (e.g., H^+, Al^{3+}) on soil exchangers, or vice versa. Cation exchange regulates the effect of nutrient uptake on rhizosphere pH and mobilization of nutrients (Neumann and Römheld, 2012; De Vries and Breeuwsma, 1987). Ammonium is exchangeable and can be retained in soils, but nitrate is easily leached and reduces the carbonate alkalinity of the drainage waters.

Finally, nitrogen fixation by plant-root-associated microbes (e.g., *Rhizobia*) can produce or consume acidity, especially when nitrate supply is limited. These effects are species-specific; often correlating well with cation/anion imbalance in the plant tissues (e.g., Van Beusichem, 1982; Haynes, 1983; McLay et al., 1997; Monaghan et al., 1998; Tang et al., 1998). However, rhizosphere acidification also arises from dissociation of amides during N_2 fixation and the exchange of the resulting protons for cations during nutrient uptake (Bolan et al., 1991). Tropical legumes may exhibit less rhizosphere acidification because they produce ureides instead of amides; ureides are less likely to dissociate due to higher pKa (Bolan et al., 1991).

Nutrient cycling in agroecosystems, and nitrogen cycling in particular, therefore affects the alkalinity of the soil solution and the weathering environment. ARTEMIS represents many parts of the overall soil nitrogen cycle and its contributions to soil acidity (Figure 2), including leaching, nitrification, denitrification, nitrogen uptake and fixation by plants, and mineralisation from organic matter. As previously stated, ammonium and nitrate are redox-decoupled in ARTEMIS because nitrogen cycling processes in soils are microbially mediated. ARTEMIS does not yet explicitly represent microbial population dynamics; instead, nitrification, denitrification, fixation, and decomposition kinetics follow the implict treatment of microbial function of the Soil Water and Assessment Tool (SWAT) model (2009 code, Neitsch et al., 2011).

2.3.1 Organic matter decomposition

Soil organic matter (SOM) is a larger carbon repository than land plants or the atmosphere (Schmidt et al., 2011), and because its dynamics are important for understanding and mitigating climate change, it is represented in the major earth system models (Shi et al., 2024), terrestrial biosphere models (Tian et al., 2015) and soil organic carbon (SOC) models (Sulman et al., 2018). SOC dynamics are microbially mediated, but SOC and soil microbial interactions with minerals are not always represented in the aforementioned models (Sulman et al., 2018). These interactions will likely be a focus of future research by the enhanced weathering community.

As it decomposes, SOM transforms to increasingly recalcitrant forms which decompose more slowly (Schmidt et al., 2011). Models tend to represent at least three organic matter pools (Tian et al., 2015, Table 2) which decompose at different rates and transfer nitrogen and possibly phosphorus between pools and the soil solution. ARTEMIS adopts the three-pool scheme of the

https://doi.org/10.5194/egusphere-2025-5823
Preprint. Discussion started: 27 January 2026

SWAT model (Neitsch et al., 2011), where plant residues comprise the single litter pool and there are active and passive SOM pools. Kinetics largely follow the 2009 version of the SWAT code (nminrl.f); specified fractions of nitrogen and phosphorus pass to solution (and plant availability) or to the active pool at each stage of decomposition.

Organic matter is however also a key source of other nutrients in soils, including those which affect soil chemistry or the saturation state of weathering minerals. These nutrients are released as the less recalcitrant litter pools decompose. Attiwill (1968) noted that the rates of element loss during decomposition followed a particular sequence: Na > K > Ca > Mg > P, where Na and K were largely released within three months, while Ca, Mg and P were lost as dry matter decreased. This is related to the function of the nutrients in plants: potassium and magnesium are largely non-structural, whereas calcium is bound to pectins in the middle lamella of leaves and is thus partly structural (Hawkesford et al., 2012). Na can substitute for K in natrophilic plants, including some forage grasses, but many crops are natrophobic and do not transport Na from root to shoot (Broadley et al., 2012).

2.3.2 Humus decomposition

Release of nitrogen from the stable (passive) SOM pool (N_{hums}) to the active SOM pool (N_{huma}) in ARTEMIS depends on a tunable rate constant β_{hums}, a tunable constant giving the active fraction of humic N (f_{active}) and the current state of the active pool (N_{huma}) following Equation 8 as given in the 2009 version of the SWAT module nminrl.f:

$$N_{hums,new} = \beta_{hums} \cdot \left(N_{huma} \cdot \left(\frac{1}{f_{active} - 1} \right) - N_{hums} \right) \tag{8}$$

within the limits given by Equation 9:

$$N_{hums} = \begin{cases} N_{huma} & \text{if } N_{hums} > 0 \text{ and } N_{huma} < N_{hums} \\ -N_{hums} & \text{if } N_{hums} \leq 0 \text{ and abs}(N_{hums}) > N_{hums,old} \\ N_{hums,new} & \text{otherwise} \end{cases} \tag{9}$$

Release of nitrogen from the active humic pool (N_{huma}) is similarly based on nminrl.f from the SWAT 2009 code. It depends on temperature T (°C), current soil moisture fraction compared to field capacity, and a tunable linear rate constant assuming no limitation (fraction/day).

The moisture dependency is a function of current soil moisture SW, field capacity FC, and wilting point WP. It is restricted by a tunable maximum value $\gamma_{W,max}$ and is calculated before calling PHREEQC following Equation 10:

$$\gamma_W = \begin{cases} 0.1 + 0.9 \cdot \sqrt{\frac{\max(0.0000001, SW - WP)}{FC - WP}} & \text{if } < \gamma_{W,max} \text{ and } > 0.05 \\ \gamma_{W,max} & \text{maximum allowed value} \\ 0.05 & \text{minimum allowed value} \end{cases} \tag{10}$$

The remaining calculations for N_{huma} occur within PHREEQC. The temperature dependency is described by Equation 11:

$$\gamma_T = 0.9 \cdot \frac{T}{(T + \exp(9.93 - 0.312 \cdot T))} + 0.1 \tag{11}$$

https://doi.org/10.5194/egusphere-2025-5823
Preprint. Discussion started: 27 January 2026

where $\gamma_T = 0.1$ is the minimum allowed value.

The overall calculations for N_{huma} follow Equation 12

$$N_{huma} = \begin{cases} 0 & \text{if } N_{huma,old} = 0 \\ 0 & \text{if } \sqrt{\gamma_T \cdot \gamma_W} < 0 \\ \beta_{act} \cdot \sqrt{1e^6} \cdot N_{huma,old} & \text{if } \sqrt{\gamma_T \cdot \gamma_W} > 1e^6 \\ \beta_{act} \cdot \sqrt{\gamma_T \cdot \gamma_W} \cdot N_{huma,old} & \text{otherwise} \end{cases} \tag{12}$$

where $N_{huma,old}$ is the current value of N_{huma} to be updated, i.e. the current amount of N left in the active humus pool. In contrast, loss of P from the humus P pool (P_{hum}) depends only on the current state of the two humus N pools (N_{hums} and N_{huma}, available within PHREEQC). SWAT 2009 module nminrl.f is also the basis for Equation 13:

$$P_{hum} = \begin{cases} \frac{1.4 \cdot \text{abs}\Delta N_{huma} \cdot P_{hum}}{N_{huma} + N_{hums}} & \text{if } \leq P_{hum,old} \\ P_{hum,old} & \text{otherwise} \end{cases} \tag{13}$$

where $P_{hum,old}$ is the current value of P_{hum} to be updated, i.e. the current amount of P left in humus.

By default, ARTEMIS releases CO_3^{2-} stoichiometrically along with ammonium from the active humus pool. The C:N mass ratio is 14:1 (Neitsch et al., 2011), corresponding to 16.3314 mol C mol N^{-1}. In PHREEQC, equilibration of the carbonate system is rapid compared to kinetics, such that CO_3^{2-} will be adjusted to CO_2(aq), H_2CO_3 or HCO_3^- for acidic or circum-neutral solution pH (Parkhurst and Appelo, 2013). Under open system conditions where the supply of CO_2 gas is effectively unlimited, H_2CO_3+CO_2(aq) is constant in accord with Henry's law (Henry, 1803; Stumm and Morgan, 1996).

2.3.3 Residue decomposition

For simplicity, ARTEMIS residues lose nutrients other than N and P at the same rate as they decompose and with the same stoichiometry as the original plants; otherwise the SWAT2009 scheme is followed with only N and P released from the two SOM pools. Microbially-mediated organic matter decomposition releases nitrogen in the form of ammonia (Kuypers et al., 2018), so ARTEMIS does not follow SWAT2009 in releasing nitrate (see also Figure 2).

N release from residue decomposition (N_{res}, Equation 14) is a function of temperature (γ_T, Equation 11), soil moisture relative to field capacity (γ_W, Equation 10), the C:N and C:P ratios of the residues, and a tunable residue mineralisation rate constant (β_{res}) assuming no limitations. The decay fraction for the timestep δ_{res} is given by Equation 14:

$$\delta_{res} = \begin{cases} 0 & \text{if } \sqrt{\gamma_T \cdot \gamma_W} < 0 \\ \beta_{res} \cdot \gamma_N \cdot \sqrt{1e^6} & \text{if } \sqrt{\gamma_T \cdot \gamma_W} > 1e^6 \\ \beta_{res} \cdot \gamma_N \cdot \sqrt{\gamma_T \cdot \gamma_W} & \text{otherwise} \end{cases} \tag{14}$$

https://doi.org/10.5194/egusphere-2025-5823
Preprint. Discussion started: 27 January 2026

Table 4. Tunable parameters in the ARTEMIS organic matter decomposition scheme

Parameter	Units	Default	Description
kNhumsday	per day	0.0001	Active humus pool decomposition rate (Biome-BGC kSOM4, Lawrence et al., 23 March 2020)
humactfrac	fraction	0.02	Fraction of humus which is active (SWAT default)
resCgfrac	g g^{-1}	0.58	Carbon to residue dry weight fraction (SWAT 2009 code default)
resNgfrac	g g^{-1}	0.0055	Carbon to residue dry weight fraction (SWAT 2009 code default)
resPgfrac	g g^{-1}	0.001	Phosphorus to residue dry weight fraction (SWAT 2009 code default)
Nresx	fraction	0.8	Fraction of decomposed residue nitrogen going to solution

where γ_N is given by Equation 15:

$$\gamma_N = \min \begin{cases} \exp\left(-0.693 \cdot \frac{\varepsilon_P - 200}{200}\right) & \text{where } \varepsilon_P = \min\left(5000, \frac{gC_{res}}{gP_{res} + \Sigma_P}\right) \\ \exp\left(-0.693 \cdot \frac{\varepsilon_N - 25}{25}\right) & \text{where } \varepsilon_N = \min\left(500, \frac{gC_{res}}{gN_{res} + \Sigma_N}\right) \\ 1 & \text{otherwise} \end{cases} \tag{15}$$

Here, Σ_N is the sum of exchangeable and plant-available N in grams of N ($[NH_3]$ + $[NH_4^-]$ + $[NO_3^-]$ + N_{exch}), Σ_P is the sum of phosphoric acid anions in solution in grams of P ($[PO_4^{3-}]$ + $[HPO_4^{2-}]$ + $[H_2PO_4^-]$), gC_{res} is the mass of carbon in the residue carbon pool (grams), gN_{res} is the mass of N in residues (grams), and gP_{res} is the mass of P in residues (grams).

The stoichiometry of release is specified in the PHREEQC KINETICS block, including release of nutrients to solution, CO_3^{2-} from microbial respiration to solution, and of N and P transfer to humus.

2.4 Nitrogen cycling

Nitrogen cycling affects the alkalinity of the soil solution, which can lead to longer-term soil acidification in the weathering arena. ARTEMIS represents many parts of the overall soil nitrogen cycle and its contributions to soil acidity (Fig. 2), including leaching, nitrification, denitrification, nitrogen uptake and fixation by plants, and mineralisation from organic matter, but does not yet explicitly represent gaseous phases or microbial dynamics. Ammonium and nitrate are redox-decoupled in ARTEMIS because nitrogen cycling processes in soils are microbially mediated. Nitrification, denitrification, fixation, and decomposition kinetics follow SWAT (2009 code, Neitsch et al., 2011).

https://doi.org/10.5194/egusphere-2025-5823
Preprint. Discussion started: 27 January 2026

The effect of temperature TC (Celsius) in the SWAT nitrification and denitrification scheme is given by Equation 16

$$\eta_{tmp} = \begin{cases} 0.41 \times \frac{TC-5°C}{10} & \text{for } TC \geq 5°C \\ 0 & \text{for } TC < 5°C \end{cases} \tag{16}$$

while that of soil moisture (following the 2009 version of the SWAT code rather than the documentation of Neitsch et al., 2011) is expressed by Equation 17:

$$\eta_{mois} = \begin{cases} \frac{(\text{SW}-\text{WP})}{\text{S25}-\text{WP}} & \text{for SW} < \text{S25} \\ 1 & \text{for SW} \geq \text{S25} \end{cases} \tag{17}$$

where SW is the current soil water content, WP is wilting point, FC is field capacity, and $\text{S25} = \text{WP} + 0.25 \cdot (\text{FC} - \text{WP})$, all in liters. The depth regulator for volatilisation is given by Equation 18

$$\eta_{depth} = 1 - \frac{\text{mm}}{\text{mm} + \exp 4.076 - 0.0305 \cdot \text{mm}} \tag{18}$$

where mm is the midpoint depth for the PHREEQC cell in millimeters. The final regulator for volatilisation expresses the effect of cation exchange and is hardcoded as $\eta_{CEC} = 0.15$ as in SWAT.

Total N lost from ammonium is given by Equation 19:

$$\text{N}_{lost} = \text{NH}_4 \times (1 - \exp(-\eta_{nit} - \eta_{vol})) \tag{19}$$

Here, $\eta_{nit} = \eta_{tmp} \cdot \eta_{moisture}$, and $\eta_{vol} = \eta_{tmp} \cdot \eta_{mois} \cdot \eta_{depth} \cdot \eta_{CEC}$

The fractions nitrified and volatilised are then calculated using expressions of the form $f = 1 - \exp(-\eta)$ (Reddy et al., 1979; Neitsch et al., 2011) where η is η_{nit} or η_{vol}. exchange on volatilisation. The rate law implemented for nitrification within PHREEQC likewise returns the total moles lost during nitrification, and calculates the speciation of dissolved ammonium and ammonia, but the fractions of those moles volatilised and nitrified are calculated by the PHREEQC wrapper before calling PHREEQC.

The rate law implemented for denitrification follows the 2009 SWAT code, and is also a function of soil moisture (Equation 20):

$$\gamma_{sw} = \max\left(0.05, \min\left(\text{maxsut}, 0.1 + 0.9 \cdot \sqrt{\frac{\max\left(0.0000001, \text{SW} - \text{WP}\right)}{\text{FC} - \text{WP}}}\right)\right) \tag{20}$$

where variables are defined as for Equation 17. γ_{sw} is restricted to the range 0.05 and "maxsut". (Table 4) The total amount of nitrate lost to denitrification is expressed by Equation 21:

$$\text{N}_{denit} = \begin{cases} \text{NO}_3^- \cdot (1 - \exp(-\beta_{denit} \cdot \eta_{tmp} \cdot orgC)) & \text{for } \gamma_{sw} \geq \gamma_{swthresh} \\ 0 & \text{for } \gamma_{sw} < \gamma_{swthresh} \end{cases} \tag{21}$$

where NO_3^- is the moles of nitrate in the soil solution, $orgC$ is the percent organic carbon, and $\gamma_{swthresh}$ is the minimum allowed value of γ_{sw} where denitrification is allowed to occur and should be less than "maxsut"; β_{denit}, "maxsut" and $\gamma_{swthresh}$ are tunable (Table 5).

https://doi.org/10.5194/egusphere-2025-5823
Preprint. Discussion started: 27 January 2026

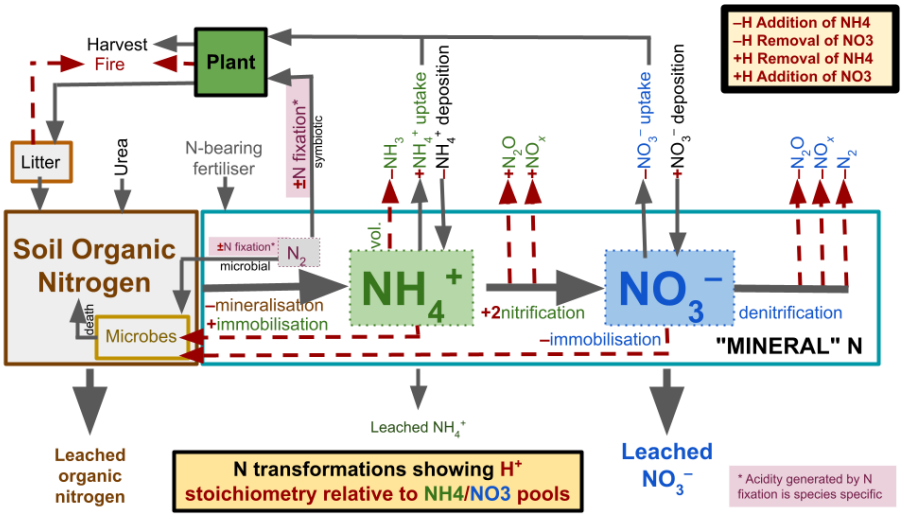

Figure 2. Nitrogen cycling in ARTEMIS. Red –, + show the stoichiometric contributions to acidity and alkalinity respectively. Fluxes shown as red dashed arrows are not yet represented. See Section 2.4 for details. Note: this diagram and Extended Data Fig. 3 of Kantzas et al. (2022), which described the Community Land Model nitrogen cycle, were both developed from the same original diagram by the same author (L Taylor).

Table 5. Tunable denitrification parameters in ARTEMIS

Parameter	Units	Default	Description
maxsut	ratio	3	Maximum ratio of plant-available water at current soil moisture to that at field capacity. Water is available to plants above the wilting point.
$\gamma_{swthresh}$		1.1	Threshold above which denitrification may take place (must be lower than "maxsut").
β_{denit}		1.4	Denitrification exponential rate coefficient.

2.5 Fertilisers and other treatments

ARTEMIS requires the chemical formula and molar mass of any treatment(s) to be applied. A limited range of fertilisers can be interpreted by the preprocessor (Table 6). Fertilisers are added in pelletised form, and their dissolution aims to replicate slow-release solid fertilisers (Ritger and Peppas, 1987) as a function of time and initial amount only (Eqn. 22):

$$M/M0 = k \times (t^n) \tag{22}$$

where $M0$ is the initial moles of nutrient, M is current moles of nutrient, t is time (elapsed hours), k is a rate constant and n is an exponent. This equation is the default for ARTEMIS and assumes uncoated pellets. However, a two-stage dissolution process for coated pellets is also supported. Following Sofyane et al. (2020), an initial fast stage lasting $5-10$ hours is followed by

https://doi.org/10.5194/egusphere-2025-5823
Preprint. Discussion started: 27 January 2026

Table 6. Fertilisers which can be processed automatically by ARTEMIS

Name	Formula	Description
UANx	1:1 Urea:NH_4NO_3	N is x percent of the total mass
MOP	KCl	Muriate of potash
SOA	$(NH_4)_2SO_4$	Sulphate of ammonia
DAP	$(NH_4)_2(HPO_4)$	Diammonium phosphate
MAP	NH_4HPO_3	Monoammonium phosphate

Table 7. Pellet dissolution parameters

Coating	k_1 (hour^{-1})	n_1	k_2 (hour^{-1})	n_2
Uncoated	0.8869	0.59	0	0
Priamine 1L	0.1054	1.06	0.6008	0.11
Priamine 2L	0.0216	1.90	0.2954	0.25
Priamine/solvent 1L	0.1237	1.48	0.6244	0.09
Priamine/solvent 2L	0.0695	1.79	0.2691	0.24

continued slower dissolution of the remaining material. In ARTEMIS, the initial stage lasts up to seven hours. There are several possible sets of parameters for different types of coatings (Table 7), and the user can specify other parameters as required.

2.6 Plant dynamics

Nutrient uptake in ARTEMIS is demand-based and depends on plant biomass and crop type. If plant growth curves are not provided as input forcings, they can be calculated as described by Neitsch et al. (2011) if peak biomass, sowing and harvest times are included in the input timetable file. Growth calculations depend on parameters from a version of the SWAT crop database (Arnold et al., 2011) for ARTEMIS which has some data added, including whether the plant is a legume or not. ARTEMIS does not calculate photosynthesis.

2.6.1 Crop growth and leaf area index

Growth is controlled by temperature via "phenological heat units" which are given by the cumulative sum (Equation 23):

$$\text{PHU} = \sum_{i=1}^{\text{maturity}} (T_i - T_{base}) \tag{23}$$

where T_i is the mean temperature (°C) of day i and sum is over all the days of plant growth to maturity. The base temperature T_{base} (°C), below which no growth occurs, is given for each crop in the SWAT crop database (Arnold et al., 2011). The

https://doi.org/10.5194/egusphere-2025-5823
Preprint. Discussion started: 27 January 2026

preprocessor calculates plant growth curves and phenological heat units attained following Neitsch et al. (2011) based on the crop type and the peak biomass and harvest data.

For annual crops, phenological heat units accumulate after sowing and and are reset to zero following harvest. For crops needing a drying period, harvest is beyond maturity and Neitsch et al. (2011, Table 5:1-1) suggests that 1.2 is a reasonable value for the fraction of phenological heat units attaned (f_{PHU}) at harvest. Hay-cutting takes place when f_{PHU} = 0.6, and for other annual crops harvest occurs when f_{PHU} = 1. Grain filling starts when the decrease in leaf area index (LAI) due to senescence exceeds LAI increase due to growth. Grain filling ends when f_{PHU} is 1. The fraction of maximum LAI attained comprises the growth curve which is calculated following Neitsch et al. (2011) (Equation 24):

$$f_{LAI} = \begin{cases} \frac{f_{PHU}}{(f_{PHU} + \exp LAI_{shp1} - LAI_{shp2} \cdot f_{PHU})} & \text{when } f_{PHU} \leq f_{PHU,sen} \\ \frac{f_{PHU}}{(f_{PHU} + \exp LAI_{shp1} - LAI_{shp2} \cdot f_{PHU})} \cdot \frac{1 - f_{PHU}}{1 - f_{PHU,sen}} & \text{when } f_{PHU} > f_{PHU,sen} \end{cases} \quad (24)$$

where LAI_{shp1} and LAI_{shp2} are shape parameters and $f_{PHU,sen}$ is the PHU at which senescence exceeds growth. Total LAI is calculated as LAI $= LAI_{max} \cdot f_{LAI}$, where LAI_{max} is the maximum LAI for the crop type. LAI_{shp1}, LAI_{shp2}, $f_{PHU,sen}$, and LAI_{max} are all from the SWAT crop database.

Biomasses are calculated by multiplying the peak biomass by the fraction of LAI attained. This biomass curve is partitioned into roots and aboveground biomass using the peak root biomass from the timetable, and the amount of biomass attained following commencement of grain filling is assigned to grain rather than vegetative biomass.

Canopy height H_{can} follows Neitsch et al. (2011) (Equation 25):

$$H_{can} = H_{can,max} \cdot \sqrt{f_{LAI}} \quad (25)$$

where the maximum canopy height $H_{can,max}$ comes from the SWAT crop database. Root depth attained by the growing roots (z_{root}, cm) is given by Equation 26:

$$z_{root} = \min\left(z_{sow}, \frac{f_{LAI}}{0.4}\right) + z_{sow} \quad (26)$$

where z_{sow} is sowing depth (cm) and 0.4 is the PHU at which maximum root length is attained (SWAT default). By default, all roots are assumed to be alive.

2.6.2 Nutrient uptake

Equation 27 for nitrogen uptake (Neitsch et al., 2011) requires several parameters from the SWAT crop database: the biomass fraction of N at emergence (f_{N1}), maturity (f_{N3}) and when 50% of PHU has been attained (f_{N2}).

$$f_N = (f_{N1} - f_{N3}) \cdot \left[1 - \frac{f_{PHU}}{f_{PHU} + \exp\left(N_{shp1} - N_{shp2} \cdot f_{PHU}\right)}\right] + f_{N3} \quad (27)$$

The shape coefficients N_{shp1} and N_{shp2} were calculated by Equations 28 and 29:

$$N_{shp1} = \ln\left[\frac{f_{N2}}{\left(1 - \frac{f_{N2} - f_{N3}}{f_{N1} - f_{N3}}\right)} - f_{N2}\right] + N_{shp2} \cdot f_{N2} \quad (28)$$

https://doi.org/10.5194/egusphere-2025-5823
Preprint. Discussion started: 27 January 2026

$$N_{shp2} = \frac{\left(\ln\left[\frac{f_{N2}}{\left(1-\frac{f_{N2}-f_{N3}}{f_{N1}-f_{N3}}\right)} - f_{N2}\right] - \ln\left[\frac{f_{N3}}{\left(1-\frac{f_{N4}-f_{N3}}{f_{N1}-f_{N3}}\right)} - f_{N2}\right]\right)}{f_{N3} - f_{N2}} \tag{29}$$

where $f_{N4} = f_{N3} + 0.00001$ to avoid possible division by zero. These shape coefficients have been added to a version of the crop database, and are included in the same directory as the PHREEQC databases developed for ARTEMIS.

Equations of the same form as Equations 27, 28 and 29 are used to calculate P uptake. Once the fractions of N and P expected in biomass are calculated, they are multiplied by the biomass and then the daily molar demand for N and P are calculated before running PHREEQC. N uptake from the PHREEQC cells ($N_{up,cell}$) is given by Equation 30:

$$N_{up,cell} = \frac{\left(-\exp\left(-N_{up,dis} \cdot \frac{z_b}{z_{LR}}\right)\right) - \left(1 - \exp\left(-N_{up,dis} \cdot \frac{z_t}{z_{LR}}\right)\right)}{\left(1 - \exp\left(-N_{up,dis}\right)\right)} \tag{30}$$

where z_b is the bottom depth (cm) of the PHREEQC cell (or the depth live roots have attained, whichever is smaller), z_t is the top depth (cm) of the PHREEQC cell, z_{LR} is the depth attained by living roots (cm), and $N_{up,dis}$ is a parameter controlling the shape of the depth distribution (default: 20). Larger values of $N_{up,dis}$ result in more uptake from upper layers and less from lower layers.

The uptake of other nutrients follows the uptake of nitrogen scaled by the molar ratio of the nutrient to N in biomass. A default .csv file of stoichiometries for crops is provided for ARTEMIS.

Michaelis-Menten kinetics (Michaelis and Menten, 1913, 2013) are employed during uptake (Equation 31):

$$R_{up} = D \cdot \left(\frac{C}{K_m + C} - \frac{C_{min}}{K_m + C_{min}}\right) \tag{31}$$

where R_{up} is the rate of uptake (mol cell^{-1} day^{-1}), D is the precalculated demand (mol cell^{-1} day^{-1}), C is the concentration of the nutrient in solution, K_m is the molar concentration at half the maximum rate of uptake, and C_{min} is the minimum concentration allowed for uptake (all concentrations in mol kg$^{-1}_{water}$). PHREEQC will not attempt to take up a nutrient unless its concentration C is greater than C_{min}.

In the case of nitrogen, ammonium and nitrate are taken up separately but both contribute to fulfilling the N demand. When taking up ammonium, PHREEQC will remove the current nitrate uptake from the total N demand; therefore, nitrate uptake is effectively preferred. This is not the case in forests where trees may preferentially take up ammonium (Arnold, 1992; Neumann and Römheld, 2012), so these uptake kinetics may require adjustment if such ecosystems are to be modelled.

https://doi.org/10.5194/egusphere-2025-5823
Preprint. Discussion started: 27 January 2026

2.6.3 Nitrogen fixation

Model nitrogen fixation by legumes depends on the plant growth stage (Equation 32) as described by Neitsch et al. (2011, Section 5:2.3.1.1):

$$\mathrm{N}_{fix} = \begin{cases} 0 & \text{for } f_{PHU} \leq 0.15 \\ 6.67 \cdot f_{PHU} - 1 & \text{for } 0.15 < f_{PHU} \leq 0.3 \\ 1 & \text{for } 0.3 < f_{PHU} \leq 0.55 \\ 3.75 - 5 \cdot f_{PHU} & \text{for } 0.55 < f_{PHU} \leq 0.75 \\ 0 & \text{for } 0.75 > f_{PHU} \end{cases} \tag{32}$$

where f_{PHU} is the fraction of phenological heat units attained and N_{fix} is the total plant nitrogen demand satisfied by fixation.

Model nitrogen fixation also depends on how much ammonium and nitrate the plant has taken up from solution. N fixation therefore helps satisfy plant demand for N, but it can also be a source of acidity. This extra proton efflux is tunable, with a default value of 0.01 mol H extruded per mol N fixed based on a slight discrepancy between excess cation uptake and pHstat measurements observed by Van Beusichem (1982) in a study of peas.

Free-living microbial nitrogen fixation is not represented at present.

2.7 Hydrology

In land models, hydrological fluxes through the Critical Zone (Anderson, 2005; Brantley et al., 2007) from canopy through the soil profile encompass rain and snow precipitation, canopy interception, overland runoff, infiltration into the soil, percolation through the soil, evaporation from the canopy, evaporation from the soil, transpiration and drainage. Of these, precipitation is required by ARTEMIS although many of the other fluxes can be supplied as forcings. If not provided as a forcing, infiltration is set as follows (Equation 33):

$$Infiltration = Precipitation - Snowfall + Snowmelt - Interception_{\text{canopy}} - Runoff_{\text{overland}} \tag{33}$$

where all variables are given in mm day^{-1} and are set to zero if not provided. Snow can also be calculated as described in Section 2.7.1.

Within PHREEQC, there are three ways to move water between cells: ADVECTION, TRANSPORT and MIX. The first two methods expect the PHREEQC cells to be the same size with the same water content, with all the water in each cell shifting to the next cell at a specified rate. ADVECTION is therefore essentially a type of bucket model. TRANSPORT is similar but calculates intercell dispersion/diffusion; it is also possible to define stagnant cells such that solutes can diffuse between the stagnant and advecting cells.

ARTEMIS does not require its PHREEQC cells to be the same size or to have the same water content, so it uses PHREEQC's MIX instead of ADVECTION or TRANSPORT. MIXing fractions for combining solutions of each cell with each other cell at each timestep must be defined ahead of time. This approach means that evapotranspiration from individual cells can be

https://doi.org/10.5194/egusphere-2025-5823
Preprint. Discussion started: 27 January 2026

modelled, along with differences in soil texture and water-holding capacity, changes in water table position, and potentially also hydraulic lift or preferential flow between cells. It also means that cells can be defined that reflect observed soil layers of different thickness. The default spatial extent of PHREEQC cells in ARTEMIS is one square meter of land. In contrast to many of the examples in the PHREEQC documentation where cells contain exactly one litre of water, (Parkhurst and Appelo, 2013), cell water content in ARTEMIS will be the actual water content for an actual soil layer.

A simplistic method for calculating percolation fluxes and soil moisture is supplied with the preprocessor (Equation 34):

$$W_{j,t+1} = W_{j,t} + inperc_{j,t} - T_{j,t} - E_{j,t} - outperc_{j,t} \tag{34}$$

where $W_{j,t}$ is the total water in layer j at time t, the start of the current model day (mm). Percolation into layer j takes place at the start of the day, followed by percolation out of layer j as percolation is assumed to be faster than transpiration T and evaporation E from layer j (see Section 2.7.3). $W_{j,t-1}$ is maintained above wilting point (see below), and $outperc_{j,t}$ is only permitted if $W_{j,t+1}$ is above field capacity. This method requires daily infiltration along with the porosity, field capacity and wilting point for each of the PHREEQC cells. The latter three values can be calculated from soil layer texture (percent sand, silt and clay) by the preprocessor using one of three pedotransfer functions: Cosby et al. (1984, their Tables 4 or 5) or Noilhan and Lacarrère (1995). The function from Table 5 of Cosby et al. (1984) is the default for both ARTEMIS and for the Community Land Model (CLM5, Lawrence et al., 23 March 2020). Alternatively, the fractional moisture content for every PHREEQC cell at every timestep can be supplied as a forcing, in which case percolation will be forced to maintain that specified moisture.

In the absence of specified initial water content, the soil moisture is initialised at field capacity. Drainage, if not provided as a forcing, will be calculated as the infiltration less the sum of evapotranspiration from the model cells. This sum will generally be less than the total evapotranspiration from the whole soil due to the approximately exponential depth profile of evapotranspiration (Section 2.7.3).

Flow into a cell takes place when the total water will not exceed porosity; excess water will be rerouted to deeper layers under the assumption that macropore flow takes place. Flow out of a cell takes place when the total water is above field capacity. Evapotranspiration is allowed to remove water to wilting point; excess demand will be switched to other cells if the current cell does not contain enough water.

The caveats, assumptions and limitations inherent in this crude hydrological approach are as follows:

1. Canopy interception can be supplied as a forcing.

2. Overland runoff can be supplied as a forcing, but is not currently calculated. Possible future versions could include the SCS (Rallison and Miller, 1981; Neitsch et al., 2011) curve-number method, or the SIMTOP (Niu et al., 2005) approach used in CLM5 (Lawrence et al., 23 March 2020).

3. Infiltration is treated the same way as inter-cell percolation, if it is not provided as a forcing. No ponding is allowed. Better approaches could include the SCS method mentioned above, or solving the Green-Ampt equation (Green and Ampt, 1911).

https://doi.org/10.5194/egusphere-2025-5823
Preprint. Discussion started: 27 January 2026

4. This is essentially a bucket model; water flows when above field capacity. It does not attempt to calculate unsaturated hydraulic conductivity, for example. A more sophisTiCATed approach could be to solve Richards' equation (Richards, 1931).

5. Hygroscopic water (tightly bound to solid surfaces) is assumed to equal water below wilting point. This water is completely mixed with the water that may flow; there are no stagnant PHREEQC cells.

6. Preferential or macropore flow only occurs when the total water content of the percolating water plus cell water would exceed cell porosity. By default, this macropore flow routes water to the next PHREEQC cell with enough air-filled space to accept it; alternatively the water can be routed to the bottom cell, filling porosity from the bottom up. A better approach could involve implementation of separate stacks of cells for different porosity classes.

7. Hydraulic lift is not implemented, although there is a crude attempt to transpire or evaporate water from other parts of the soil if the current cell is too dry.

8. Model infiltration occurs at the start of the model day.

9. Percolation is assumed to take place much faster than evapotranspiration, so all percolation is completed before evapotranspiration takes place.

10. Evapotranspiration is instantaneous by default.

11. Transpiration water has the same chemistry as the soil cell water by default; the user may specify whether the plant is allowed to take up nutrients from this water, or transpire pure water leaving all solutes behind. There is no way to select which solutes are included in the transpiration stream.

12. PHREEQC can change cell water content via processes such as weathering or precipitation of solid water-bearing phases. Because soil water content for the following day has been calculated ahead of time by the preprocessor or otherwise specified by the user, ARTEMIS corrects it at the start of every day prior to calling PHREEQC so that it cannot deviate too much from what was specified.

13. Porosity and other soil texture parameters affecting hydrology are not currently dynamic and do not change as a result of feedstock applications (de Oliveira Garcia et al., 2020) or secondary phase precipitation (e.g., Noiriel et al., 2016).

2.7.1 Snow and sublimation

The treatment of snowfall, snowpack and sublimation follows Neitsch et al. (2011). Precipitation is deemed to be snow if the air temperature is below 1°C.

Snow temperature is assumed to be like air temperature, and melting is a function of season and a 0.5°C threshold temperature for melting (Equation 35)

$$b_{mlt} = 0.5 \cdot (6.9 + 1.4 + (6.9 - 1.4) \cdot \sin(2\pi \cdot (\text{DOY} - 81) \cdot 5)) \quad (35)$$

https://doi.org/10.5194/egusphere-2025-5823
Preprint. Discussion started: 27 January 2026

where the factors 6.9 and 1.4 (mmH2O/day/C) are for the summer and winter solstices respectively (Huber et al., 1988; Neitsch et al., 2011). Melting is then described by Equation 36:

$$S_{mlt} = b_{mlt} \cdot \left[\frac{T_{snow} + T_{air}}{2} - T_{mlt} \right] \tag{36}$$

where T_{air} should be the maximum daily temperature, but where only the daily mean is provided, it is the daily mean (°C). T_{snow} is the snowpack temperature, here assumed to be equal to air temperature, and $T_{mlt} = 0.5$°C is the maximum temperature for snow to remain unmelted. Note that because ARTEMIS is a point model which runs at the scale of 1m^2 of land by default, snow cover is assumed to be 1 or 0.

Sublimation is assumed to equal the minimum of the total evapotranspiration and the amount of water in the snowpack, which accrues each day with snowfall.

2.7.2 Total evapotranspiration

Evapotranspiration (ET) from the soil system is required to run ARTEMIS, so that water evaporated or transpired from each soil layer can be calculated. If canopy interception is provided, it will be subtracted from ET to get soil evapotranspiration. ARTEMIS does not calculate actual evapotranspiration, but a function to calculate potential evapotranspiration by various methods is provided.

Both soil evaporation and transpiration can be provided as forcings, but if not available, they can be calculated from total evapotranspiration.

2.7.3 Evapotranspiration from soil

The fraction of soil water evaporation from a particular PHREEQC soil cell E_{cell} (Equation 37) follows Neitsch et al. (2011, Section 2:2.3.3.2):

$$E_{cell} = \frac{z_b}{z_b + \exp\left(2.374 - 0.00713 \cdot z_b\right)} - \frac{z_t}{z_t + \exp\left(2.374 - 0.00713 \cdot z_t\right)} \tag{37}$$

while the fraction of transpiration from a PHREEQC soil cell T_{cell} (Equation 38) follows Neitsch et al. (2011, Section 2:2.3.3.2):

$$T_{cell} = \frac{1}{1 - \exp\left(-\beta_{water}\right)} \cdot \left(\left[1 - \exp\left(-\beta_{water} \cdot \frac{z_b}{z_{LR}} \right) \right] - \left[1 - \exp\left(-\beta_{water} \cdot \frac{z_t}{z_{LR}} \right) \right] \right) \tag{38}$$

where z_t and z_b are top and bottom depths of the PHREEQC cell (cm), and z_{LR} is the depth currently attained by live roots (cm). β_{water} is a settable parameter describing the distribution of water uptake with depth. The default value for β_{water} is 10, meaning that 50% of water uptake will occur in the upper 6% of the root zone (Neitsch et al., 2011, Section 5:2.2).

The extent of vegetation cover (m^2 m$_{land}^{-2}$) is set to V=min(LAI,1) so that bare ground is 1-V. It follows that the fraction of total evapotranspiration from a PHREEQC cell is given by Equation 39:

$$f_{ET} = V \cdot T_{cell} + (1 - V) \cdot E_{cell} \tag{39}$$

https://doi.org/10.5194/egusphere-2025-5823
Preprint. Discussion started: 27 January 2026

2.8 Total soil respiration

Soil respiration is the flux of CO_2 gas from the soil surface on account of both root and microbial respiration in the soil. This respiration can lead to soil pCO_2 1–2 orders of magnitude higher than that of the above-ground atmosphere (Oh et al., 2005).

If total soil respiration has not been provided as a forcing, it can be calculated following a general relationship between annual net primary productivity (NPP) and annual soil respiration (SR) published by Raich and Schlesinger (1992) (Equation 40):

$$SR_{day} = 1.24 \cdot DWT_{day} \cdot Cbiorat + \frac{24.5}{365} \tag{40}$$

where $NPP_{day} = DWT_{day} \cdot Cbiorat$ is the daily carbon increment (g). $Cbiorat$ is the fraction of the dry weight (DWT) which is carbon, with default value 0.45 (Table 4.12 of Fageria et al., 2010). SR_{day} is the daily carbon flux (g) from the soil surface, and the Y intercept of Equation 40 is assumed to represent heterotrophic respiration. This is the default method for crops other than *Sorghum* and oil palm.

2.8.1 *Sorghum* respiration

If the crop being modelled is sorghum, then soil respiration will be calculated following Choudhury (2001). First, the gross primary productivity (GPP) increment for the day is calculated given an observed average carbon use efficiency in growth chambers of 60%. Converting to moles of carbon, daily gross primary productivity $GPP_{day,mol}$ is given by Equation 41:

$$GPP_{day,mol} = \frac{DWT_{day} \cdot Cbiorat}{0.6 \cdot 12.01} \tag{41}$$

where DWT_{day} and $Cbiorat$ are defined above (Section 2.8).

Next, the growth conversion efficiency Y_g is required (Equation 42, Choudhury, 2001, his Equation 3).

$$Y_g = 0.814 - 0.051 \cdot fr_N \cdot 100 \tag{42}$$

where fr_N is the plant N concentration (% dry matter). Specific plant respiration for *Sorghum bicolor* at 20°C is R_{20} ~0.04 gC_{resp} gC^{-1}_{DWT} day^{-1} with a best-fit $Q_{10} = 1.3$ (Kirschbaum and Mueller, 2001, their Figure 1). Maintenance respiration (mol C day^{-1}) is then given by Equation 43:

$$R_m = \frac{0.04 \cdot Cbiorat \cdot DWT_{tot}}{12.01} \cdot Q_{10}^{(\frac{T_{air}-20}{10})} \tag{43}$$

Total plant growth respiration (mol C day^{-1}) is given by Equation 44:

$$R_g = \max\left[0, (1 - Y_g) \cdot (GPP_{day,mol} - R_m)\right] \tag{44}$$

Total autotrophic respiration is $R_m + R_g$ and root respiration is given by Equation45:

$$R_r = (R_m - R_g) \cdot \frac{DWT_{root}}{DWT_{tot}} \tag{45}$$

where DWT_{root} is the dry weight of the roots and DWT_{tot} is the dry weight of the whole plant.

https://doi.org/10.5194/egusphere-2025-5823
Preprint. Discussion started: 27 January 2026

The contribution of *Sorghum* roots to total soil respiration has been observed to be 75–87% (Fu et al., 2002), so heterotrophic respiration R_h is taken as 20% of root respiration R_r during the growing season. During the fallow season, the following sigmoid function is applied to ensure a smooth transition of R_h to the next growing season (Equation 46):

$$R_{h,fday} = (R_{h,gday1} - R_{h,gdayf}) \cdot \left[1 - \frac{1}{\left(1 + \exp\left(-\frac{(DOY - DOY_{gdayf} - 0.5 \cdot N_{fdays})}{10}\right)\right)}\right] + R_{h,gday1} \tag{46}$$

where the fallow season includes those days with no plant mass ($fday$), N_{fdays} is the number of days in the fallow season, DOY is the day of year, $gday1$ is the first day of the growing season, $gdayf$ is the finalday of the growing season.

Soil respiration is then set to $R_h + R_r$.

2.8.2 Oil palm respiration

Oil palm (*Elaeis guineensis*) respiration follows the PALMSIM model (Hoffmann et al., 2014) with parameters from Dufrene et al. (1990).

Root respiration (mol C day^{-1}) is given by Equation 47:

$$R_r = \frac{(0.023 \cdot DWT_{root,day} + 0.0022 \cdot DWT_{root,tot})}{30.026} \tag{47}$$

where the molar mass of CH_2O is 30.026 g mol^{-1} and DWT is the dry weight in grams.

Lamade et al. (1996, their Table 2) measured the root contributions to total soil respiration for wet and dry conditions near the trunk, interrow, and several points in between. The total respiration R_{tot} is given by Equation 48:

$$R_{tot} = \frac{R_r}{(b \cdot 0.768 + (1 - b) \cdot 0.51)} \tag{48}$$

where b is given by Equation 49:

$$b = \sum_{cells} \left(\frac{SW_{cell}}{V_{cell}} - \frac{WP_{cell}}{(FC_{cell} - WP_{cell})} \cdot f_{cell} \right) \tag{49}$$

where f_{cell} is the depth fraction of the model soil for the PHREEQC cell, which has current water content SW_{cell}, volume V_{cell}, wilting point WP_{cell}, and field capacity FC_{cell}.

2.9 CO_2 gas partial pressures in soil

The ARTEMIS preprocessor sets the target saturation state of CO_2 gas in PHREEQC's EQUILIBRIUM_PHASES block using the partial pressure of CO_2 gas (Parkhurst and Appelo, 2013). These partial pressures (C_z, atm) are calculated using an analytical solution to the diffusion equation (Equation 11 of Cerling, 1991) (Equation 50)

$$C_z = M_{O_2} \cdot \frac{\phi_s(0) \cdot z_{char}^2}{D_s} \left(1 - e^{-\left(\frac{z}{z_{char}}\right)}\right) + C_{atm} \tag{50}$$

https://doi.org/10.5194/egusphere-2025-5823
Preprint. Discussion started: 27 January 2026

An optional term accounting for finite soil depth L (cm) derived by Mark Lomas for the weathering code of Kantzas et al. (2022) can be included (Equation 51):

$$C_z = M_{O_2} \cdot \frac{\phi_s(0) \cdot z_{char}^2}{D_s} \left(1 - e^{-\left(\frac{z}{z_{char}}\right)}\right) + \left(\frac{\phi_s(0) \cdot z \cdot z_{char}}{D_s} \cdot e^{-\left(\frac{L}{z_{char}}\right)}\right) + C_{atm} \tag{51}$$

In these equations, C_{atm} is the partial pressure of CO_2 gas in the atmosphere (atm), z is depth (cm), z_{char} is a characteristic depth of CO_2 production, L is depth (cm) to an impermeable layer (e.g., the water table or bedrock), $\phi_s(0) = R_{tot} \cdot R_{gas} \cdot T_K$ is soil respiration (cm atm s^{-1}), with T_K being temperature (Kelvin), R_{tot} total soil respiration (mol cm^{-2} s^{-1}), and the gas constant is $R_{gas} = 0.08206 \cdot 1000$ (cm^3 atm $Kelvin^{-1}$ mol^{-1}). D_s is CO_2 diffusivity in soil (cm^2 s^{-1}), which is given by Equation 52:

$$D_s = D_{air} \cdot \left(\frac{P^0 \cdot T_K}{P \cdot (25 + 273.16)}\right)^{1.823} \cdot \tau \cdot \theta_{air} \tag{52}$$

where D_{air} is diffusivity of CO_2 in air under standard conditions (default 0.144 cm^2 s^{-1}), T_K is temperature (Kelvin), τ is tortuosity (default 0.6), and θ_{air} is air-filled porosity (fraction). By default, experiments are assumed to take place at sea level such that atmospheric pressure $P = P^0$, where P^0 is pressure at sea level in atm. Note that D_{air} and P can also be provided as input parameters.

The true air-filled porosity is given by Equation 53:

$$x_{trueair} = \max(0, x_{por} - x_{mois}) \tag{53}$$

where x_{por} is total porosity and x_{mois} is the soil moisture either provided as a forcing or calculated as described in Section 2.7. However, Equations 50 and 51 are not valid for wet soils.

If soil moisture has been prescribed as a forcing, the air-filled porosity will already exist. In this case, ARTEMIS will attempt to find the water table by checking the cell moistures from the bottom cell upwards. The water table will be located in the uppermost fully saturated cell, and this cell will be treated as an impermeable layer, below which no CO_2 gas production takes place. Note that perched water tables cannot be accommodated with this crude approach.

If air-filled porosity is not given, an "effective" air-filled porosity will be estimated following Equation 54 under the assumption that high soil moisture is transient for any given day:

$$x_{air} = \begin{cases} \max(x_{por} - x_{fc}, x_{por} - x_{mois}) & \text{if } x_{por}, x_{fc}, x_{mois} \text{ all available} \\ \max(0.09, x_{por} - x_{mois}) & \text{if } x_{por}, x_{mois} \text{ both available} \end{cases} \tag{54}$$

where x_{fc} is field capacity. In the absence of field capacity, the minimum valid air-filled porosity is taken as 0.09 (Solomon and Cerling, 1987). Note that the true air-filled porosity will also be calculated (Equation 53) so it is possible to check whether the preprocessor has applied either of the above thresholds. If the simplistic hydrology described in Section 2.7 has been applied, this problem with wet cells is less likely to arise as water flows when field capacity is exceeded.

The effect of O_2 deficit on respiration will be calculated if the Michaelis-Menten constant K_m is given (Equation 55):

$$M_{O_2} = \frac{O_2}{O_2 - K_m} \tag{55}$$

https://doi.org/10.5194/egusphere-2025-5823
Preprint. Discussion started: 27 January 2026

where O_2 units are the fraction of O_2 gas in the atmosphere (default: 0.21) under the assumption that the sum of O_2 + CO_2 is effectively constant. If K_m is not given it is set to zero, so that $M_{O_2} = 1$. Note, however, that oxygen does not have its own production function, so is not represented well enough in ARTEMIS to model waterlogged soil (e.g., rice paddies).

During the fallow period, it is assumed that microbial populations follow the final root distribution before harvest if heterotrophic respiration is available. Otherwise, atmospheric pCO_2 is assumed.

A characteristic depth for the distribution of living roots is estimated with Equation 56, a modified version of the equation for transpiration (see Equation 38 in Section 2.7.3):

$$x_i = \frac{V}{1 - \exp(-\beta_{water})} \cdot \left(\left[1 - \exp\left(-\beta_{water} \cdot \frac{i}{z_{LR}} \right) \right] - \left[1 - \exp\left(-\beta_{water} \cdot \frac{i}{z_{LR}} \right) \right] \right) \tag{56}$$

where V=min(LAI,1) is the extent of vegetation cover, β_{water} describes the distribution of transpiration with depth (Section 2.7.3), x is the fraction of transpiration taking place from depth i, ranging ranging from 1 to the bottom depth of the modeled soil in increments of 1 cm. The absolute value of the smallest difference between x and its mean $\bar{x}$ for living roots (down to their maximum depth z_{LR}) gives the characteristic live root depth z_{char}, and is calculated for each timestep.

The characteristic depth $z_{char,het}$ (cm) for heterotrophic respiration can be set as a parameter, or it can be calculated from the mean depth of soil organic carbon if the latter is given (Equation 57):

$$z_{char,het} = \frac{\sum_i (z_i \cdot \mathrm{SOC}_i)}{\sum_j \mathrm{SOC}_i} \tag{57}$$

where SOC_i is the organic carbon content for layer i and z_i is the midpoint depth for layer i.

Otherwise, it will be set to the mean value of the characteristic depth for root respiration (Equation 58) under the assumption that microbial distribution follows root distribution (Equation 58)

$$z_{char,het} = \frac{\sum_i (z_i \cdot x_i)}{\sum_i x_i} \tag{58}$$

where x_i is given by Equation 56.

The overall characteristic depth for respiration is estimated with Equation 59:

$$z_{char} = \frac{z_{char,root} \cdot R_{root} + z_{char,het} \cdot R_{het}}{R_{tot}} \tag{59}$$

2.9.1 Soil CO_2 evolution with time

A key limitation of ARTEMIS is that gas diffusion between soil layers and the soil surface is not modelled. Although the partial pressure of CO_2 gas is high in soils (Oh et al., 2005), the total volume of air is determined by porosity and soil moisture. The moles of CO_2 gas available for consumption via carbonic acid weathering at any given time is therefore limited by the available moles of CO_2 gas in the air-filled pore space. In a fully open system, this air-filled pore space is in contact with the atmosphere and any CO_2 consumed is quickly replenished. This may be the case for topsoils where feedstocks have been applied, and is therefore the default condition for ARTEMIS. Closed-system conditions are more likely to occur beneath the water table (Engesgaard and Christensen, 1988), where our analytical solution to the diffusion equation is not valid (Cerling, 1991).

https://doi.org/10.5194/egusphere-2025-5823
Preprint. Discussion started: 27 January 2026

As previously done in other PHREEQC-based models (e.g., Kelland et al., 2020), fully open-system conditions are replicated in ARTEMIS by using the default 10 mol cell^{-1} when initialising CO_2 gas in PHREEQC's EQUILIBRIUM_PHASES data block (see PHREEQC documentation, Parkhurst and Appelo, 2013), along with the calculated saturation state of pCO_2 gas described in Section 2.9 above. This means that moles of CO_2 gas are effectively unlimited. PHREEQC will calculate the initial dissolved H_2CO_3 using Henry's law and the current saturation state of CO_2 gas (given by its partial pressure). However, note that CO_3^{2-} is by default released during decomposition of organic matter (Sections 2.3.2 and 2.3.3), such that heterotrophic respiration is partially dynamic. Where residues are decomposing, this release can be non-negligible, but may be switched off if desired.

It is also possible to calculate the initial daily moles of both CO_2 and O_2 gas in each model soil cell using the ideal gas law (Equation 60):

$$M_{gas} = P_{gas} \cdot \frac{(V_{pores} - V_{H_2O})}{RT_K} \quad (60)$$

where the moles of gas M_{gas} (L) are assumed to be related to the partial pressure P_{gas} (atm), and the air-filled pore volume $V_{air} = V_{pores} - V_{H_2O}$ is a function of the volumes of pores and the precalculated soil moisture V_{H_2O} (Section 2.7). R is the gas constant (atm L)/(mol Kelvin) and T_K is the temperature (Kelvin). If this option is chosen, the ARTEMIS soil crudely represents partially-open conditions where moles of gas are replenished but limited. Saturation indices and moles for CO_2 and O_2 are updated daily to the precalculated values described above, assuming that root and microbial respiration along with diffusion from the atmosphere will replenish their concentrations on daily timesteps. Under these conditions, release of CO_3^{2-} by decomposing organic matter helps replenish the inorganic carbon supply on sub-daily timesteps.

This approach to CO_2 gas moles in the soil cells could be improved by modelling diffusion explicitly, defining CO_2 as part of a fixed-volume gas, and treating root and microbial respiration as reactions changing the gaseous CO_2 and O_2 concentrations. The air volume would need to be modified daily with PHREEQC's GAS_PHASE_MODIFY data block (Parkhurst and Appelo, 2013) to account for changing moisture in the soil cells. At present, the choice of open or partially-closed system applies throughout the soil column, but a depth dependency would be more realistic.

2.9.2 Nitrogen gases

Aqueous NO_2^- and gaseous N_2, N_2O and NO are not currently modelled. Volatilisation of ammonium to ammonia and the release of N_2 gas during denitrification are both modelled, but without an explicit representation of gas diffusion, ARTEMIS does not yet model N gas emissions.

2.10 Tillage and particle mixing into soil

Particle transport of surface-applied silt-sized particles has previously been quantified for several soil types (e.g., Fishkis et al., 2010). Attachment and detachment of $< 3\mu$m-diameter particles via surface interaction and filtration of larger particles being transported by percolating fluid (e.g., Fishkis et al., 2009) is not presently supported in ARTEMIS, nor are bioturbation processes. Feedstocks and other treatments are assumed to be mixed into the soil to a tillage depth specified by the user.

https://doi.org/10.5194/egusphere-2025-5823
Preprint. Discussion started: 27 January 2026

2.11 Elemental fluxes and carbon dioxide removal (CDR)

At the end of a ARTEMIS run, arrays of PHREEQC outputs for each PHREEQC cell (influent, soil cells and leachate) at each timestep These outputs include solute concentrations in solution and on exchangers and surfaces, along with the moles and saturation indices of each solid and gas phase in the system.

From these arrays, ARTEMIS calculates total fluxes of each element delivered in the leachate, along with fluxes of key elements released from feedstock and separate fluxes from native soil phases. These are returned both as mol m^2_{land} day^{-1} and as cumulative fluxes (mol m^2_{land}). Total moles of phases and key geochemical species in the model soil are also calculated.

2.11.1 CDR via leached solutes

ARTEMIS calculates several fluxes related to carbon dioxide reduction (CDR), returned as tCO_2 ha^{-1} day^{-1} for the incremental flux and tCO_2 ha^{-1} for the cumulative flux. These include CO_2 consumption, which is widely reported for rivers as a measure of CO_2 drawdown due to weathering of primary minerals in watersheds (e.g., Gaillardet et al., 1999). This is calculated as the sum of the concentrations of bicarbonate and carbonate anions in the leachate, multiplied by the daily leached water flux Q (Equation 61):

$$CO_{2,cons}(i) = Q(i) \cdot \left(\left[HCO_3^-\right](i) + \left[CO_3^{2-}\right](i) \right) \tag{61}$$

Cumulative CO_2 consumption is given by Equation 62:

$$cCO_{2,cons}(i) = \sum_{j=1}^{i} \left[Q(j) \cdot \left(\left[HCO_3^-\right](j) + \left[CO_3^{2-}\right](j) \right) \right] \tag{62}$$

where i is the timestep (day). Incremental (daily) CDR calculated from total leached DIC (H_2CO_3+ HCO_3^-+CO_3^{-2}) is also returned (Equation 63):

$$CO_{2,DIC}(i) = Q(i) \cdot \left([H_2CO_3](i) + \left[HCO_3^-\right](i) + \left[CO_3^{2-}\right](i) \right) \tag{63}$$

Cumulative leached DIC is given by Equation 64:

$$cCO_{2,DIC}(i) = \sum_{j=1}^{i} \left[Q(j) \cdot \left([H_2CO_3](j) + \left[HCO_3^-\right](j) + \left[CO_3^{2-}(j)\right] \right) \right] \tag{64}$$

Downstream carbon dynamics in rivers, estuaries and near-shore environments are not accounted for in these fluxes. However, if bicarbonate is the dominant anion, daily CO_2 consumption can be approximated as the sum of the base cation equivalents (Equation 65):

$$CO_{2,cat}(i) = Q(i) \cdot \left(2 \cdot \left[Ca^{2+}\right](i) + 2 \cdot \left[Mg^{2+}\right](i) + \left[Na^+\right](i) + \left[K^+\right](i) \right) \tag{65}$$

Cumulative cationic CO_2 consumption is given by Equation 66:

$$cCO_{2,cat}(i) = \sum_{j=1}^{i} \left[Q(j) \cdot \left(2 \cdot \left[Ca^{2+}\right](j) + 2 \cdot \left[Mg^{2+}\right](j) + \left[Na^+\right](j) + \left[K^+\right](j) \right) \right] \tag{66}$$

https://doi.org/10.5194/egusphere-2025-5823
Preprint. Discussion started: 27 January 2026

CO_2 consumption calculations via Equations 61 and 62 account for all major ions and, if these have been defined, organic anions as well (e.g., Taylor et al., 2021). Nitrate and organic anions in particular may not accompany base cations to the open ocean (Taylor et al., 2021) where long-term carbon sequestration may occur (Renforth and Henderson, 2017).

Additional versions of the cationic CDR fluxes (Equations 65, 66) are also returned with a correction for storage in the marine water column (Renforth and Henderson, 2017, their Equation 11). The cationic CDR is multiplied by the efficiency of sequestration (Equation 67):

$$\eta(i) = \left(S_{ocean} \cdot 10^{-3.009} + 10^{-1.519}\right) \cdot \ln\left(p\mathrm{CO}_2(i)\right) - S \cdot 10^{-2.100} - T_{ocean} \cdot p\mathrm{CO}_2(i) \cdot \left(S_{ocean} \cdot 10^{-7.501} - 10^{-5.598}\right) - T_{ocean} \cdot 10^{-2.337} + 10^{-0.102} \quad (67)$$

where S_{ocean} is salinity (default 35‰), T_{ocean} is mean ocean surface water temperature (default 17.0°C), and $p\mathrm{CO}_2(i)$ is the partial pressure of CO_2 in equilibrium with seawater, here equal to that of the atmosphere (ppmV) at timestep i. The default values above (Renforth and Henderson, 2017, their Section 2.3) are ARTEMIS parameters which can be changed. η is returned as an array.

2.11.2 Carbonate mineral contribution to CDR

Sequestration on geological timescales via carbonate precipitation in the oceans (e.g., Berner et al., 1983) is not accounted for. However, total carbonate mineral accumulation in the soil during the model run is returned. In addition to returning time-series arrays for all the individual phases specified in the input phases file, all mineral phases containing CO_3 are summed over the soil cells to create a single total time series with units of $\mathrm{tCO}_2\ \mathrm{ha}^{-1}$. Pre-existing and additions of carbonates in timetabled feedstock or liming treatments are subtracted from this array.

2.11.3 Statistics generated for comparisons with observations

If observations (e.g., solution chemistry) have been provided, ARTEMIS finds the appropriate model day and PHREEQC cell corresponding to each observation. Model outputs for those days and cells can then be compared to the observations, and a set of statistics is generated for each column j in the relevant file of observations. Where several depths and days of observations are provided in one observation file, overall statistics are generated. These calculations begin with Equation 68:

$$\mathrm{diff}_i = \mathrm{model}_i - \mathrm{obsn}_i \quad (68)$$

where diff_i is the difference between model output and observation i. We can calculate the root mean square error (RMSE) with Equation 69:

$$\mathrm{RMSE}_j = \sqrt{\mathrm{mean}\left(\mathrm{diff}^2\right)_j} \quad (69)$$

Generally, solute concentrations are logged (e.g., $\log_{10}[\mathrm{Ca}^{2+}]$) so that one RMSE unit is one order of magnitude of difference. Note that this means solutes are treated similarly to pH (pH = $-\log_{10}[\mathrm{H}^+]$). RMSE does not indicate whether the model is high

https://doi.org/10.5194/egusphere-2025-5823
Preprint. Discussion started: 27 January 2026

or low compared to the observations, so we calculate bias for each column using Equation 70:

$$\text{bias}_j = \text{mean}\left(\text{model}\right)_j - \text{mean}\left(\text{obsns}\right)_j \tag{70}$$

We can also calculate the root mean square distance

$$\text{rmsd}_j = \frac{\sqrt{\sum_i^{N_j}\left(\left(\text{model}_{i,j} - \text{obsn}_{i,j}\right)^2\right)}}{N_j} \tag{71}$$

A centred root mean square distance (crmsd) can be calculated using Equation 72:

$$\text{crmsd}_j = \sqrt{\frac{\sum_i^{N_j}\left(\left(\text{model}_{i,j} - \text{mean}\left(\text{model}\right)_j\right) - \left(\text{obsn}_{i,j} - \text{mean}\left(\text{obsns}\right)_j\right)^2\right)}{N}} \tag{72}$$

The rmsd and bias values are suitable for placement on a target diagram (e.g. Jolliff et al., 2009), while crmsd is suitable for Taylor diagrams (Taylor, 2001) along with the correlation coefficient (calculated using MATLAB's corrcoef function).

3 Example: Using ARTEMIS to model solute export for a long-term ERW field trial

The aim of this example is to model CDR via ion export for a long-term enhanced weathering experiment in the United States "Corn Belt" (e.g., Blanc-Betes et al., 2021; Kantola et al., 2023; Val Martin et al., 2023; Epihov et al., 2024; Beerling et al., 2024). First, we describe the site and the data used to parameterize ARTEMIS. We calibrate ARTEMIS by comparing its Ca and Mg release outputs to feedstock weathering rates reported by Beerling et al. (2024). Then, we evaluate model outputs by comparison with measured drainage water chemistry. We can then demonstrate how key processes of nitrogen cycling and sorption affect drainage water chemistry and calculate lag times for ion export, considering future feedstock application rates. Finally, we consider possible effects of faster-weathering feedstocks on CDR.

In addition to the PHREEQC database mentioned above (Section 2.1), ARTEMIS requires a considerable array of inputs to run. These include thermodynamic data for all solid phases to be modelled, geochemical rate law parameters for phases weathering kinetically, daily climate data, the timetable of agricultural and feedstock-application events at the site, crop data, and soil texture and chemical data. Optional inputs include the initial feedstock surface area and particle size distribution (PSD) data, and actual field measurements for comparison with model outputs. Minimal climate forcings include precipitation, mean temperature, and total evapotranspiration, which must be provided on a daily timestep.

3.1 Energy Farm enhanced weathering field trial

The Energy Farm is operated by University of Illinois Department of Crop Science. It is located in Champaign County, Illinois, south of Urbana (40.0628 N, -88.1961 E) in the northernmost reaches of the Embarras watershed. The temperate climate and experimental design have been described by Kantola et al. (2023), who reported mean annual precipitation 1051mm and mean annual temperature 11°C.

https://doi.org/10.5194/egusphere-2025-5823
Preprint. Discussion started: 27 January 2026

Starting in late 2016, 50 t ha^{-1} of a metabasalt from the Blue Ridge mountains ("Blueridge", Lewis et al., 2021) was applied to soils under soy-maize-maize rotation between 2016 and 2019 inclusive, after which the Blueridge feedstock was replaced with a different feedstock ("Pioneer", first applied in autumn 2020). In this crop rotation system, the feedstock was tilled into the soil each autumn, to a depth of 18 cm. Ca and Mg feedstock release rates for the soy-maize-maize rotation during the Blueridge period between 2016 and 2020 were recently determined by Beerling et al. (2024) from analyses of soil Ca and Mg concentrations normalised to an immobile tracer (Ti) (Reershemius et al., 2023). These measurements provide a way to calibrate ARTEMIS.

3.2 Site data for the Energy Farm

The site is relatively flat, with relatively poorly drained mollisols developed under native tallgrass prairie vegetation from the Richland loess (Endres et al., 2001). These mollisols are considered to be highly productive when drained; drains can vary between 1–1.5 m deep in the Embarras watershed (David et al., 2009). The Richland loess overlies Wisconsinian ground moraines of the calcareous Batestown till (Endres et al., 2001), which may occur above the Energy Farm 1.3m drain depth in some localities (e.g., Champaign, Sharp, 1974). This site has been in agricultural production (primarily maize and soybean) for over 100 years.

3.2.1 The Flanagan soil

Four mollisols (Flanagan, Dana, Elburn and Drummer) occur in the five individual enhanced weathering plots under maize-maize-soy rotation at the Energy Farm (Beerling et al., 2024; Soil Survey Staff, 2025). Rock dust was applied to one large "B0" plot (3.8 ha, Dana with some Flanagan soils) with drains 1.3 m deep and four small (0.7 ha) plots without drains (Beerling et al., 2024). The Flanagan silt loam is dominant in two of the small plots and present in a third; two plots have multiple soil types (Soil Survey Staff, 2025). Small plots were divided into treated and untreated subplots (Beerling et al., 2024).

Along with the Drummer silty clay loams, the Flanagan silt loams are among the most common soils in Champaign County (Alexander et al., 1974). They are fine, montmorillonitic, mesic Aquic Argiudolls (Fehrenbacher et al., 1984); the Dana and Elburn silt loams are fine-silty, mesic Aquic (Elburn) or Typic (Dana) Argiudolls. The three Argiudolls are less poorly drained than the Drummer silty clay loams, which are fine-silty, mixed, mesic Typic Haplaquolls (Fehrenbacher et al., 1984).

Chemical analyses for Flanagan horizons down to 183 cm are available from Alexander et al. (1974, Table 5, Profile 6). These data include exchangeable Ca, Mg, Na and K, along with CEC. Here, we have assumed that the monoprotic carboxylic sites on organic matter contributed to the analysed CEC, reducing the exchange capacity assigned to clays (Section 2.1). Where the exchangeable base cations did not account for all the CEC, we assumed that Al comprised the exchangeable acidity.

Flow paths to drains are likely to curve through soil below drain depth (Hooghoudt, 1940, Fig. 8), and these paths are not rigorously represented in this 1-D model. However, the model soil (3) includes the underlying layers and the chemistry of the percolating water can be calculated in all layers.

https://doi.org/10.5194/egusphere-2025-5823
Preprint. Discussion started: 27 January 2026

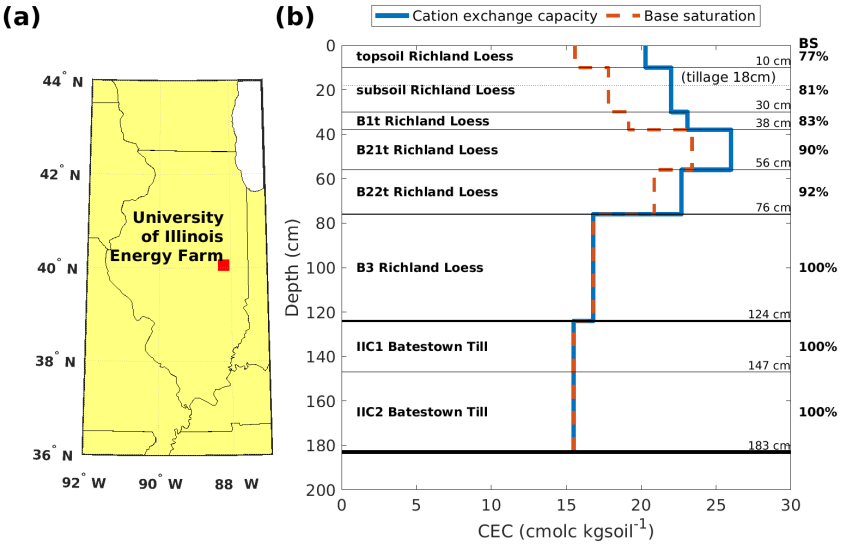

Figure 3. Location of Energy Farm (a) and model soil cells (b) based on published chemical analyses from the Flanagan soil series (Alexander et al., 1974, Table 5, Profile 6). The model topsoil and subsoil follow the sampling regime of Beerling et al. (2024) rather than the observed horizons Ap (0–23 cm) and A12 (23–30 cm). BS (base saturation, %) is shown on the right Y axis.

3.2.2 Soil parent materials

The mineralogy of the Richland Loess (sample 331, Frye et al., 1962) and the Batestown Till (sample P754, Willman et al., 1963) was reported for the same suite of minerals: garnet, epidote, hornblende, quartz, microcline, albite, hypersthene, augite, smectite and illite, along with black and "other" heavy opaque fractions. For the model, the black opaque fraction was divided evenly between magnetite and ilmenite, and the other heavy opaque fraction was assigned to anatase, a common secondary titanium-bearing mineral which serves a sink for Ti in the model. Smectite was assigned only to depths where swelling potential was known to be moderate rather than low (Table 7, Alexander et al., 1974).

The Batestown Till is calcareous, so the mineralogical proportions from Willman et al. (1963) were rescaled to accommodate calcite and dolomite observed at the top of the Mahomet I-74 bridge section in Champaign County (Appendix 1, Wickham, 1979). The contact between the loess and till is abrupt (Sharp, 1974), and carbonates are not observed to be present in the uppermost soil (Soil Survey Staff, 2025), so no carbonate phases were assigned to the loess layers.

3.2.3 Climate forcings

We forced ARTEMIS using monthly climate and hydrological outputs from the Community Land Model (CLM5, Lawrence et al., 23 March 2020) with the medium mitigation Shared Socioeconomic Pathway (SSP2) (Beerling et al., 2025, Extended Data Fig 1 and Supplementary Figs. 3–6). Time-series outputs (2015–2070) for the nearest CLM5 gridpoint to our site (see 3.1)

https://doi.org/10.5194/egusphere-2025-5823
Preprint. Discussion started: 27 January 2026

were resampled to a daily timestep for use in ARTEMIS. These included soil temperature with depth, air temperature, infiltration, evaporation from soil and canopy, and transpiration CLM5 outputs.

We did not use the CLM5 soil moisture, which was often well above field capacity. Because the ARTEMIS approach to soil CO_2 gas (Section 2.9) assumes high air-filled porosity, we used the crude default hydrology described in Section 2.7 which usually maintains soil moisture at or below field capacity.

Major ion chemistry for our incoming percolation is an average for the rainwater collected over the period starting 2020-11-17 15:15 and ending 2020-11-24 15:15 by the National Trends Network (e.g., McCammon and Deyette, 2025) under the National Atmospheric Deposition Program for Champaign, IL, USA, downloaded on Friday 25 June 2021. Percent error in the charge balance of this solution is 0.0351%.

3.3 Calibrating ARTEMIS

The aim of calibration was to achieve model Ca+Mg cumulative release from the "blueridge" feedstock within one standard error of the Ca+Mg weathering release reported by Beerling et al. (2024) for the soy-maize-maize rotation between 2016 and 2020. Modeled Ca and Mg release were also compared to those reported by Beerling et al. (2024) individually. After identifying problematic feedstock phases, their representation and scalings were adjusted using the options described in Section 2.2 in several five-year test runs. Initial feedstock reactive surface area (1.02 $m^2 g^{-1}$, measured by N_2 gas sorption) and particle size distribution data for all runs were taken from Lewis et al. (2021). We tried several combinations of scalings and options for representing the feedstock phases (see the User Guide for details of a subset of calibration runs). For the final calibrated model run (Figure 4), we slightly increased the initial RSA by a factor of 1.1, and treated titanite and apatite as implicit phases to be released faster than the kinetically-weathering phases by a factor of five.

We adjusted one additional parameter following comparison with observed nitrate concentrations in lysimeter and drainage waters. Because nitrate and ammonium are redox-decoupled, denitrification can be the dominant process controlling nitrate concentrations in this model. Denitrification is dependent on attaining a threshold soil moisture, and a parameter controlling this threshold ($\gamma_{swthresh}$, see Table 5) was reset to 1.0 when test runs suggested that nitrate fluxes would be far too high with the default value ($\gamma_{swthresh} = 1.1$). This adjustment resulted in model nitrate concentrations of the right order of magnitude (Table A1) but did not bring annual denitrification rates into line with literature values during maize years (Figure B1).

3.4 Validating the model

A wide range of samples from the Energy Farm were collected and analyzed over the course of the ERW experiment. Of these, the major ion chemistry of the drainage water is particularly relevant to quantifying CDR via solute export. Drains integrate waters following flowpaths which may have passed through deeper layers, such as the calcareous till present at or below the physical drain depth of 130 cm in the large treated "B0" maize-soy plot at the Energy Farm (Fig. 3b). However, macropore flow could mean that the observed drainage solution chemistry may be better represented by flow through shallower layers. Lateral heterogeneity in the soil layers can also contribute to differences between the physical drain depth and an "effective" drain chemistry depth.

https://doi.org/10.5194/egusphere-2025-5823
Preprint. Discussion started: 27 January 2026

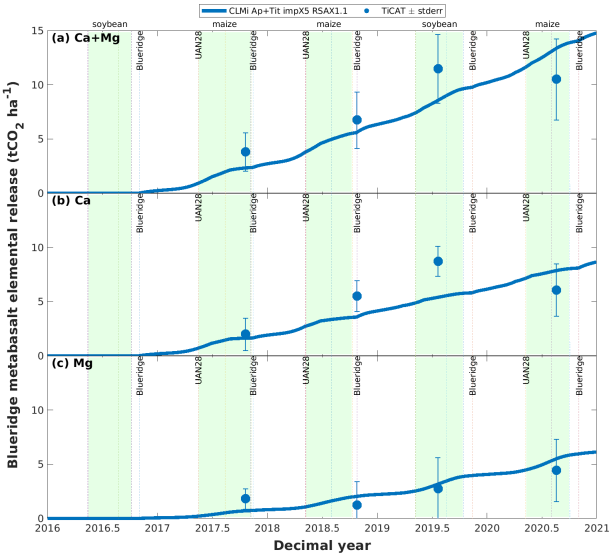

Figure 4. Comparison between the best-calibrated model run (solid line) measured (a) Ca + Mg, (b) Ca and (c) Mg cation release rates. Measured data are from Beerling et al. (2024), blue dots. The thick blue solid line represents the best model run used in subsequent experiments in the current study.

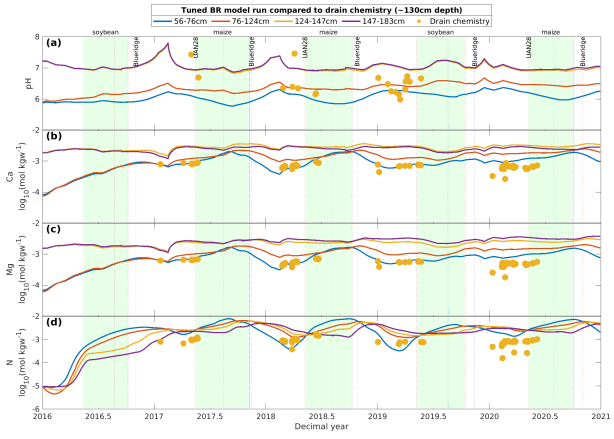

Figure 5. Comparison between the chemistry of the four deepest soil layers in the calibrated model (solid lines) and observed drainage chemistry (gold disks). (a) pH, (b) Ca, (c) Mg, and (d) nitrate. The observations have been given the same colour as the layer containing the physical drain depth of 130 cm.

Therefore, it was important to compare the model solution chemistry for both shallower and deeper layers than the physical drain depth (Fig. 5). This was done for the four layers between 56cm and 183cm (Fig. 3b). The best-fit model layer (Ap-
890 pendix A) was the B22t Richland Loess layer between 56 and 76 cm deep, suggesting macropore flow to the drains. It is also likely that the model soil layers differ from the actual mean soil layers at this site.

https://doi.org/10.5194/egusphere-2025-5823
Preprint. Discussion started: 27 January 2026

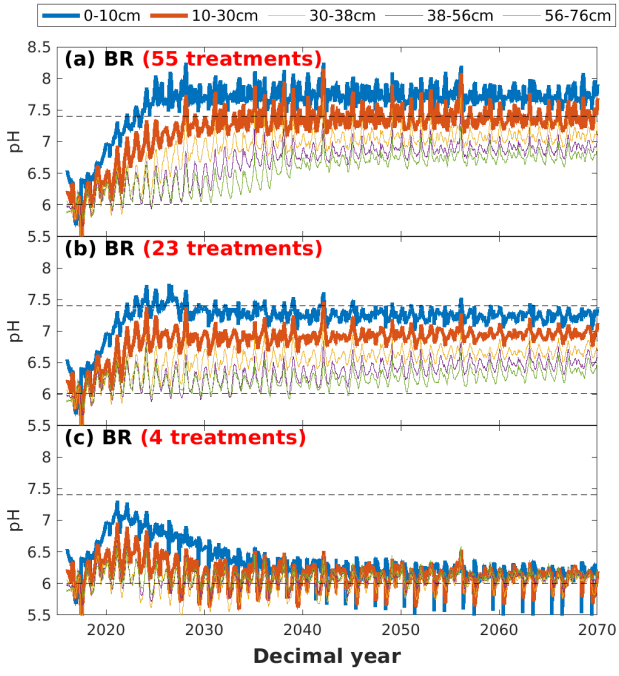

Figure 6. Long-term solution pH given a total of (a) 55, (b) 23 or (c) four treatments with the Blueridge metabasalt feedstock. Horizontal dashed lines indicate pH thresholds for liming (pH 6) or possible SO4 treatment (pH 7.4, (Fernández and Hoeft, 2009)).

3.5 Estimating long-term pH effects and lag times for solute-based CDR

As the available CLM5 runs had extended through 2070, it was possible to repeat the most recent timetabled crop rotations and treatments into the future. In addition to a control run without feedstock, the Blueridge calibrated run was extended through 2070 under three different scenarios:

1. Annual applications of the Blueridge feedstock (55 treatments including the initial four)
2. Triannual applications of the Blueridge feedstock after 2020 (23 total treatments including the initial four)
3. Cease applying feedstock after the initial four treatments

One aim of these extended runs was to determine solution pH response in the rooting zone, as Illinois farmers are advised to consider remedial treatments if pH exceeds 7.4 (Fernández and Hoeft, 2009). Results suggest that pH could exceed recommended limits in the topsoil if the Blueridge feedstock were applied annually for 55 years, from 2016 through 2070 (Fig. 6). Reducing the frequency or amount of feedstock applications can ameliorate this issue. After 2024, pH remains below 8.3 in the 55-treatment run partly because calcite accumulates in the top 30cm of soil at a rate of 0.6 tCO_2 ha^{-1} $year^{-1}$). The other runs do not accumulate carbonates in the rooting zone; pH is largely controlled by sorption.

https://doi.org/10.5194/egusphere-2025-5823
Preprint. Discussion started: 27 January 2026

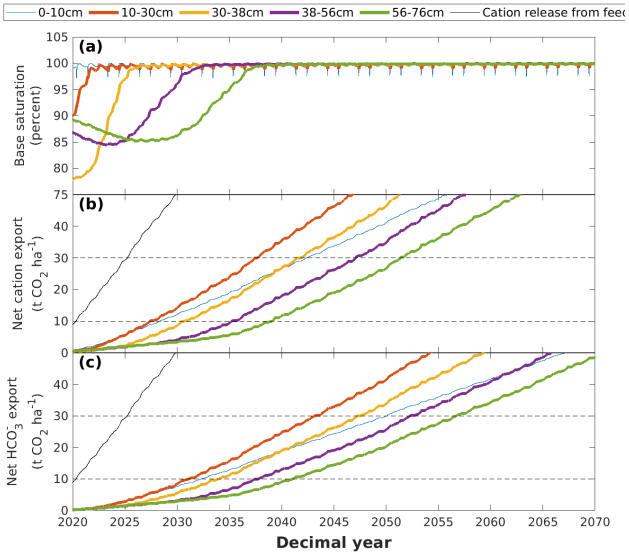

Figure 7. (a) Model base saturation for soil layers, and CDR based on (b) cation or (c) bicarbonate fluxes through each soil layer as compared to cations released from feedstock. Results are shown for 55 annual treatments with Blueridge feedstock. The lag times (Table 8) for each soil layer and CDR removal (dashed horizontal lines showing 10 and 30 tCO_2 ha^{-1}), are computed as the differences between cation (b) and bicarbonate (c) fluxes for each soil layer and cation release from feedstock (thin black lines)). Note that the times when these fluxes pass each soil layer are later than the times for base saturation, bicarbonate fluxes take longer than cation fluxes, and lag times increase with both layer and CDR horizon.

Skipping annual applications and applying rock dust every third year after 2020 suppresses pH, but will also limit CDR via solute export from the drains. Based on an increasing number of field and laboratory studies (e.g., Hasemer et al., 2024; Vienne et al., 2024) and recent modelling work (Kanzaki et al., 2025), it is clear that sorption delays the export of solutes from the soil column. With ARTEMIS, we can compare a "potential CDR" from solute release from the feedstock to solute export in the drains for a desired CDR horizon, and also with the time required to achieve 99% base saturation. Here, Ca+Mg release is chosen as the "potential CDR" as it can be related to the TiCAT measurements at the site.

With annual applications for 55 years, a few decades are required to achieve the potential CDR suggested by weathering release rates (Fig 7, Table 8). These lag times exceed the times required to achieve 99% base saturation because cation exchange is not the only sorption process modelled (Sections 2.1, 3.2.1). However, all export lag times become prohibitively long for climate mitigation when fewer treatments are applied (Fig 8). With 23 treatments, base saturation down to the effective drain depth of 76 cm is barely approached by the end of the run in 2070. With four treatments, 99% base saturation is only achieved in the topsoil, and CDR via ion export is not achieved before 2070.

https://doi.org/10.5194/egusphere-2025-5823
Preprint. Discussion started: 27 January 2026

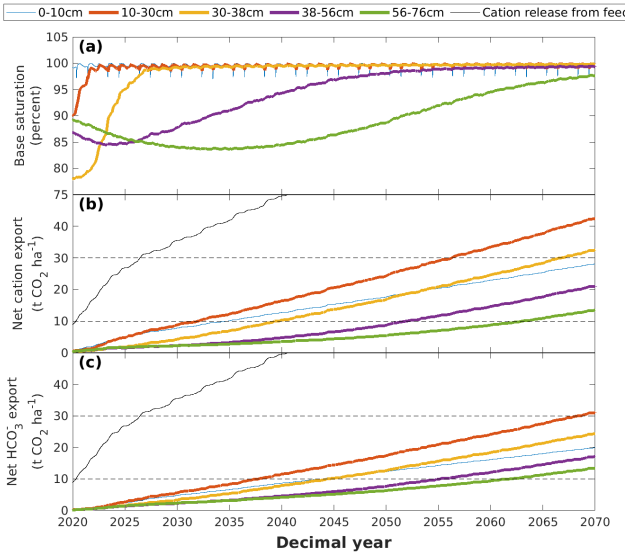

Figure 8. (a) Base saturation and CDR based on (b) cation and (c) bicarbonate fluxes through each layer as compared to cations released from feedstock (thin black lines), computed for a run with 23 treatments over 55 years with Blueridge feedstock. Note that this 55-year model run was not long enough for cation or bicarbonate fluxes from the effective drainage layer (green lines) to reach 20 tCO_2 ha^{-1}.

3.6 Net nitrification and nitric acid effects

Because ARTEMIS represents key elements of the nitrogen cycle (Section 2.3, Fig. 2), we examine how nitric acid affects solute export using three five-year model runs:

1. Standard calibrated run including nitrification and denitrification (Section 3.3, Figure 4)
2. Run ignoring nitrification and denitrification (using "noNkinetics" keyword), but otherwise like the standard calibrated run
3. Control run ignoring feedstock (using "nodust" keyword) but otherwise like the standard calibrated run, including nitrification and denitrification

ARTEMIS has a "noNkinetics" keyword that can be applied at runtime. If this keyword is used, nitrification, denitrification and N fixation kinetics will be ignored; nitrate and ammonium supply from influent and fertilisers, nitrate and ammonium uptake by plants, and release of ammonium from decaying organic matter and ureolysis proceed as per normal. Likewise, there is a "nodust" keyword which means that the feedstock will be ignored.

In our example, the supply of ammonium from UAN and organic matter exceeds the supply of nitrate from UAN, so nitrification (conversion of ammonium to nitrate) should increase nitrate concentrations and nitric acid weathering, resulting in lower bicarbonate concentrations and lower CDR via bicarbonate export. Denitrification (conversion of nitrate to nitrogen gas) reduces nitrate concentrations on days with sufficient plant-available water. Here, the moisture threshold for denitrification has

https://doi.org/10.5194/egusphere-2025-5823
Preprint. Discussion started: 27 January 2026

been set to $\gamma_{swthresh} = 1.0$ (Section 3.3, Equation 20), equivalent to field capacity. Because evapotranspiration reduces soil moisture in the upper soil layers, we expect net nitrification (nitrification−denitrification) reduces bicarbonate fluxes in our standard calibrated run (Fig. 4). The run ignoring net nitrification, however, should have higher bicarbonate export as nitric acid weathering will be modest.

Compared to our standard calibrated run which includes net nitrification (Fig. 9, blue curves), the run ignoring net nitrification (red curves) does show higher bicarbonate export, but it also shows lower cation export. This is because base cations accompany nitrate being flushed through the soil, and the nitrate flux is lower in the run without net nitrification. These cations maintain charge balance of the percolating water. Comparison with the control run (gold curves, with net nitrification but ignoring feedstock) suggests that net nitrification has a larger effect on CDR via solute export than the metabasalt treatment.

Net nitrification also reduces solution pH in the soil layers (solid lines, Fig. 9a) compared to the run without N kinetics (dashed lines). Although both runs show increasing base saturation in the second layer after the first metabasalt treatment (Fig. 9b), the run without net nitrification responds more quickly due to reduced nitrate and cation export.

Use of the "noNkinetics" keyword does not completely eliminate nitric acid weathering due to supply of nitrate from UAN and rainwater. Nevertheless, it seems clear that nitric acid production from net nitrification increases cation export and reduces bicarbonate export. Results of these five-year ARTEMIS runs suggest that net nitrification affects these export fluxes to a greater extent than the metabasalt feedstock. However, these results should be treated with caution as the other major anions (Cl^- and SO_4^{2-}) and denitrification and nitrate export all compare poorly to observations (Table A1, Fig. B1).

3.7 Exploring process effects with different feedstocks

Using the same forcings, input files and application rates described above for the Energy Farm, a set of twelve five-year runs was undertaken to demonstrate some capabilities of ARTEMIS. These runs encompass the period when the "blueridge" feedstock was applied, with the late 2020 application of Pioneer feedstock replaced with Blueridge in these runs.

There were four feedstock cases:

CTL No feedstock

Fo Pure forsterite (Mg_2SiO_4)

Wo Pure wollastonite ($CaSiO_3$)

BR "Blueridge" metabasalt, calibrated as described above in Section 3.3

The forsterite (Fo) and wollastonite (Wo) feedstocks are expected to weather more quickly than the metabasalt (BR) that was applied during the first few years of the Energy Farm experiments. CTL, Wo and Fo runs are like the BR runs in every respect except for feedstock.

To illustrate and explore the effects of specific processes on CDR, the following three "model option" runs were done for each of the feedstock cases:

Standard run As the calibrated run discussed in Section 3.3, but with feedstock set to one of the feedstock cases above.

https://doi.org/10.5194/egusphere-2025-5823
Preprint. Discussion started: 27 January 2026

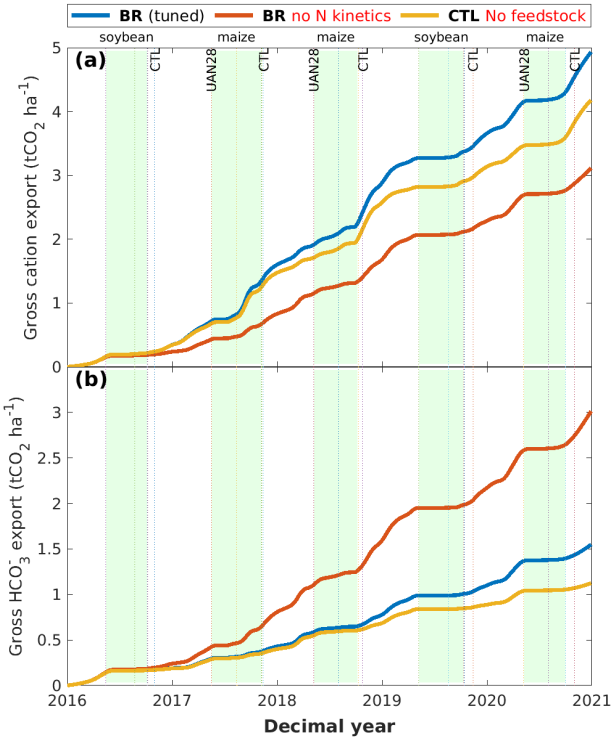

Figure 9. Gross CDR via solute export at the effective drain depth of 76cm for the calibrated run (blue curves) and an otherwise identical run with N kinetics switched off (orange curves). A control run with N kinetics but no feedstock (gold curves) is included for comparison.

No sorption No cation exchange or sorption to hydrous ferric oxide or organic matter

Closed system Like the standard runs, but with the moles of CO_2 in soil cells set using $PV = nRT$ (Section 2.9). In these runs, the CO_2 gas available for consumption is effectively limited.

The "no sorption" option was chosen because not all models represent cation exchange or surface complexation, and this option will allow estimation of the errors that may be expected when calculating CDR via exported solutes without these processes. Because the water table has been observed above the drains at the Energy Farm, the "closed system" option may indicate whether CO_2 limitation could occur

As expected given their relative dissolution kinetics, cation release from feedstock followed the sequence Wo>Fo>BR (Fig. 11), as did calcite accumulation (Fig. 12). Cumulative bicarbonate and carbonate ion export (CO_2 consumption, Sec. 2.11) from the effective drain depth (76 cm) identified in Section 3.4 does not follow this sequence; at this depth, cumulative CO_2 consumption is only slightly higher than the control runs for all three feedstocks, except when sorption is excluded (Fig. 13). Without sorption, Fo would deliver CO_2 consumption nearly an order of magnitude greater than it would with sorption (Fig. 13). The other feedstocks are less responsive to sorption, with CO_2 consumption limited by calcite deposition for the fast-weathering Wo feedstock, and by slower weathering rates for the BR feedstock.

https://doi.org/10.5194/egusphere-2025-5823
Preprint. Discussion started: 27 January 2026

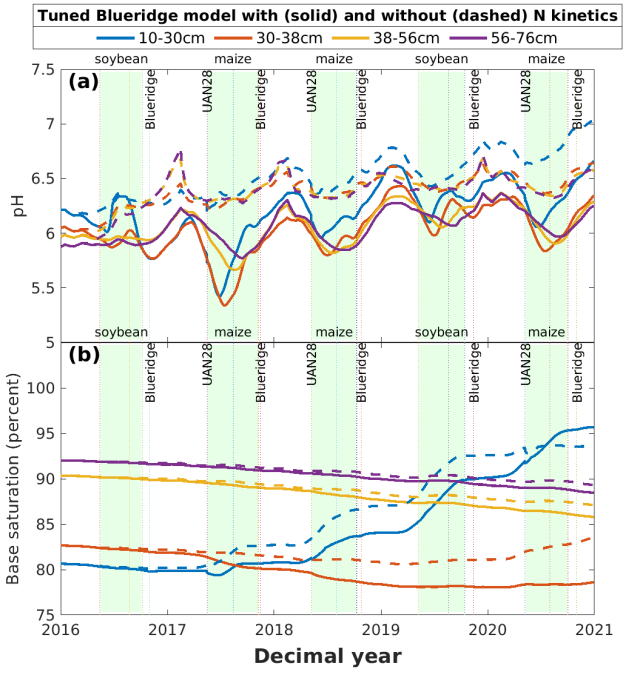

Figure 10. Effect of nitrogen kinetics on (a) solution pH and (b) base saturation in four soil layers. The calibrated run including nitrification, denitrification and N fixation (solid lines) has lower pH than the run without those N kinetic processes (dashed lines). Base saturation increases more quickly in response to ERW treatment without N kinetics.

Note that cation release is lower and less calcite accumulates in the Wo run under closed system conditions, suggesting that CO_2 availability becomes limiting (Fig. 11b, Fig. 12c). Other feedstocks are less strongly limited by closed system conditions. With unlimited CO_2 gas, wollastonite remains undersaturated (Fig. E1) and consequently dissolves completely each year, largely during the fallow season (Fig. E2). This leads to considerably higher calcite precipitation compared to any other run (Fig. 12) and modest CO_2 consumption (Fig. 13).

4 Conclusions

Given the increasing interest ERW as a CDR technique, the ability of models to provide reliable estimates of CDR is important because it is impractical to follow the carbon in many soils, or examine long-term impacts of rock dust treatments. The geochemical soil model presented here aims to represent all key processes affecting soil chemistry. In addition to the weathering of both applied and native soil minerals, these processes include the kinetics of nutrient uptake by plants, release of nutrients from decomposing organic matter, microbially-mediated nitrogen cycling, fertiliser applications, evapotranspiration, sorption and secondary phase dynamics.

https://doi.org/10.5194/egusphere-2025-5823
Preprint. Discussion started: 27 January 2026

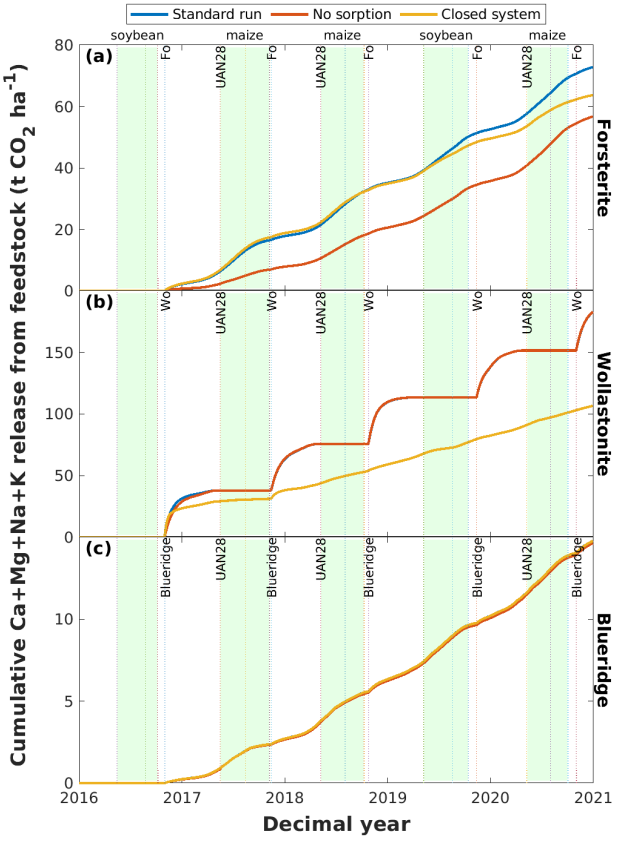

Figure 11. Model total base cation release from three feedstocks tilled into the top 18 cm of soil. Note that the scales on the Y axis for the three panels differ.

Here, we demonstrate several of this model's capabilities using data from Energy Farm ERW field trials (e.g., Beerling et al., 2024) as an example. ARTEMIS was validated against solution chemistry from drainage waters at the Energy Farm. Because the best-matching model soil layer was shallower (56–76 cm) than the physical drain depth (130 cm), one can infer macropore flow at this site.

55-year model runs with differing numbers of feedstock treatments demonstrate the effect of ERW on long-term soil pH and on the lag-times that could be expected as the solutes pass through the soil layers. Results suggest that the Blueridge feedstock would be ineffective at delivering CDR via ion export at application rates that maintain an acceptable rooting-zone pH range for crop growth.

Next, we demonstrate the effect of nitrogen-cycling kinetics (primarily nitrification and denitrification) on solute export by disabling those kinetics in a five-year model run. In comparison to our standard calibrated five-year run, where net nitrification increases nitric acid weathering and nitrate export, the no-N-kinetics run had approximately twice as much bicarbonate export

https://doi.org/10.5194/egusphere-2025-5823
Preprint. Discussion started: 27 January 2026

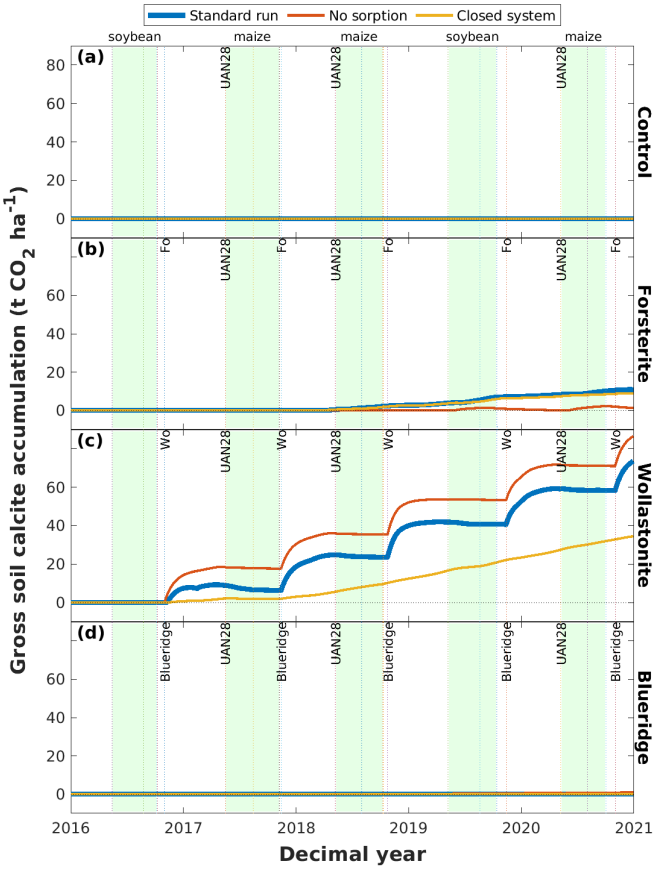

Figure 12. Model soil calcite accumulation between soil surface and the effective drain depth of 76 cm for the CTL (a), Fo (b), Wo (c) and BR (d) feedstock cases.

at the effective drain depth of 76 cm. However, base cation export was considerably lower in the absence of net nitrification, because fewer base cations are required to maintain charge balance of the percolating water when nitrate export is reduced.

Finally, we explored replacement of the slow-weathering Blueridge feedstock with fast-weathering feedstocks, with model options for ignoring sorption and closing the system to rapid CO_2 diffusion. These options were chosen because sorption retains cations in the soil, reducing CDR via exported solutes, and closed-system conditions, which might occur beneath the water table (Cerling, 1991; Engesgaard and Christensen, 1988) could lead to CO_2 limitation. Results suggest that sorption, particularly cation exchange on clays, is a key process for modelling cation release from feedstock as it helps control both the saturation indices of the dissolving phases and the solution pH. However, the Wo (pure wollastonite) feedstock weathers very quickly so that soil processes including sorption only had a transient effect on cation release. Calcium release from Wo results in substantial calcite precipitation, reducing calcium export and therefore CO_2 consumption (HCO_3^- export). This feedstock

https://doi.org/10.5194/egusphere-2025-5823
Preprint. Discussion started: 27 January 2026

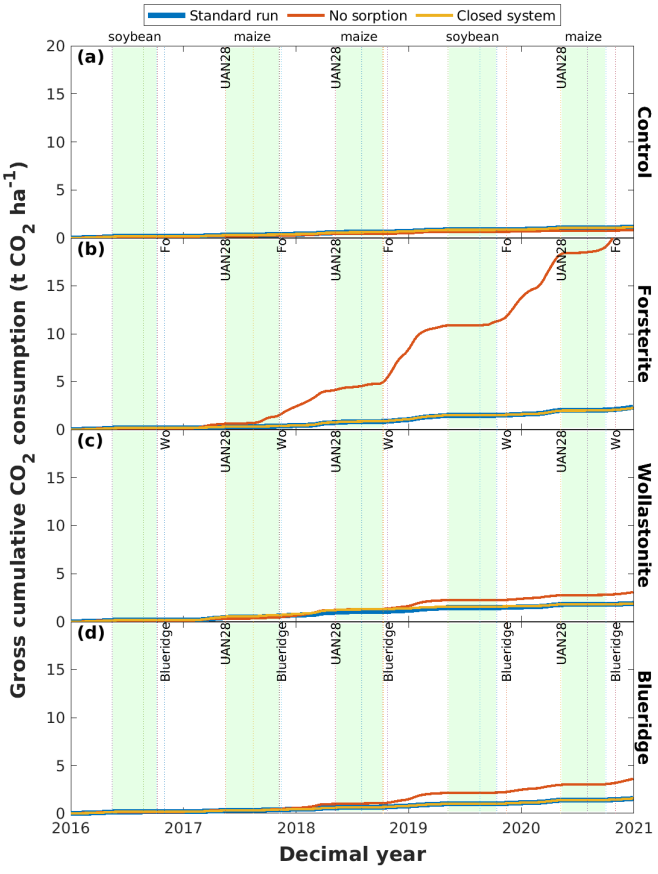

Figure 13. Model cumulative CO_2 consumption (CDR via HCO_3^-+CO_3^{2-} export) calculated at the effective drain depth of 76 cm over the whole five-year period 2016–2020 inclusive for the CTL (a), Fo (b), Wo (c) and BR (d) feedstock cases.

also exhibited sensitivity to CO_2 availability, weathering more slowly under closed-system conditions than under (standard) open-system conditions.

We hope that the code and practical documentation for this model, along with the technical process description in this paper, will prove useful or instructive to the ERW and soil-based CDR community of researchers.

Code and data availability. The ARTEMIS code with the example input data files, example outputs and a user guide are available on zenodo (Taylor, 2025). Data files are in the file ARTEMIS_GMD_code_v1.0_Sep-2025.tar.gz along with the code.

https://doi.org/10.5194/egusphere-2025-5823
Preprint. Discussion started: 27 January 2026

55 Blueridge treatments					
	99% base	10 tCO_2 ha^{-1}		30 tCO_2 ha^{-1}	
	saturation	Cation export	HCO_3^- export	Cation export	HCO_3^- export
Layer	years	years	years	years	years
0–10 cm	2.6	8.4	12.3	18.0	25.7
10–30 cm	4.8	7.4	11.2	13.1	18.8
30–38 cm	9.0	10.7	14.0	17.1	22.9
38–56 cm	14.9	15.3	17.9	22.7	27.9
56–76 cm	20.4	19.1	21.1	27.0	32.3
76–124 cm	N/A	21.4	26.2	31.8	38.9
124–147 cm	N/A	22.8	N/D	N/D	N/D
147–183 cm	N/A	24.2	N/D	N/D	N/D
23 Blueridge treatments					
	99% base	10 tCO_2 ha^{-1}		30 tCO_2 ha^{-1}	
	saturation	Cation export	HCO_3^- export	Cation export	HCO_3^- export
Layer	years	years	years	years	years
0–10 cm	2.6	15.0	23.9	N/D	N/D
10–30 cm	4.8	12.0	17.5	N/D	N/D
30–38 cm	10.7	19.4	24.4	N/D	N/D
38–56 cm	38.8	31.9	35.1	N/D	N/D
56–76 cm	N/D	43.0	41.3	N/D	N/D
76–124 cm	N/A	48.4	46.5	N/D	N/D
124–147 cm	N/A	49.1	N/D	N/D	N/D
147–183 cm	N/A	N/D	N/D	N/D	N/D
4 Blueridge treatments					
	99% base	10 tCO_2 ha^{-1}		**30 tCO_2 ha^{-1}**	
	saturation	Cation export	HCO_3^- export	Cation export	HCO_3^- export
Layer	years	years	years	years	years
0–10 cm	2.6	N/D	N/D	N/D	N/D
10–30 cm	N/D	N/D	N/D	N/D	N/D
30–38 cm	N/D	N/D	N/D	N/D	N/D
38–56 cm	N/D	N/D	N/D	N/D	N/D
56–76 cm	N/D	N/D	N/D	N/D	N/D
76–124 cm	N/A	N/D	N/D	N/D	N/D
124–147 cm	N/A	N/D	N/D	N/D	N/D
147–183 cm	N/A	N/D	N/D	N/D	N/D

N/A: not applicable for layers already at 100% base saturation. N/D: not determined

Table 8. Lag times for achieving 99% base saturation since the first feedstock application, and for CDR via solute export from the bottom of each layer as compared to Ca+Mg release from the feedstock (Figs. 7 and 8). "HCO_3^- export" listed here includes small contributions from the carbonate ion (CO_3^{2-}).

https://doi.org/10.5194/egusphere-2025-5823
Preprint. Discussion started: 27 January 2026

Appendix A: Validation: drain statistics and comparison with lysimeter and topsoil pH data

The model layer that best matched the observed drain water chemistry was determined using the RMSE (Section 2.11.3 for Ca^{2+}, Mg^{2+} and nitrate, along with pH. However, statistics were also generated for the other major ions Na^{+}, K^{+}, Cl^{-}, and S (sulphate), as well as Si. All these statistics are presented in Table A1 for layers 5, 6 and 7 (Fig. 3). Note that Cl^{-} is particularly badly fit as it was adjusted to achieve charge balance in PHREEQC.

Layer 5	Ca	K	Mg	Na	Si	Cl	N	S	pH
RMSE	0.16821	1.2126	0.18321	0.33185	0.094422	1.2397	0.36423	0.94711	0.73403
n	110	42	110	111	109	108	108	108	20
bias	0.062063	1.2032	0.098371	0.3085	0.089164	-1.204	0.11862	-0.93235	-0.42563
crmsd	0.15634	0.15029	0.15456	0.12227	0.03107	0.29524	0.34438	0.16657	0.59803
rmsd	0.016038	0.1871	0.017468	0.031498	0.009044	0.11929	0.035048	0.091136	0.16413
ccoef	0.11871	-0.030955	0.15117	0.28358	0.7744	-0.42819	0.013364	-0.091437	0.036233
Layer 6	Ca	K	Mg	Na	Si	Cl	N	S	pH
RMSE	0.33454	1.3019	0.37056	0.53782	0.049791	1.2944	0.4607	0.9933	0.6312
n	110	42	110	111	109	108	108	108	20
bias	0.30479	1.2934	0.34228	0.52411	0.043688	-1.2552	0.41343	-0.98142	-0.21309
crmsd	0.13791	0.14814	0.14198	0.12066	0.023885	0.31609	0.20328	0.15319	0.59415
rmsd	0.031898	0.20089	0.035331	0.051048	0.0047691	0.12455	0.044331	0.095581	0.14114
ccoef	-0.2262	-0.0303	-0.2356	0.1736	0.87434	-0.54175	-0.20132	0.20385	0.031816
Layer 7	Ca	K	Mg	Na	Si	Cl	N	S	pH
RMSE	0.66755	1.28	0.70184	0.59573	0.023542	1.3193	0.51868	1.0181	0.69314
n	110	42	110	111	109	108	108	108	20
bias	0.66157	1.2711	0.69484	0.58255	-0.012952	-1.2782	0.47973	-1.0014	0.39116
crmsd	0.089107	0.1504	0.09885	0.12464	0.019658	0.32675	0.19721	0.18401	0.57222
rmsd	0.063648	0.19751	0.066918	0.056545	0.0022549	0.12695	0.04991	0.097969	0.15499
ccoef	-0.18797	-0.44907	-0.29545	0.055258	0.91672	-0.58595	-0.31867	0.18142	0.31383

Table A1. Statistics for the comparison between model layer solution chemistry and observed drainage chemistry. All statistics are computed for logged cation concentrations (e.g., $\log_{10}([Ca^{2+}])$. See Section 2.11.3 for details.

The calibrated model run was compared with soil pH data for the top two soil layers (Fig. A1a). Note, however, that soil pH and solution pH are not identical, and no correction has been applied here. This model limitation will be the subject of further development in future. The model Ca, Mg, and nitrate were also compared to lysimeter data (Fig. A1b, c, d). The model fits these data poorly in the winter of 2018. Note also that all three of these solutes are taken up from the top layer by the plants during the growing season, and then their concentrations recover during the fallow season. This is because the roots are

https://doi.org/10.5194/egusphere-2025-5823
Preprint. Discussion started: 27 January 2026

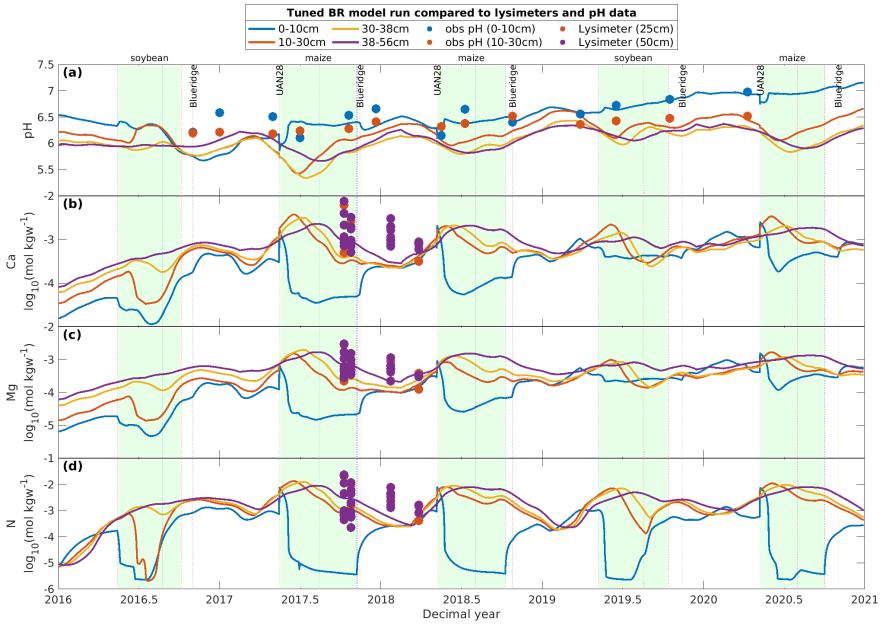

Figure A1. Upper soil chemistry as compared with soil pH and lysimeters. (a) Observed soil pH in the large "B0" treated maize-soy plot compared with model solution pH, without corrections. (b) Calcium ($\log_{10}$(Ca)), (c) magnesium ($\log_{10}$(Mg), and nitrate ($\log_{10}(NO_3)$) in "B0" and small-plot lysimeters (25cm and 50cm respectively).

approximately exponentially distributed (Section 2.6.2). In the subsoil, some uptake occurs, but concentrations tend to stabilise after anthesis when plants are primarily translocating nutrients to grains from other plant parts, and leaves are beginning to senesce.

Appendix B: Nitrogen cycling in example model runs compared to literature

Compared to published model results for maize-soy systems in the Embarras watershed (Table 1 of David et al., 2009) denitrification and nitrate export in the calibrated model run (Fig. B1a,c) are both too high during maize years; nitrate export is also high compared to Blanc-Betes et al. (2021, their Fig. 5). The model has not been calibrated to match the results of these studies, but it would be possible to do so using the parameters shown in Table 5. Reducing the "maxsut" moisture threshold could restrict denitrification rates, for example, but would possibly increase the exported nitrate.

Annual N fixation during soybean years in the calibrated model run is higher than published model results for maize-soy systems in the Embarras watershed (Table 1 of David et al., 2009) but lower than reported N fixation at the Energy Farm (Fig. S9C of Beerling et al., 2024). Total nitrogen uptake in the calibrated run was comparable to literature values for maize years, but is low for soybean years (Fig. B1d). In the case of soybean, N fixation will make up the balance of the N demand when N uptake is insufficient in the model. However, when maize begins grain-filling, 30–60% of N is remobilised from vegetative

https://doi.org/10.5194/egusphere-2025-5823
Preprint. Discussion started: 27 January 2026

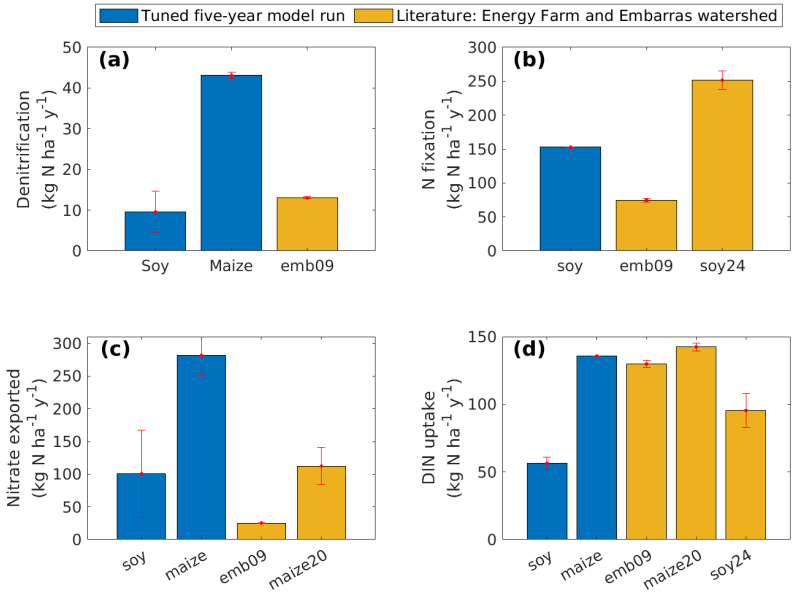

Figure B1. Nitrogen cycling in the calibrated five-year ARTEMIS runs compared to published values for the Energy Farm and the Embarras watershed. Data and results from other studies (David et al., 2009; Blanc-Betes et al., 2021; Beerling et al., 2024) are shown in gold. Error bars represent standard errors. (a) Model denitrification compared to David et al. (2009, their Table 3). (b) Model N fixation during soybean years compared to David et al. (2009, their Table 1) and Beerling et al. (2024, their Fig. S9C). (c) Model nitrate export compared to David et al. (2009, their Table 1) and Blanc-Betes et al. (2021, their Fig. 5). (d) Model nitrogen uptake compared to grain N of David et al. (2009, their Table 1), Blanc-Betes et al. (2021, their Table 1, maize) and Beerling et al. (2024, their Fig. S9D, soybean).

organs to the grain (DeBruin et al., 2017), depending on the hybrid planted, planting density, fertiliser applications etc. No correction for N remobilisation has been applied in ARTEMIS, so the apparent good agreement for maize N uptake could be coincidental.

Appendix C: Soil respiration and CO_2 gas profiles for the Energy Farm

Fig. C1 shows that model pCO_2 in the lower soil layers reaches values above 60000 ppmV during the growing season, following the same pattern as the CLM5 soil respiration. Similarly, the second layer (10–30 cm) approaches 20000 ppmV during the growing season. To model a closed system, the starting moles of CO_2 gas for each day were calculated using $PV = nRT$. These moles may be topped up during the course of the day by carbon release from (kinetically) decaying organic matter, which can be considerable during the fallow season after residues are incorporated into the soil. For feedstocks other than Wo (pure wollastonite), weathering does not fully consume these moles of CO_2 gas in the "closed system" model runs. However, the treatment of gas diffusion in ARTEMIS (Section 2.9) is not rigorous enough for accurate quantification of gas dynamics.

https://doi.org/10.5194/egusphere-2025-5823
Preprint. Discussion started: 27 January 2026

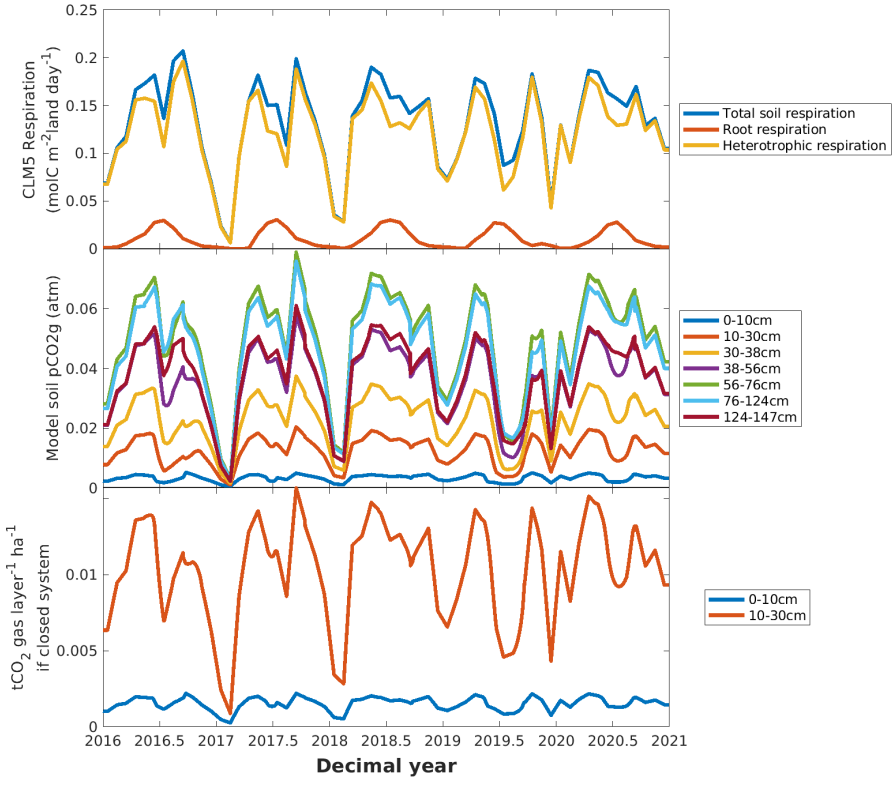

Figure C1. CLM5 soil respiration (a), pCO_2g in model layers (b) and resulting availability of CO_2 in model runs with a closed system (c).

Appendix D: CDR via solute export for several feedstocks

Base cation export from the effective drain depth (76 cm) (Fig. D1) is only slightly higher than bicarbonate+carbonate export (Fig. 13), but shows similar patterns. "No sorption" runs export more cations than other runs for the same feedstock, and that for Fo, exporting only Mg from the feedstock, is particularly high.

Appendix E: Topsoil chemistry and feedstock phase dynamics

Immediately after the first feedstock application, saturation indices (Fig. E1) for forsterite are highest for the no-sorption model option. Increased forsterite SI leads slower weathering rates and to greater forsterite accumulation in the soil with time (Fig. E2). Like forsterite, the Blueridge feedstock has greater long-term feedstock accumulation in the soil and higher SI for its fastest-weathering kinetic phase (ferroactinolite) for the no-sorption model option. This is not the case for wollastonite, which has similar SI for all model options following the first feedstock application in 2016, and complete fallow-season dissolution of applied feedstock each year.

https://doi.org/10.5194/egusphere-2025-5823
Preprint. Discussion started: 27 January 2026

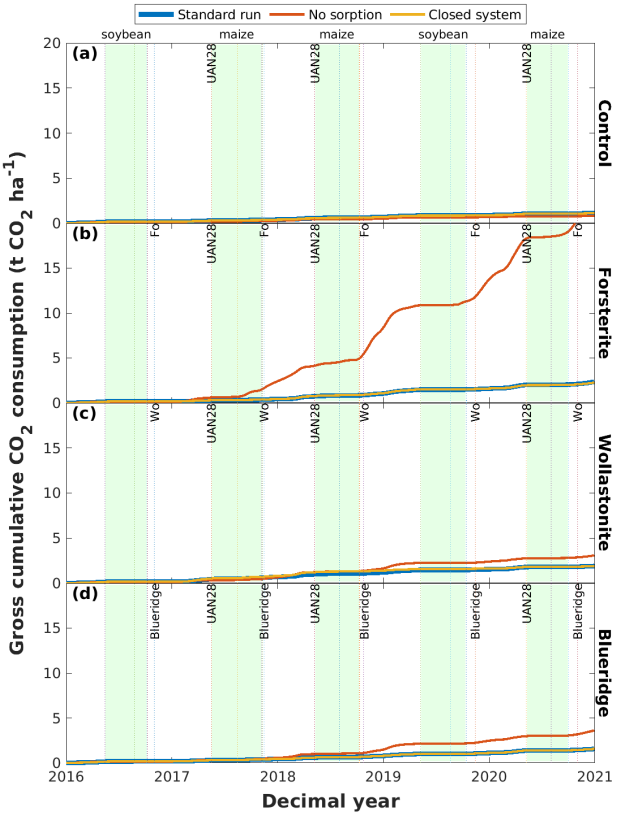

Figure D1. Model total CDR calculated from cation export at the "effective" drain depth 76 cm for three feedstocks.

There are small topsoil pH dips at the beginning of the growing season for all model runs due to UAN fertiliser application, but pH is far more variable for the no-sorption runs for all feedstock cases except wollastonite. For most runs, sorption helps control pH. However, in the case of wollastonite, closed-system conditions lead to unreasonably high pH. In contrast to the other feedstock cases, calcite SI (Fig. E4) is zero for all wollastonite model runs from the first feedstock treatment in autumn 2016. Consequently, calcite precipitation controls topsoil chemistry for Wo runs. For most other runs, calcite is undersaturated; the key exceptions are the Fo runs with sorption. See Section F for details of calcium dynamics in these runs.

Appendix F: Exchanger, surface and calcium dynamics for the standard feedstock model runs

All runs with sorption begin with the same exchange compositions regardless of feedstock. Exchangeable Al was added where the base saturation was under 100%, as in the upper five loess layers (Fig. 3). Initially, calcium is the dominant exchangeable cation in all model runs (Fig. F1), but for the Mg-rich Fo (pure forsterite) feedstock, it is gradually replaced by Mg (Fig. F1b). Displaced calcium temporarily sorbs to other surfaces such as organic matter (Fig. F2), but most of it is subsequently precipitated as calcite in the topsoil (Fig. F3) and subsoil. These dynamics do not occur with the calcium-rich Wo (pure wollastonite)

https://doi.org/10.5194/egusphere-2025-5823
Preprint. Discussion started: 27 January 2026

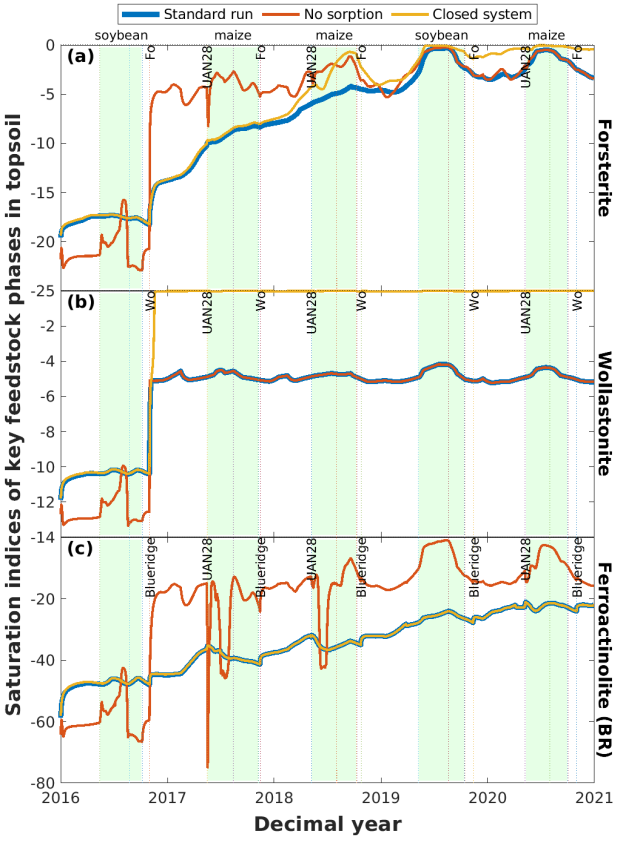

Figure E1. Model saturation indices for key phases in the Fo (a), Wo (b) and BR (c) feedstocks

feedstock, or with the slow-weathering BR (Blueridge) feedstock. Calcite is the only neoformed carbonate mineral that precipitates as a result of treatment. It precipitates largely in the top two layers (Fig. F4).

Author contributions. LLT developed the code, designed and conducted the model experiments, interpreted the results, wrote the documentation, and wrote the manuscript. RHJ provided chemical analyses of lysimeter and drainage waters. IK provided timetable data and upper soil pH. All authors provided comments and edits on the manuscript as well as useful comments and ideas during model development.

Competing interests. DJB has minority equity stakes in two companies aiming to help mitigate climate change (Future Forest and Undo), and is an advisory board member of The Carbon Community, a UK carbon removal charity.

https://doi.org/10.5194/egusphere-2025-5823
Preprint. Discussion started: 27 January 2026

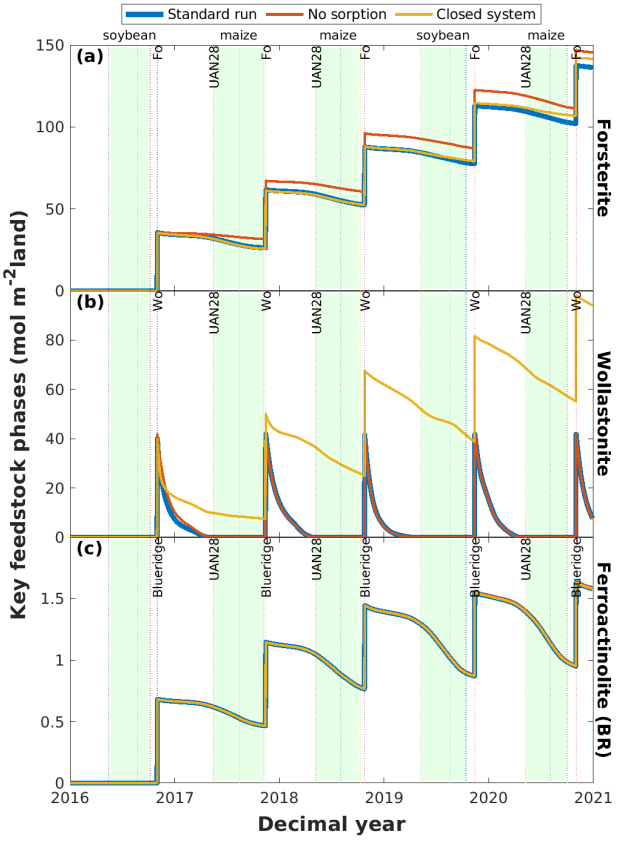

Figure E2. Model dissolution of key phases for three feedstocks (Fo (a), Wo (b) and BR (c)).

Acknowledgements. We would like to thank many past and present members of the Leverhulme Centre for Climate Change Mitigation team for many fruitful discussions during model development for the Energy Farm. Special thanks are due to Peter Wade, whose knowledge of PHREEQC was invaluable when LLT began to develop ARTEMIS, and Grace Andrews and Christina Larkin. Amongst many other contributions to the Energy Farm experiment, they processed and analysed the lysimeter and drainage water samples in RHJ's lab at the University of Southampton. We are grateful to the late Steven Banwart, who gave advice related to influent chemistry, and many other colleagues at the Energy Farm, including Mike Masters, Caitlin Moore, Bethany Blakely, Carl Baldocci, and Evan DeLucia. These colleagues were always ready to answer questions, and their advice and suggestions were much appreciated. Many of them also provided Energy Farm flux tower or geochemical data which does not appear in the simple example study presented here. Finally, we thank the Leverhulme Trust (Leverhulme Research Centre grant number RC-2015-029 to DJB) for funding both this study and the Energy Farm enhanced weathering experiments.

https://doi.org/10.5194/egusphere-2025-5823
Preprint. Discussion started: 27 January 2026

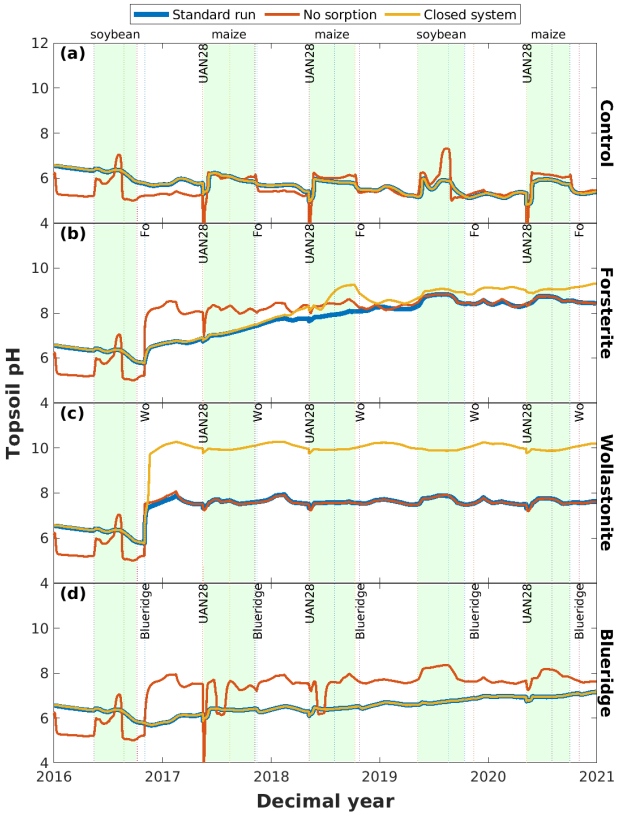

Figure E3. Model topsoil pH for feedstock cases CTL (a), Fo (b), Wo (c) and BR (d). Sorption exerts the key control on pH for all feedstocks except wollastonite (c), which is controlled by calcite precipitation and CO_2 availability.

https://doi.org/10.5194/egusphere-2025-5823
Preprint. Discussion started: 27 January 2026

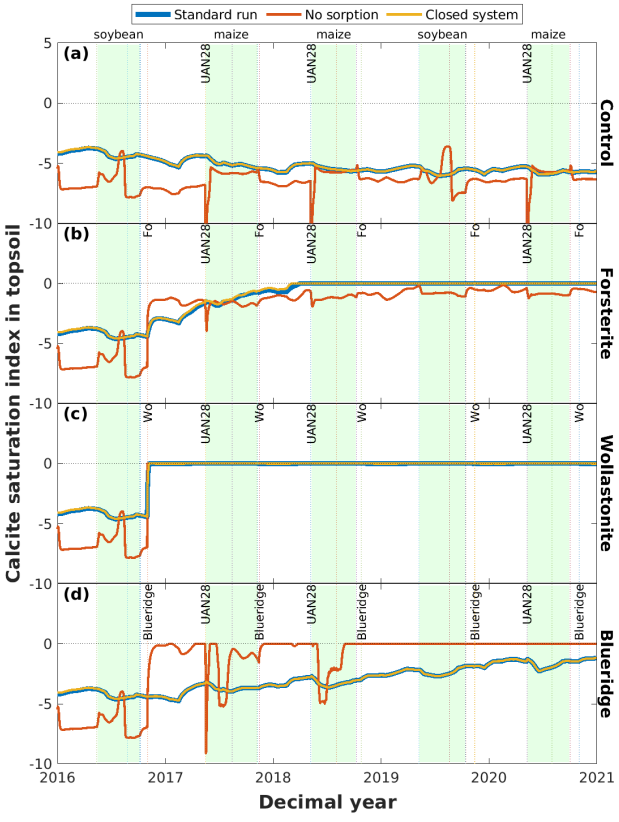

Figure E4. Model topsoil saturation indices for calcite in the CTL (a), Fo (b), Wo (c) and BR (d) feedstock cases

https://doi.org/10.5194/egusphere-2025-5823
Preprint. Discussion started: 27 January 2026

Depth						Sites for sorption				
Top	Bottom	Density[a]	Soil[b]	SOM[c]	CEC[d]	Total	CEC	SOC+Fe[e]	CEC	SOC+Fe
cm		g cm^{-3}	kg	mass%	cmolc/kg	eq layer^{-1}			%	
0	10	1.20	120	4.0	20.3	25.41	23.12	2.29	90.98	9.02
10	30	1.20	240	3.5	22	54.64	50.62	4.01	92.65	7.35
30	38	1.30	104	2.1	23.1	24.51	23.46	1.05	95.72	4.28
38	56	1.33	239	1.1	26	62.74	61.47	1.27	97.97	2.03
56	76	1.35	270	0.9	22.7	61.84	60.66	1.18	98.09	1.91
76	124	1.575	756	0.4	16.8	127.74	126.22	1.51	98.82	1.18
124	147	1.725	397	0.025	15.5	61.56	61.47	0.09	99.86	0.14
147	183	1.725	621	0.025	15.5	96.35	96.22	0.14	99.86	0.14

[a] Bulk density from Beerling et al. (2024)

[b] Soil mass calculated from layer thickness and bulk density

[c] Soil organic matter for Flanagan soil from Soil Survey Staff (2025). Soil organic carbon was calculated assuming 58% carbon (Neitsch et al., 2011). See Section 2.1 for specific site densities. [d] Cation exchange capacity for Flanagan soil at pH 7 from Soil Survey Staff (2025)

[e] Sum of all SURFACE sites. Active fraction for Fe oxide sites set to 0.01 to avoid convergence errors. See Section 2.1 for additional details.

Table F1. Layer sorption data

https://doi.org/10.5194/egusphere-2025-5823
Preprint. Discussion started: 27 January 2026

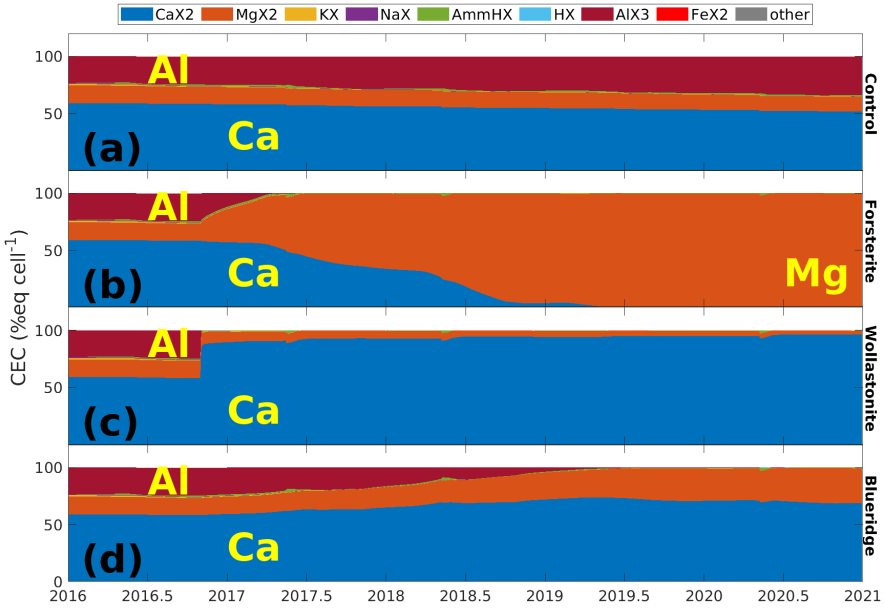

Figure F1. Evolution of the exchange complex in the topsoil ($0-10$ cm) in the standard runs for the four feedstock cases. The exchange complex was initialised using measured CEC and exchangeable base cations (Table F1), with sufficient exchangeable Al added to make 100% of the CEC. The exchange complex contains 91% of the total sorption sites in the topsoil. Ca is the dominant exchangeable cation. (a) CTL (control run with no feedstock) has relatively constant exchangeable Ca, Mg and Al. (b) Fo (run with pure forsterite) first gains Mg at the expense of Al and then at the expense of Ca. (c) Wo (run with pure wollastonite) rapidly gains Ca at the expense of Al and Mg. (d) BR (run with "Blueridge" metabasalt) gradually gains Ca and some Mg at the expense of Al.

https://doi.org/10.5194/egusphere-2025-5823
Preprint. Discussion started: 27 January 2026

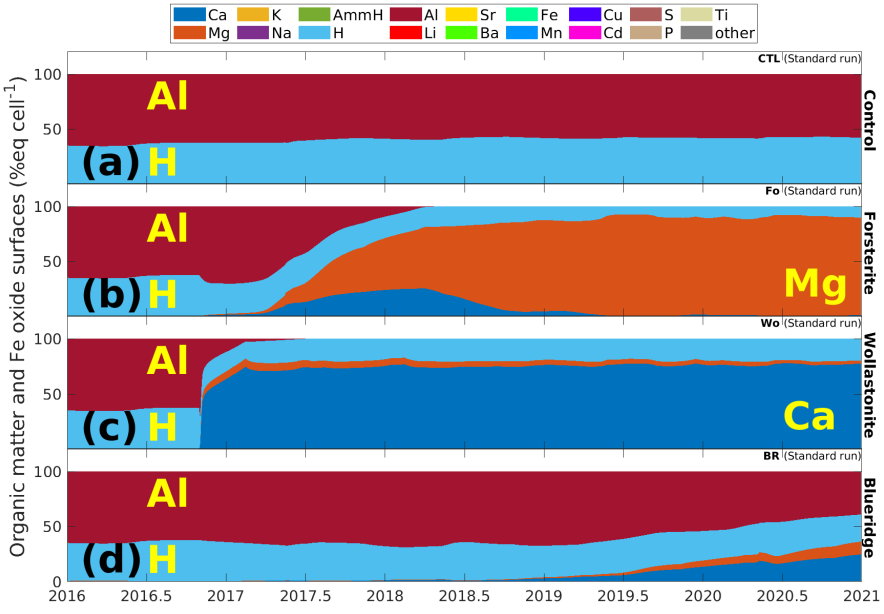

Figure F2. Evolution of the organic and Fe-oxide surfaces in the topsoil ($0-10$ cm) in the standard runs for the four feedstock cases. These surfaces were initialised by equilibration with the solutions and exchange complexes in each layer. In the topsoil, they subtend 9% of the total sorption sites (Table F1). (a) CTL (control run with no feedstock) has relatively constant Al and proton pools. (b) Fo (run with pure forsterite) gains Mg at the expense of Al, after a transient loading with Ca following its displacement by Mg on the exchange complex. (c) Wo (run with pure wollastonite) rapidly gains Ca and a small amount of Mg at the expense of Al. (d) BR (run with "Blueridge" metabasalt) gradually gains Ca and some Mg at the expense of Al after Al has been removed from the exchange complex (Fig F1d).

https://doi.org/10.5194/egusphere-2025-5823
Preprint. Discussion started: 27 January 2026

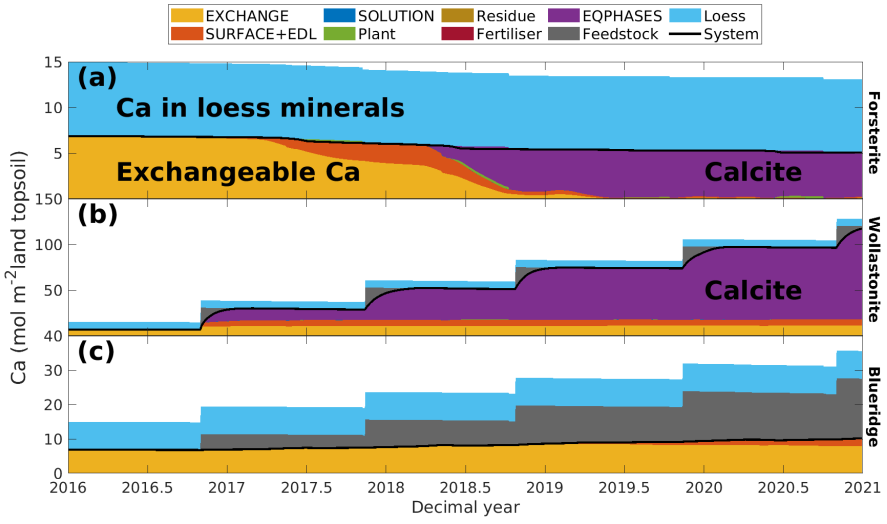

Figure F3. (0 – 10 cm) for the (a) Mg-rich Fo (pure forsterite), (b) Ca-rich Wo (pure wollastonite) and (c) BR (Blueridge) feedstocks. (a) Following displacement of exchangeable Ca by Mg from the Fo feedstock (Fig. F1b), Ca first sorbs to organic matter and hydrous ferric oxides (SURFACE including electric double layer, orange). Subsequently, Mg also displaces Ca on those surfaces and calcite precipitates. (b) For the Wo feedstock, calcite begins to accumulate quickly because Ca is the dominant exchangeable cation and weathering rates are very fast. The amount of Ca taken up by the plant is small compared to the exchangeable, surface and calcite pools. (c) Unweathered metabasalt becomes the largest Ca pool within five years, with only minor increases in Ca on the exchange complex (clays) and more strongly sorbing surfaces (organic matter and Fe oxides). PHREEQC's "System" curve (black) includes all solution, sorbed and equilibrium phases, but not kinetic phases.

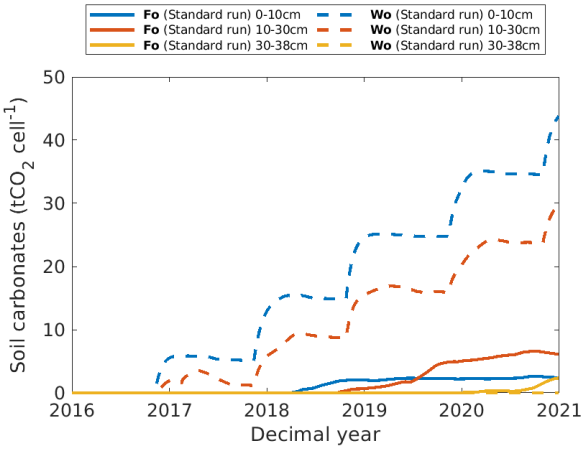

Figure F4. Neoformed soil carbonates resulting from feedstock treatments. Calcite is the only carbonate precipitated, although nesquehonite is defined as a possible secondary phase. For the pure forsterite treatment (Fo, solid lines), there is a small amount of precipitation in the third layer as well as the top two layers. The pure wollastonite treatment (Wo, dashed lines) only precipitates in the top two layers.

https://doi.org/10.5194/egusphere-2025-5823
Preprint. Discussion started: 27 January 2026

References

Alexander, J. D., Fehrenbacher, J. B., and Hallbick, D.: Soil Survey, Champaign-Urbana Area, Illinois: Report 100, Tech. rep., University of Illinois at Urbana-Champaign Agricultural Experiment Station, https://ia601608.us.archive.org/28/items/champaign_urbanaIL1974/champaign_urbanaIL1974.pdf, 1974.

Almaraz, M.: Enhanced weathering may benefit from co-application with organic amendments, AGU Advances, 6, e2025AV001 693, https://doi.org/10.1029/2025AV001693, 2025.

Anderson, S. P.: Glaciers show direct linkage between erosion rate and chemical weathering fluxes, Geomorphology, 67, 147–157, https://doi.org/https://doi.org/10.1016/j.geomorph.2004.07.010, 2005.

Anthony, T. L., Jones, A. R., and Silver, W. L.: Supplementing enhanced weathering with organic amendments accelerates the net climate benefit of soil amendments in rangeland soils, Agu Advances, 6, e2024AV001 480, https://doi.org/10.1029/2024AV001480, 2025.

Arnold, G.: Soil acidification as caused by the nitrogen uptake pattern of Scots pine (*Pinus sylvestris*), Plant and Soil, 142, 41–51, https://doi.org/10.1007/BF00010173, 1992.

Arnold, J. G., Kiniry, J. R., Williams, J. R., Haney, E. B., and Neitsch, S. L.: Soil and Water Assessment Tool input/output file documentation version 2009, Tech. rep., Texas Water Resources Institute, 2011.

Attiwill, P.: The loss of elements from decomposing litter, Ecology, 49, 142–145, https://doi.org/10.2307/1933568, 1968.

Bao, L., Ma, J., Long, W., He, P., Zhang, T.-a., and Nguyen, A. V.: Fractal analysis in particle dissolution: a review, Reviews in Chemical Engineering, 30, 261–287, https://doi.org/https://doi.org/10.1515/revce-2013-0032, 2014.

Barré, P., Fernandez-Ugalde, O., Virto, I., Velde, B., and Chenu, C.: Impact of phyllosilicate mineralogy on organic carbon stabilization in soils: incomplete knowledge and exciting prospects, Geoderma, 235, 382–395, https://doi.org/10.1016/j.geoderma.2014.07.029, 2014.

Bayat, H., Rastgou, M., Nemes, A., Mansourizadeh, M., and Zamani, P.: Mathematical models for soil particle-size distribution and their overall and fraction-wise fitting to measurements, European Journal of Soil Science, 68, 345–364, https://doi.org/https://doi.org/10.1111/ejss.12423, 2017.

Beerling, D. J., Leake, J. R., Long, S. P., Scholes, J. D., Ton, J., Nelson, P. N., Bird, M., Kantzas, E., Taylor, L. L., Sarkar, B., et al.: Farming with crops and rocks to address global climate, food and soil security, Nature plants, 4, 138–147, https://doi.org/10.1038/s41477-018-0108-y, 2018.

Beerling, D. J., Kantzas, E., Lomas, M. R., Wade, P., Eufrasio, R. M., Renforth, P., Sarkar, B., Andrews, M. G., James, R. H., Pearce, C. R., et al.: Potential for large-scale CO_2 removal via enhanced rock weathering with croplands, Nature, 583, 242–248, https://doi.org/https://doi.org/10.1038/s41586-020-2448-9, 2020.

Beerling, D. J., Epihov, D. Z., Kantola, I. B., Masters, M. D., Reershemius, T., Planavsky, N. J., Reinhard, C. T., Jordan, J. S., Thorne, S. J., Weber, J., et al.: Enhanced weathering in the US Corn Belt delivers carbon removal with agronomic benefits, Proceedings of the National Academy of Sciences, 121, e2319436 121, https://doi.org/10.1073/pnas.2319436121, 2024.

Beerling, D. J., Kantzas, E. P., Lomas, M. R., Taylor, L. L., Zhang, S., Kanzaki, Y., Eufrasio, R. M., Renforth, P., Mecure, J.-F., Pollitt, H., et al.: Transforming US agriculture for carbon removal with enhanced weathering, Nature, pp. 1–10, https://doi.org/10.1038/s41586-024-08429-2, 2025.

Benson, L.: A tabulation and evaluation of ion exchange data on smectites, Environmental Geology, 4, 23–29, https://doi.org/10.1007/BF02380496, 1982.

https://doi.org/10.5194/egusphere-2025-5823
Preprint. Discussion started: 27 January 2026

Berner, R. A., Lasaga, A. C., and Garrels, R. M.: Carbonate-silicate geochemical cycle and its effect on atmospheric carbon dioxide over the past 100 million years, American Journal of Science, 283, https://doi.org/10.2475/ajs.283.7.641, 1983.

Bittelli, M., Campbell, G. S., and Flury, M.: Characterization of particle-size distribution in soils with a fragmentation model, Soil Science Society of America Journal, 63, 782–788, https://doi.org/https://doi.org/10.2136/sssaj1999.634782x, 1999.

Blanc-Betes, E., Kantola, I. B., Gomez-Casanovas, N., Hartman, M. D., Parton, W. J., Lewis, A. L., Beerling, D. J., and DeLucia, E. H.: In silico assessment of the potential of basalt amendments to reduce N2O emissions from bioenergy crops, GCB Bioenergy, 13, 224–241, https://doi.org/10.1111/gcbb.12757, 2021.

Bolan, N., Hedley, M., and White, R.: Processes of soil acidification during nitrogen cycling with emphasis on legume based pastures, Plant and soil, 134, 53–63, https://doi.org/https://doi.org/10.1007/BF00010717, 1991.

Brantley, S. L. and Mellott, N. P.: Surface area and porosity of primary silicate minerals, American Mineralogist, 85, 1767–1783, https://doi.org/10.2138/am-2000-11-1220, 2000.

Brantley, S. L., Goldhaber, M. B., and Ragnarsdottir, K. V.: Crossing disciplines and scales to understand the critical zone, Elements, 3, 307–314, https://doi.org/https://doi.org/10.2113/gselements.3.5.307, 2007.

Broadley, M., Brown, P., Cakmak, I., Ma, J. F., Rengel, Z., and Zhao, F.: Beneficial elements, in: Marschner's Mineral Nutrition of Higher Plants, edited by Marschner, P., chap. 8, pp. 249–269, Elsevier Ltd, London, 3 edn., 2012.

Brown, W. K. and Wohletz, K. H.: Derivation of the Weibull distribution based on physical principles and its connection to the Rosin–Rammler and lognormal distributions, Journal of Applied Physics, 78, 2758–2763, https://doi.org/https://doi.org/10.1063/1.360073, 1995.

Brunauer, S., Emmett, P. H., and Teller, E.: Adsorption of gases in multimolecular layers, Journal of the American chemical society, 60, 309–319, 1938.

Cerling, T. E.: Carbon dioxide in the atmosphere: evidence from Cenozoic and Mesozoic paleosols, American Journal of Science;(United States), 291, https://doi.org/10.2475/ajs.291.4.377, 1991.

Chen, M., Gong, L., Schott, J., Lu, P., Chen, K., Yuan, H., Sun, J., Chen, S. A., Apps, J., and Zhu, C.: Coupled feldspar dissolution and secondary mineral precipitation in batch systems: 6. Labradorite dissolution, calcite growth, and clay precipitation at 60°C and pH 8.2–8.4, Geochimica et Cosmochimica Acta, https://doi.org/10.1016/j.gca.2024.11.030, 2024.

Chiaravalloti, I., Theunissen, N., Zhang, S., Wang, J., Sun, F., Ahmed, A. A., Pihlap, E., Reinhard, C. T., and Planavsky, N. J.: Mitigation of soil nitrous oxide emissions during maize production with basalt amendments, Frontiers in Climate, 5, 1203 043, https://doi.org/10.3389/fclim.2023.1203043, 2023.

Choudhury, B. J.: Modeling radiation-and carbon-use efficiencies of maize, sorghum, and rice, Agricultural and Forest Meteorology, 106, 317–330, https://doi.org/S0168-1923(00)00217-3, 2001.

Cosby, B., Hornberger, G., Clapp, R., and Ginn, T.: A statistical exploration of the relationships of soil moisture characteristics to the physical properties of soils, Water Resources Research, 20, 682–690, https://doi.org/10.1029/WR020i006p00682, 1984.

Cubillas, P., Köhler, S., Prieto, M., Causserand, C., and Oelkers, E. H.: How do mineral coatings affect dissolution rates? An experimental study of coupled CaCO3 dissolution—CdCO3 precipitation, Geochimica et Cosmochimica Acta, 69, 5459–5476, https://doi.org/10.1016/j.gca.2005.07.016, 2005.

Daval, D., Sissmann, O., Corvisier, J., Garcia, B., Martinez, I., Guyot, F., and Hellmann, R.: The effect of silica coatings on the weathering rates of wollastonite (CaSiO3) and forsterite (Mg2SiO4): an apparent paradox, in: Water Rock Interaction-WRI-13 Proc. 13th International Conference on Water Rock Interaction, pp. 713–717, https://www.academia.edu/download/83917429/The_effect_of_silica_coatings_on_the_wea20220411-1792-1ka87qi.pdf, 2010.

https://doi.org/10.5194/egusphere-2025-5823
Preprint. Discussion started: 27 January 2026

David, M. B., Del Grosso, S. J., Hu, X., Marshall, E. P., McIsaac, G. F., Parton, W. J., Tonitto, C., and Youssef, M. A.: Modeling denitrification in a tile-drained, corn and soybean agroecosystem of Illinois, USA, Biogeochemistry, 93, 7–30, https://doi.org/10.1007/s10533-008-9273-9, 2009.

de Oliveira Garcia, W., Amann, T., Hartmann, J., Karstens, K., Popp, A., Boysen, L. R., Smith, P., and Goll, D.: Impacts of enhanced weathering on biomass production for negative emission technologies and soil hydrology, Biogeosciences, 17, 2107–2133, https://doi.org/10.5194/bg-17-2107-2020, 2020.

De Vries, W. and Breeuwsma, A.: The relation between soil acidification and element cycling, Water, Air, and Soil Pollution, 35, 293–310, https://doi.org/10.1007/BF00290937, 1987.

DeBruin, J. L., Schussler, J. R., Mo, H., and Cooper, M.: Grain yield and nitrogen accumulation in maize hybrids released during 1934 to 2013 in the US Midwest, Crop Science, 57, 1431–1446, https://doi.org/10.2135/cropsci2016.08.0704, 2017.

Deng, H., Sonnenthal, E., Arora, B., Breunig, H., Brodie, E., Kleber, M., Spycher, N., and Nico, P.: The environmental controls on efficiency of enhanced rock weathering in soils, Scientific Reports, 13, 9765, https://doi.org/10.1038/s41598-023-36113-4, 2023.

Domokos, G., Kun, F., Sipos, A. A., and Szabó, T.: Universality of fragment shapes, Scientific Reports, 5, 9147, https://doi.org/https://doi.org/10.1038/srep09147, 2015.

Dufrene, E., Ochs, R., and Saugier, B.: Photosynthèse et production du palmier à huile en relation avec les facteurs climatiques, Oléagineux, 45, 8–9, 1990.

Dzombak, D. A. and Morel, F. M.: Surface complexation modeling: hydrous ferric oxide, John Wiley & Sons, 1990.

Endres, T., Werner, S., Ennis, J., and Voss, E.: Soil survey of Champaign County, Tech. rep., US Department of Agriculture-Natural Resources Conservation Service and Illinois Agricultural Experiment Station, USDA, Washington, DC, 2001.

Engesgaard, P. and Christensen, T. H.: A review of chemical solute transport models, Hydrology Research, 19, 183–216, https://doi.org/10.2166/nh.1988.0013, 1988.

Epihov, D. Z., Banwart, S. A., McGrath, S. P., Martin, D. P., Steeley, I. L., Cobbold, V., Kantola, I. B., Masters, M. D., DeLucia, E. H., and Beerling, D. J.: Iron Chelation in Soil: Scalable Biotechnology for Accelerating Carbon Dioxide Removal by Enhanced Rock Weathering, Environmental Science & Technology, 58, 11 970–11 987, https://doi.org/10.1021/acs.est.3c10146, 2024.

Erlandsson, M., Oelkers, E., Bishop, K., Sverdrup, H., Belyazid, S., Ledesma, J., and Köhler, S.: Spatial and temporal variations of base cation release from chemical weathering on a hillslope scale, Chemical Geology, 441, 1–13, https://doi.org/10.1016/j.chemgeo.2016.08.008, 2016.

Fageria, N. K., Baligar, V. C., and Jones, C. A.: Growth and mineral nutrition of field crops, CRC press, 2010.

Fakhraei, H. and Driscoll, C. T.: Proton and aluminum binding properties of organic acids in surface waters of the northeastern US, Environmental Science & Technology, 49, 2939–2947, https://doi.org/10.1021/es504024u, 2015.

Farin, D. and Avnir, D.: Reactive fractal surfaces, Journal of Physical Chemistry, 91, 5517–5521, https://doi.org/https://pubs.acs.org/doi/pdf/10.1021/j100306a001, 1987.

Fehrenbacher, J., Alexander, J., Jansen, I., Darmody, R., Pope, R., Flock, M., Voss, E., Scott, J., Andrews, W., and Bushue, L.: Soils of Illinois, Bulletin 778, University of Illinois at Urbana-Champaign College of Agriculture, Agricultural Experiment Station, in cooperation with the Soil Conservation Service, U.S. Department of Agriculture, https://www.ideals.illinois.edu/items/123549/bitstreams/407116/data.pdf, 1984.

Fernández, F. G. and Hoeft, R. G.: Managing soil pH and crop nutrients, Illinois agronomy handbook, 24, 91–112, 2009.

https://doi.org/10.5194/egusphere-2025-5823
Preprint. Discussion started: 27 January 2026

Fishkis, O., Ingwersen, J., and Streck, T.: Phytolith transport in sandy sediment: experiments and modeling, Geoderma, 151, 168–178, https://doi.org/10.1016/j.geoderma.2009.04.003, 2009.

Fishkis, O., Ingwersen, J., Lamers, M., Denysenko, D., and Streck, T.: Phytolith transport in soil: a field study using fluorescent labelling, Geoderma, 157, 27–36, https://doi.org/10.1016/j.geoderma.2010.03.012, 2010.

Fletcher, P. and Sposito, G.: The chemical modelling of clay/electrolyte interactions for montmorillonite, Clay Minerals, 24, 375–391, https://doi.org/10.1180/claymin.1989.024.2.14, 1989.

Frye, J. C., Glass, H. D., and Willman, H. B.: Stratigraphy and mineralogy of the Wisconsinan loesses of Illinois, Circular 334, Illinois State Geological Survey, Prairie Research Institute., 1962.

Fu, S., Cheng, W., and Susfalk, R.: Rhizosphere respiration varies with plant species and phenology: a greenhouse pot experiment, Plant and Soil, 239, 133–140, https://doi.org/10.1023/A:1014959701396, 2002.

Gaillardet, J., Dupré, B., Louvat, P., and Allegre, C.: Global silicate weathering and CO_2 consumption rates deduced from the chemistry of large rivers, Chemical geology, 159, 3–30, https://doi.org/10.1016/S0009-2541(99)00031-5, 1999.

Gaucher, Y., Tanaka, K., Johansson, D. J., Goll, D. S., and Ciais, P.: Leveraging ecosystems responses to enhanced rock weathering in mitigation scenarios, Nature Communications, 16, 3021, https://doi.org/10.1038/s41467-025-58284-6, 2025.

Giménez, D., Allmaras, R., Huggins, D., and Nater, E.: Mass, surface, and fragmentation fractal dimensions of soil fragments produced by tillage, Geoderma, 86, 261–278, https://doi.org/https://doi.org/10.1016/S0016-7061(98)00043-3, 1998.

Goldich, S. S.: A study in rock-weathering, The Journal of Geology, 46, 17–58, https://doi.org/10.1086/624619, 1938.

Green, W. H. and Ampt, G. A.: Studies on Soil Phyics, The Journal of Agricultural Science, 4, 1–24, https://doi.org/10.1017/S0021859600001441, 1911.

Hangx, S. J. and Spiers, C. J.: Coastal spreading of olivine to control atmospheric CO2 concentrations: A critical analysis of viability, International Journal of Greenhouse Gas Control, 3, 757–767, https://doi.org/10.1016/j.ijggc.2009.07.001, 2009.

Hartmann, W. K.: Terrestrial, lunar, and interplanetary rock fragmentation, Icarus, 10, 201–213, https://doi.org/https://doi.org/10.1016/0019-1035(69)90022-0, 1969.

Hasemer, H., Borevitz, J., and Buss, W.: Measuring enhanced weathering: inorganic carbon-based approaches may be required to complement cation-based approaches, Frontiers in Climate, 6, 1352 825, https://doi.org/10.3389/fclim.2024.1352825, 2024.

Hawkesford, M., Horst, W., Kichey, T., Lambers, H., Schjoerring, J., Møller, I. S., and White, P.: Functions of macronutrients, in: Marschner's Mineral Nutrition of Higher Plants, edited by Marschner, P., chap. 6, pp. 135–189, Elsevier Ltd, London, 3 edn., 2012.

Haynes, R.: Soil acidification induced by leguminous crops, Grass and Forage Science, 38, 1–11, https://doi.org/10.1111/j.1365-2494.1983.tb01614.x, 1983.

Henry, W.: III. Experiments on the quantity of gases absorbed by water, at different temperatures, and under different pressures, Philosophical Transactions of the Royal Society of London, pp. 29–274, https://doi.org/10.1098/rstl.1803.0004, 1803.

Hoffmann, M. P., Vera, A. C., Van Wijk, M., Giller, K. E., Oberthuer, T., Donough, C., and Whitbread, A. M.: Simulating potential growth and yield of oil palm (*Elaeis guineensis*) with PALMSIM: Model description, evaluation and application, Agricultural Systems, 131, 1–10, https://doi.org/10.1016/j.agsy.2014.07.006, 2014.

Holdren Jr, G. R. and Speyer, P. M.: Reaction rate-surface area relationships during the early stages of weathering. II. Data on eight additional feldspars, Geochimica et Cosmochimica Acta, 51, 2311–2318, https://doi.org/10.1016/0016-7037(87)90284-5, 1987.

https://doi.org/10.5194/egusphere-2025-5823
Preprint. Discussion started: 27 January 2026

Hooghoudt, S.: Bijdragen tot de kennis van eenige natuurkundige grootheden van den grond: Algemeene beschouwing van het probleem van de detailontwatering en de infiltratie door middel van parallel loopende drains, greppels, slooten en kanalen, Tech. Rep. 7, Algemeene Landsdrukkerij, https://edepot.wur.nl/250838, 1940.

Huber, W. C., Dickinson, R. E., Barnwell Jr, T. O., and Branch, A.: Storm water management model; version 4, Environmental Protection Agency, United States, https://www.casqa.org/wp-content/uploads/2023/03/james_2002_swmm4usermanual.pdf, 1988.

Johnson, C.: Cation exchange properties of acid forest soils of the northeastern USA, European Journal of Soil Science, 53, 271–282, https://doi.org/10.1046/j.1365-2389.2002.00441.x, 2002.

Jolliff, J. K., Kindle, J. C., Shulman, I., Penta, B., Friedrichs, M. A., Helber, R., and Arnone, R. A.: Summary diagrams for coupled hydrodynamic-ecosystem model skill assessment, Journal of Marine Systems, 76, 64–82, https://doi.org/10.1016/j.jmarsys.2008.05.014, 2009.

Kantola, I. B., Blanc-Betes, E., Masters, M. D., Chang, E., Marklein, A., Moore, C. E., von Haden, A., Bernacchi, C. J., Wolf, A., Epihov, D. Z., et al.: Improved net carbon budgets in the US Midwest through direct measured impacts of enhanced weathering, Global change biology, 29, 7012–7028, https://doi.org/10.1111/gcb.16903, 2023.

Kantzas, E. P., Val Martin, M., Lomas, M. R., Eufrasio, R. M., Renforth, P., Lewis, A. L., Taylor, L. L., Mecure, J.-F., Pollitt, H., Vercoulen, P. V., et al.: Substantial carbon drawdown potential from enhanced rock weathering in the United Kingdom, Nature Geoscience, 15, 382–389, https://doi.org/10.1038/s41586-024-08429-2, 2022.

Kanzaki, Y., Zhang, S., Planavsky, N. J., and Reinhard, C. T.: Soil Cycles of Elements simulator for Predicting TERrestrial regulation of greenhouse gases: SCEPTER v0. 9, Geoscientific Model Development, 15, 4959–4990, https://doi.org/10.5194/gmd-15-4959-2022, 2022.

Kanzaki, Y., Planavsky, N., Zhang, S., Jordan, J., Suhrhoff, T. J., and Reinhard, C.: Soil cation storage is a key control on the carbon removal dynamics of enhanced weathering, Environmental Research Letters, 20, 074 055, https://doi.org/10.1088/1748-9326/ade0d5, 2025.

Kelland, M. E., Wade, P. W., Lewis, A. L., Taylor, L. L., Sarkar, B., Andrews, M. G., Lomas, M. R., Cotton, T. A., Kemp, S. J., James, R. H., et al.: Increased yield and CO2 sequestration potential with the C4 cereal Sorghum bicolor cultivated in basaltic rock dust-amended agricultural soil, Global Change Biology, 26, 3658–3676, https://doi.org/10.1111/gcb.15089, 2020.

Kirschbaum, M. U. and Mueller, R.: Net Ecosystem Exchange: Workshop Proceedings, Cooperative Research Centre for Greenhouse Accounting, 2001.

Kuypers, M. M., Marchant, H. K., and Kartal, B.: The microbial nitrogen-cycling network, Nature Reviews Microbiology, 16, 263–276, https://doi.org/10.1038/nrmicro.2018.9, 2018.

Lamade, E., Djégui, N., and Leterme, P.: Estimation of carbon allocation to the roots from soil respiration measurements of oil palm, Plant and soil, 181, 329–339, https://doi.org/10.1007/BF00012067, 1996.

Lamb, W. F., Gasser, T., Roman-Cuesta, R. M., Grassi, G., Gidden, M. J., Powis, C. M., Geden, O., Nemet, G., Pratama, Y., Riahi, K., et al.: The carbon dioxide removal gap, Nature Climate Change, 14, 644–651, https://doi.org/10.1038/s41558-024-01984-6, 2024.

Lasaga, A. C.: Chemical kinetics of water-rock interactions, Journal of Geophysical Research: Solid Earth, 89, 4009–4025, https://doi.org/10.1029/JB089iB06p04009, 1984.

Lavallee, J. M., Soong, J. L., and Cotrufo, M. F.: Conceptualizing soil organic matter into particulate and mineral-associated forms to address global change in the 21st century, Global change biology, 26, 261–273, https://doi.org/10.1111/gcb.14859, 2020.

Lawrence, D., Fisher, R., Koven, C., Oleson, K., Swenson, S., and Vertenstein, M.: Technical description of version 5.0 of the Community Land Model (CLM), National Center for Atmospheric Research, PO Box 3000, Boulder, CO 80307-300, 23 March 2020.

https://doi.org/10.5194/egusphere-2025-5823
Preprint. Discussion started: 27 January 2026

Lewis, A. L., Sarkar, B., Wade, P., Kemp, S. J., Hodson, M. E., Taylor, L. L., Yeong, K. L., Davies, K., Nelson, P. N., Bird, M. I., et al.: Effects of mineralogy, chemistry and physical properties of basalts on carbon capture potential and plant-nutrient element release via enhanced weathering, Applied Geochemistry, 132, 105 023, https://doi.org/10.1016/j.apgeochem.2021.105023, 2021.

Liang, F., Li, B., Vogt, R. D., Mulder, J., Song, H., Chen, J., and Guo, J.: Straw return exacerbates soil acidification in major Chinese croplands, Resources, Conservation and Recycling, 198, 107 176, https://doi.org/10.1016/j.resconrec.2023.107176, 2023.

Lofts, S. and Tipping, E.: Solid-solution metal partitioning in the Humber rivers: application of WHAM and SCAMP, Science of the Total Environment, 251, 381–399, https://doi.org/10.1016/S0048-9697(00)00418-6, 2000.

McCammon, R. C. and Deyette, N. A.: The US Geological Survey National Atmospheric Deposition Program, National Trends Network, 2023, Tech. rep., USGS General Information Product, https://doi.org/10.3133/gip258, 2025.

McLay, C., Barton, L., and Tang, C.: Acidification potential of ten grain legume species grown in nutrient solution, Australian Journal of Agricultural Research, 48, 1025–1032, https://doi.org/10.1071/A96174, 1997.

Michaelis, L. and Menten, M. L.: Die kinetic invertinwirkung Biochem, Zeitsch, 49, 1913.

Michaelis, L. and Menten, M. L.: The kinetics of invertin action: Translated by TRC Boyde Submitted 4 February 1913, FEBS letters, 587, 2712–2720, https://febs.onlinelibrary.wiley.com/doi/pdfdirect/10.1016/j.febslet.2013.07.015, 2013.

Miranda, J. G. V., Montero, E., Alves, M. C., González, A. P., and Vázquez, E. V.: Multifractal characterization of saprolite particle-size distributions after topsoil removal, Geoderma, 134, 373–385, https://doi.org/https://doi.org/10.1016/j.geoderma.2006.03.014, 2006.

Monaghan, R., Morrison, J., and Sinclair, A.: Soil acidification through carbon cycling in legumes: a pot experiment examining the contributions from white clover, lotus, caucasian clover, and lucerne, New Zealand Journal of Agricultural Research, 41, 243–250, https://doi.org/10.1080/00288233.1998.9513308, 1998.

Nagy, K. L., Cygan, R. T., Hanchar, J. M., and Sturchio, N. C.: Gibbsite growth kinetics on gibbsite, kaolinite, and muscovite substrates: Atomic force microscopy evidence for epitaxy and an assessment of reactive surface area, Geochimica et Cosmochimica Acta, 63, 2337–2351, https://doi.org/10.1016/S0016-7037(99)00118-0, 1999.

Navarre-Sitchler, A., Steefel, C. I., Sak, P. B., and Brantley, S. L.: A reactive-transport model for weathering rind formation on basalt, Geochimica et Cosmochimica Acta, 75, 7644–7667, https://doi.org/10.1016/j.gca.2011.09.033, 2011.

Navarre-Sitchler, A. K. and Brantley, S. L.: Basalt weathering across scales, Earth and Planetary Science Letters, 261, 321–334, https://doi.org/https://doi.org/10.1016/j.epsl.2007.07.010, 2007.

Navarre-Sitchler, A. K., Cole, D. R., Rother, G., Jin, L., Buss, H. L., and Brantley, S. L.: Porosity and surface area evolution during weathering of two igneous rocks, Geochimica et Cosmochimica Acta, 109, 400–413, https://doi.org/https://doi.org/10.1016/j.gca.2013.02.012, 2013.

Neitsch, S. L., Arnold, J. G., Kiniry, J. R., and Williams, J. R.: Soil and Water Assessment Tool theoretical documentation version 2009, Tech. rep., Texas Water Resources Institute, 2011.

Neumann, G. and Römheld, V.: Rhizosphere chemistry in relation to plant nutrition, in: Marschner's Mineral Nutrition of Higher Plants, edited by Marschner, P., chap. 14, pp. 347–368, Elsevier Ltd, London, 3 edn., 2012.

Niu, G.-Y., Yang, Z.-L., Dickinson, R. E., and Gulden, L. E.: A simple TOPMODEL-based runoff parameterization (SIMTOP) for use in global climate models, Journal of Geophysical Research: Atmospheres, 110, https://doi.org/10.1029/2005JD006111, 2005.

Noilhan, J. and Lacarrère, P.: GCM grid-scale evaporation from mesoscale modeling, Journal of Climate, 8, 206–223, https://doi.org/10.1175/1520-0442(1995)008<0206:GGSEFM>2.0.CO;2, 1995.

Noiriel, C., Steefel, C. I., Yang, L., and Bernard, D.: Effects of pore-scale precipitation on permeability and flow, Advances in water resources, 95, 125–137, https://doi.org/10.1016/j.advwatres.2015.11.013, 2016.

https://doi.org/10.5194/egusphere-2025-5823
Preprint. Discussion started: 27 January 2026

Nugent, M., Brantley, S. L., Pantano, C. G., and Maurice, P.: The influence of natural mineral coatings on feldspar weathering, Nature, 395, 588–591, https://doi.org/10.1038/26951, 1998.

Oelkers, E. H., Benning, L. G., Lutz, S., Mavromatis, V., Pearce, C. R., and Plümper, O.: The efficient long-term inhibition of forsterite dissolution by common soil bacteria and fungi at Earth surface conditions, Geochimica et Cosmochimica Acta, 168, 222–235, https://doi.org/10.1016/j.gca.2015.06.004, 2015.

Oh, N.-H., Kim, H.-S., and Richter Jr, D. D.: What regulates soil CO2 concentrations? A modeling approach to CO_2 diffusion in deep soil profiles, Environmental Engineering Science, 22, 38–45, https://doi.org/10.1089/ees.2005.22.38, 2005.

Palandri, J. L. and Kharaka, Y. K.: A compilation of rate parameters of water-mineral interaction kinetics for application to geochemical modeling, Tech. rep., US Geological Survey, https://doi.org/10.3133/ofr20041068, 2004.

Parkhurst, D. and Appelo, C.: Description of input and examples for PHREEQC version 3—A computer program for speciation, batch-reaction, one-dimensional transport, and inverse geochemical calculations, http://pubs.usgs.gov/tm/06/a43, 2013.

Perfect, E.: Fractal models for the fragmentation of rocks and soils: a review, Engineering Geology, 48, 185–198, https://doi.org/https://doi.org/10.1016/S0013-7952(97)00040-9, 1997.

Raich, J. W. and Schlesinger, W. H.: The global carbon dioxide flux in soil respiration and its relationship to vegetation and climate, Tellus B, 44, 81–99, https://doi.org/10.1034/j.1600-0889.1992.t01-1-00001.x, 1992.

Rallison, R. and Miller, N.: Past, present and future SCS runoff procedure, in: Rainfall runoff relationship—Proceedings of the International Symposium on rainfall-runoff modelling, edited by Singh, V., Water Tesources Publications, Colorado USA, 1981.

Reddy, K., Khaleel, R., Overcash, M., and Westerman, P.: A nonpoint source model for land areas receiving animal wastes: II. Ammonia volatilization, Transactions of the ASAE, 22, 1398–1405, https://doi.org/10.13031/2013.35219, 1979.

Reershemius, T., Kelland, M. E., Jordan, J. S., Davis, I. R., D'Ascanio, R., Kalderon-Asael, B., Asael, D., Suhrhoff, T. J., Epihov, D. Z., Beerling, D. J., et al.: Initial validation of a soil-based mass-balance approach for empirical monitoring of enhanced rock weathering rates, Environmental Science & Technology, 57, 19 497–19 507, https://doi.org/10.1021/acs.est.3c03609, 2023.

Renforth, P. and Henderson, G.: Assessing ocean alkalinity for carbon sequestration, Reviews of Geophysics, 55, 636–674, https://doi.org/10.1002/2016RG000533, 2017.

Richards, L. A.: Capillary conduction of liquids through porous mediums, Physics, 1, 318–333, https://doi.org/10.1063/1.1745010, 1931.

Ritger, P. L. and Peppas, N. A.: A simple equation for description of solute release I. Fickian and non-fickian release from non-swellable devices in the form of slabs, spheres, cylinders or discs, Journal of Controlled Release, 5, 23–36, https://doi.org/10.1016/0168-3659(87)90034-4, 1987.

Rodríguez-Lado, L. and Lado, M.: Relation between soil forming factors and scaling properties of particle size distributions derived from multifractal analysis in topsoils from Galicia (NW Spain), Geoderma, 287, 147–156, https://doi.org/https://doi.org/10.1016/j.geoderma.2016.08.005, 2017.

Rosin, O. and Rammler, E.: Particle mass distribution for coarse crushed coal, Journal of the Institute of Fuel, 7, 29–36, 1933.

Schmidt, M. W., Torn, M. S., Abiven, S., Dittmar, T., Guggenberger, G., Janssens, I. A., Kleber, M., Kögel-Knabner, I., Lehmann, J., Manning, D. A., et al.: Persistence of soil organic matter as an ecosystem property, Nature, 478, 49–56, https://doi.org/10.1038/nature10386, 2011.

Sharp, J. M.: Anomalous pink till, Transactions of the Illinois State Academy of Sciences, 67, 303–311, 1974.

Shi, Z., Allen, H. E., Di Toro, D. M., Lee, S.-Z., Meza, D. M. F., and Lofts, S.: Predicting cadmium adsorption on soils using WHAM VI, Chemosphere, 69, 605–612, https://doi.org/10.1016/j.chemosphere.2007.03.001, 2007.

https://doi.org/10.5194/egusphere-2025-5823
Preprint. Discussion started: 27 January 2026

Shi, Z., Hoffman, F. M., Xu, M., Mishra, U., Allison, S. D., Zhou, J., and Randerson, J. T.: Global-scale convergence obscures inconsistencies in soil carbon change predicted by Earth system models, AGU Advances, 5, e2023AV001 068, https://doi.org/10.1029/2023AV001068, 2024.

Sofyane, A., Lahcini, M., El Meziane, A., Khouloud, M., Dahchour, A., Caillol, S., and Raihane, M.: Properties of coated controlled release diammonium phosphate fertilizers prepared with the use of bio-based amino oil, Journal of the American Oil Chemists' Society, 97, 751–763, https://doi.org/10.1002/aocs.12360, 2020.

Soil Survey Staff: Web Soil Survey, Natural Resources Conservation Service, United Stated Department of Agriculture, http://websoilsurvey.sc.egov.usda.gov/, accessed 1 February 2025, 2025.

Sokol, N. W., Whalen, E. D., Jilling, A., Kallenbach, C., Pett-Ridge, J., and Georgiou, K.: Global distribution, formation and fate of mineral-associated soil organic matter under a changing climate: A trait-based perspective, Functional Ecology, 36, 1411–1429, https://doi.org/10.1111/1365-2435.14040, 2022.

Solomon, D. K. and Cerling, T. E.: The annual carbon dioxide cycle in a montane soil: Observations, modeling, and implications for weathering, Water Resources Research, 23, 2257–2265, https://doi.org/10.1029/WR023i012p02257, 1987.

Stamboliadis, E., Petrakis, E., and Pantelaki, O.: Variation of dimensional properties of particulate materials during grinding and their non-fractal nature, Canadian Metallurgical Quarterly, 50, 119–126, https://doi.org/10.1179/000844311X12949291727970, 2011.

Stefánsson, A. and Arnórsson, S.: Feldspar saturation state in natural waters, Geochimica et Cosmochimica Acta, 64, 2567–2584, https://doi.org/10.1016/S0016-7037(00)00392-6, 2000.

Stefánsson, A., Gíslason, S. R., and Arnórsson, S.: Dissolution of primary minerals in natural waters: II. Mineral saturation state, Chemical Geology, 172, 251–276, https://doi.org/10.1016/S0016-7037(00)00392-6, 2001.

Stoner, S., Trumbore, S. E., González-Pérez, J. A., Schrumpf, M., Sierra, C. A., Hoyt, A. M., Chadwick, O., and Doetterl, S.: Relating mineral–organic matter stabilization mechanisms to carbon quality and age distributions using ramped thermal analysis, Philosophical Transactions of the Royal Society A, 381, 20230 139, https://doi.org/10.1098/rsta.2023.0139, 2023.

Stumm, W. and Morgan, J.: Aquatic chemistry: chemical equilibria and rates in natural waters, Environmental science and technology (USA)., 1996.

Sulman, B. N., Moore, J. A., Abramoff, R., Averill, C., Kivlin, S., Georgiou, K., Sridhar, B., Hartman, M. D., Wang, G., Wieder, W. R., et al.: Multiple models and experiments underscore large uncertainty in soil carbon dynamics, Biogeochemistry, 141, 109–123, https://doi.org/10.1007/s10533-018-0509-z, 2018.

Tang, C., Barton, L., and Raphael, C.: Pasture legume species differ in their capacity to acidify soil, Australian Journal of Agricultural Research, 49, 53–58, https://doi.org/10.1071/A97080, 1998.

Tang, C., Unkovich, M., and Bowden, J.: Factors affecting soil acidification under legumes. III. Acid production by N_2-fixing legumes as influenced by nitrate supply, New Phytologist, 143, 513–521, https://doi.org/10.1046/j.1469-8137.1999.00475.x, 1999.

Taylor, K. E.: Summarizing multiple aspects of model performance in a single diagram, Journal of geophysical research: atmospheres, 106, 7183–7192, https://doi.org/10.1029/2000JD900719, 2001.

Taylor, L.: ARTEMIS reactive transport/enhanced weathering model in soils, https://zenodo.org/doi/10.5281/zenodo.17682252, 2025.

Taylor, L., Driscoll, C., Groffman, P., Rau, G., Blum, J., and Beerling, D.: Increased carbon capture by a silicate-treated forested watershed attenuated by acid deposition, Biogeosciences, 8, 169–188, https://doi.org/10.5194/bg-18-169-2021, 2021.

https://doi.org/10.5194/egusphere-2025-5823
Preprint. Discussion started: 27 January 2026

Tian, H., Lu, C., Yang, J., Banger, K., Huntzinger, D. N., Schwalm, C. R., Michalak, A. M., Cook, R., Ciais, P., Hayes, D., et al.: Global patterns and controls of soil organic carbon dynamics as simulated by multiple terrestrial biosphere models: Current status and future directions, Global Biogeochemical Cycles, 29, 775–792, https://doi.org/10.1002/2014GB005021, 2015.

Tipping, E.: Humic ion-binding model VI: an improved description of the interactions of protons and metal ions with humic substances, Aquatic Geochemistry, 4, 3–47, https://doi.org/10.1023/A:1009627214459, 1998.

Tipping, E. and Hurley, M. A.: A unifying model of cation binding by humic substances, Geochimica et Cosmochimica Acta, 56, 3627–3641, https://doi.org/10.1016/0016-7037(92)90158-F, 1992.

Tolman, R. C.: The principle of microscopic reversibility, Proceedings of the National Academy of Sciences, 11, 436–439, https://doi.org/10.1073/pnas.11.7.436, 1925.

Turcotte, D. L.: Fractals and fragmentation, Journal of Geophysical Research: Solid Earth, 91, 1921–1926, https://doi.org/https://doi.org/10.1029/JB091iB02p01921, 1986.

Val Martin, M., Blanc-Betes, E., Fung, K. M., Kantzas, E. P., Kantola, I. B., Chiaravalloti, I., Taylor, L. L., Emmons, L. K., Wieder, W. R., Planavsky, N. J., et al.: Improving nitrogen cycling in a land surface model (CLM5) to quantify soil N 2 O, NO, and NH 3 emissions from enhanced rock weathering with croplands, Geoscientific Model Development, 16, 5783–5801, https://doi.org/10.5194/gmd-16-5783-2023, 2023.

Van Beusichem, M.: Nutrient absorption by pea plants during dinitrogen fixation. 2. Effects of ambient acidity and temperature., Netherlands Journal of Agricultural Science, 30, 85–97, https://doi.org/10.18174/njas.v30i2.16983, 1982.

Vicca, S., Goll, D. S., Hagens, M., Hartmann, J., Janssens, I. A., Neubeck, A., Peñuelas, J., Poblador, S., Rijnders, J., Sardans, J., et al.: Is the climate change mitigation effect of enhanced silicate weathering governed by biological processes?, Global change biology, 28, 711–726, https://doi.org/10.1111/gcb.15993, 2022.

Vienne, A., Frings, P., Poblador, S., Steinwidder, L., Rijnders, J., Schoelynck, J., Vinduskova, O., and Vicca, S.: Earthworms in an enhanced weathering mesocosm experiment: Effects on soil carbon sequestration, base cation exchange and soil CO2 efflux, Soil Biology and Biochemistry, 199, 109 596, https://doi.org/10.1016/j.soilbio.2024.109596, 2024.

Wickham, J. T.: Glacial geology of north-central and western Champaign County, Illinois, Circular 506, Illinois State Geological Survey, 1979.

Willman, H. B., Glass, H. D., and Frye, J. C.: Mineralogy of glacial tills and their weathering profiles in Illinois. Part I: Glacial Tills, Circular 347, Illinois State Geological Survey, 1963.

Yariv, S. and Cross, H.: Geochemistry of colloid systems: For earth scientists, Springer Science & Business Media, 2012.

Zhu, C., Rimstidt, J. D., Zhang, Y., Kang, J., Schott, J., and Yuan, H.: Decoupling feldspar dissolution and precipitation rates at near-equilibrium with Si isotope tracers: Implications for modeling silicate weathering, Geochimica et Cosmochimica Acta, 271, 132–153, https://doi.org/10.1016/j.gca.2019.12.024, 2020.

Zhu, C., Zhang, Y., Rimstidt, J. D., Gong, L., Burkhart, J. A., Chen, K., and Yuan, H.: Testing hypotheses of albite dissolution mechanisms at near-equilibrium using Si isotope tracers, Geochimica et Cosmochimica Acta, 303, 15–37, https://doi.org/10.1016/j.gca.2021.03.023, 2021.